Title
Ballistocardiogram (BCG) Removal for Continuous EEG Recordings inside a 3-T MR scanner

Author
XIA, HONGJING

Publication Date
2014

Peer reviewed|Thesis/dissertation

University of California
Los Angeles

Ballistocardiogram (BCG) Removal for Continuous EEG Recordings inside a 3-T MR scanner

A dissertation submitted in partial satisfaction
of the requirements for the degree
Doctor of Philosophy in Biomedical Engineering

by

Hongjing Xia

2014

Abstract of the Dissertation

Ballistocardiogram (BCG) Removal for Continuous EEG Recordings inside a 3-T MR scanner

by

Hongjing Xia

Doctor of Philosophy in Biomedical Engineering

University of California, Los Angeles, 2014

Professor Mark S. Cohen, Co-chair

Professor Dan Ruan, Co-chair

Biological processes often produce signals detectable by multiple means, but with entirely different information content. For both research and clinical applications concurrent multi-modality data collection plays an important role in understanding the signal sources. Electroencephalography (EEG) and functional magnetic resonance imaging (fMRI) are particularly interesting examples, in that each offers largely independent yet complementary information on neuronal activity. While we and others have made great strides in making concurrent EEG-fMRI recordings possible, the EEG data, in particular, still contain signal artifacts of cardiac origin (ballistocardiogram) that make EEG analysis difficult, or even impossible.

To date, no satisfying means to separate brain EEG signal and ballistocardiogram (BCG) exist especially for non-event-related-potential experiments and under 3-T MR scanner. The BCG presents high temporal non-stationarity due to variation in cardiac cycles [BPJ02, DSS07], and its amplitude scales with magnetic field strength [MHB13, YMG10]. This explains the considerable variation of success levels among studies, with more successful applications achieved at lower field strength. Previously published methods used one of blind

source separation methods to remove the BCG. All such blind source separation approaches, as reviewed in [GVK07, VDR10], are limited to performing component extraction based on the contaminated data alone, agnostic of the structural difference between BCG and EEG. Another kind of approach [BPJ02, MAF07, CMG14] is to utilize reference signals for the artifact itself. However, this requires purpose-built hardware and exploits no further denoising step besides a simple subtraction.

We have developed three algorithms to separate EEG signal and BCG artifacts. Firstly, we have designed a Direct Recording - Prior Encoding (DRPE) method to maximally incorporate prior knowledge of BCG/EEG subspaces described by bases learned from a modified recording configuration, and of the group sparsity characteristics in the signal. To further promote subspace separability, a Direct Recording Joint Incoherent Basis (DRJIB) method is proposed to learn a representative and sparse set of BCG and EEG bases by minimizing a cost function consisting of group sparsity penalties for automatic dimension selection and an energy term for encouraging incoherence. Reconstruction is subsequently obtained by fitting the contaminated data to a generative model using the learned bases subject to regularization. The third algorithm takes advantage of currently available high-density EEG cap, to reliably estimate the full-scalp BCG contribution from a near-optimal small subset (20 out of 256) of channels and a corresponding weight through our modified experimental setup using Orthogonal Matching Pursuit (OMP).

We show in carefully constructed simulations that the residual artifacts are reduced by several orders of magnitude to a tiny fraction of the true signal. In human studies we show that the methods work effectively, and validate our quantitative results. Beyond the application to the EEG-fMRI challenge, we expect that our algorithmic methods will have impact in many other domains where signal and contaminant have distinct information structures. Digital signal, imaging, or even financial data are also contaminated with noises so that studying and characterizing the information structures of desired and undesired signals would greatly improve the modeling power.

The dissertation of Hongjing Xia is approved.

Dario L. Ringach

Elliot M. Landaw

Dan Ruan, Committee Co-chair

Mark S. Cohen, Committee Co-chair

University of California, Los Angeles

2014

Table of Contents

List of Figures

List of Tables

Acknowledgments

This thesis would not have been possible without the help, support and patience of my advisors, Professor Mark S. Cohen and Professor Dan Ruan. Their good advice and friendship has been invaluable on both an academic and a personal level, for which I am extremely grateful.

I feel very fortunate to have the opportunity to work with the world-class students and researchers in our research groups over the past five years. Special thanks to Edward Lau who have always been reliable, resourceful, patient and fun to collect data with.

I gratefully acknowledge the support from Professor Martin M. Monti and John Dell'Italia for collaboration on the simultaneous EEG-fMRI projects, Professor Stanely Osher, Professor Wotao Yin and Professor Andrea Bertozzi at University of California, Los Angeles and Professor Jian-Feng Cai at University of Iowa for their time and mathematical expertise.

I thank Professor Elliot M. Landaw and Professor Dario L. Ringach, for their time and patience while serving on my PhD qualifying, candidacy and thesis committee.

To my good friends outside the lab: Teresa, James, Dankai, Yan, Zhe, Yi, Hoshun, Wenyang, Lichao, Peggy, Wei, Jesse, Dianna, Xi, Jennifer. Thank you for your companionship and constant support.

Finally, I thank my parents and my dearest Ran for your unconditional support, love and understanding, and for all of the sacrifices that you have made for me.

Vita

2005–2009	B.S. Dept. Electrical Engineering, Nanjing University.
2009–2014	Research Assistent, Biomedical Engineering, UCLA.
2014	Machine Learning Scientist Intern, Amazon corporation LLC, Seattle.

Publications

Hongjing Xia, Dan Ruan, Mark Cohen. "**Separation and Reconstruction of BCG and EEG Signals during Continuous EEG and fMRI Recordings**," in *Frontiers Brain Imaging Methods, 2014.*

Hongjing Xia, Dan Ruan, Mark Cohen. "**Removing ballistocardiogram (BCG) artifact from full-scalp EEG acquired inside the MR scanner with Orthogonal Matching Pursuit (OMP)**," in *Frontiers Brain Imaging Methods, 2014.*

Hongjing Xia, Dan Ruan, Mark Cohen. "**BCG Artifact Removal for Reconstructing Full-scalp EEG inside the MR Scanner**," in *Pattern Recognition in NeuroImaging (PRNI), 2013 International Workshop.*

Hongjing Xia, Dan Ruan, Mark Cohen. "**Coupled Basis Learning and Regularized Reconstruction for BCG Artifact Removal in Simultaneous EEG-fMRI Studies**," in *Biomedical Imaging: From Nano to Macro, 2013 IEEE International Symposium.*

Hongjing Xia, Dan Ruan, Mark Cohen. "**Regional Variations in the time course of EEG-fMRI Signal coupling**," in *Program 2012 Neuroscience Meeting Planner. New Orleans, LA: Society for Neuroscience, 2012. (OHBM 2012)*

Hongjing Xia, Dan Ruan, Mark Cohen. "**Method to remove Ballistocardiogram**

(BCG) artifact from full-scalp EEG acquired inside MRI scanners," *Patent Pending*

Kerr, W.T., Anderson, A., Hongjing, Xia, etc. "**Parameter Selection in Mutual Information-Based Feature Selection in Automated Diagnosis of Multiple Epilepsies Using Scalp EEG**," in *Pattern Recognition in NeuroImaging (PRNI), 2012 International Workshop.*

CHAPTER 1

Introduction

1.1 Background of EEG and fMRI

1.1.1 Motivation

The human brain is likely one of the most complex systems in nature. It is able to self-organize and perform an enormous variety of functions ranging from basic ones like homeostatic control to higher-order ones such as perception, action programming, emotion and consciousness. Even with substantial knowledge of the behaviors of individual neurons, progress in understanding the global organization has remained elusive largely because of the multi-scale nature of brain activity. From single neurons at the microscopic scale to cortical columns at the mesoscopic level and finally to the whole brain at the macroscopic level (See Figure 1.1), neuroscientists have tried to capture various aspects of the cerebral activity, particularly bioelectric, metabolic and hemodynamic attributes.

As discussed in [BPM11], there exist direct and indirect measurements of neural activity. Electrophysiological recordings directly measure the electric signals of neural activity and can be collected invasively and non-invasively with intracranial recordings [Mou57], electrocorticogram (ECoG) [Cat75] and electroencephalogram (EEG) [Ber29]. Recording hundreds of cells simultaneously, intracranial recordings have high temporal and relatively spatial resolutions, depending on the arrangement of electrodes, with the potential to resolve single-cell level activity. Placing electrodes directly on the cortex, ECoG is a minimally invasive electrophysiological measurement which provides slightly higher spatial resolution than EEG which recordes electric signals from the scalp. An indirect measurement of neural activity is through recording metabolic response like the blood oxygen-level dependent (BOLD) signal.

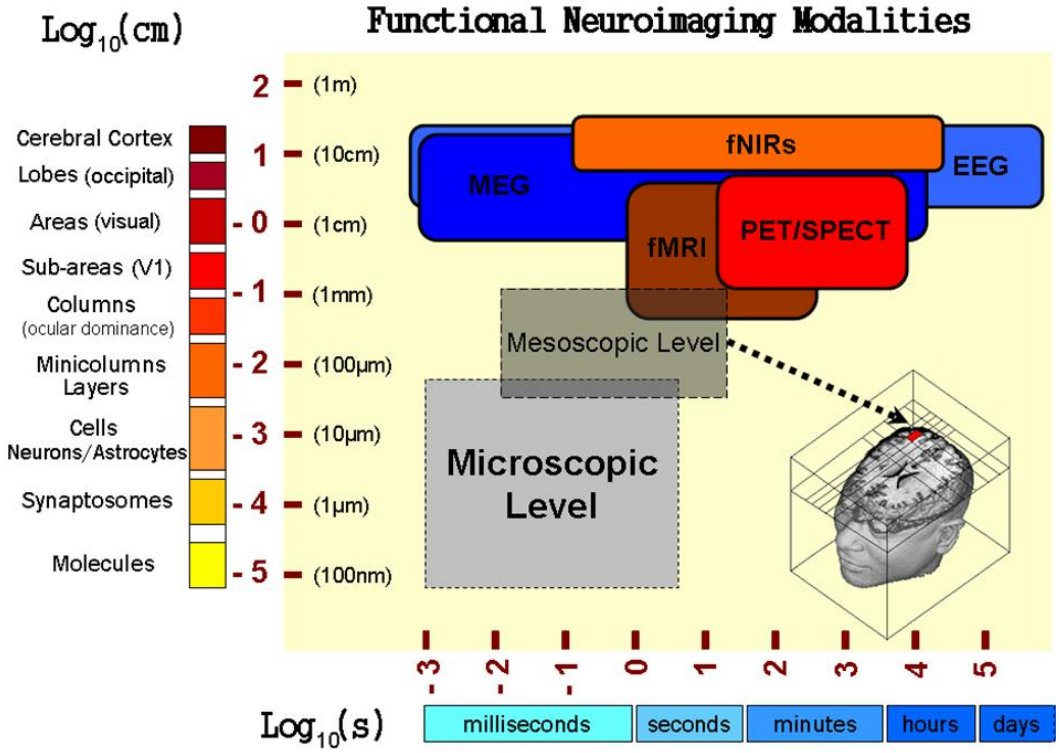

Figure 1.1: Overview of the study of brain at different scales [RS10] (Reprinted with permission).

Intrinsic optical imaging (ISOI) [GLF86] invasively measures hemodynamic activity (BOLD signal) which is measured noninvasively by functional magnetic resonance imaging [HSM04] and NIRS [Job77]. Although invasive methods generally can achieve high spatio-temporal resolution, non-invasive techniques provide the observation of brain activity across the entire brain volume and are available to experimental and clinical neuroscientists to study from in-vivo measures of brain electrical activity, often not feasible with invasive recordings. The most widespread noninvasive brain mapping techniques, including Electroencephalography (EEG), Magnetoencephalography (MEG), Functional Magnetic Resonance Imaging (fMRI), Positron Emission Tomography (PET), Single-Photon Emission Computed Tomography (SPECT), and Near-Infrared Spectroscopy (NIRS), have witnessed an explosive development during recent decades.

1.1.2 Electroencephalography

More than a century ago Caton [Cat75] discovered the existence of the electrical activity of the brain (the electroencephalography (EEG)), and Berger [Ber29] later demonstrated that we could directly record EEG from the scalp. Mainly contributed from the summed electrical signals of neuron populations and modestly from glial cells, scalp EEG records the voltage fluctuations of the brain electric activity versus time by placing the electrodes at a long distance from the sources on the scalp. More specifically, neurons contributing to EEG are excitable cells with intrinsic electrical properties that can produce electrical and magnetic fields. These fields depend on the synchronicity of neurons and require many neurons to generate significant amount of electric activity which eventually becomes detectable by the electrodes on the scalp. The strongest signals arise mainly from pyramidal neurons that are perpendicularly oriented to the scalp (See e.g., [NS05] and [ML09] for a more detailed review on the physiological origin of EEG signals). As an electrophysiological brain response to a stimulus, an event-related potential (ERP) can be reliably measured directly by means of EEG. Averaged from a large number of events, ERPs have different shapes for different types of stimuli, providing valuable information in evaluating brain functioning and a cheap noninvasive alternative to more expensive fMRI, PET studies. Non-ERP studies require high-quality EEG recordings as averaging around events is not feasible to suppress noise.

The main advantage of EEG is that EEG has very high temporal resolution, on the order of milliseconds when EEG data collection systems are capable of recording at sampling rates between 250 to 2000 Hz. However, even with sufficient coverages of electrodes over the whole head surface, the spatial resolution of EEG is much lower than that of intracranial recordings not only because EEG captures mostly dendritic currents as apposed to axonal currents, but also because EEG measures a summation of electric activity of neurons which renders source reconstruction an ill-posed inverse problem.The number and configurations of possible EEG sources become infinite given a set of measured scalp potentials without specific assumptions concerning the physical, geometric and anatomical properties of sources, conductive media and recording electrodes.

1.1.3 Functional Magnetic Resonance Imaging

Magnetic Resonance Imaging (MRI) scanners use a strong magnet, radio frequency and gradient coils to form images to non-invasively investigate the anatomy and physiology of the body in both health and disease without involving any use of ionizing radiation or radioactive tracers.

Determined by scanner hardware and the signal-to-noise ratio (SNR), the spatial resolution of fMRI can reach the order of sub-centimeter or even higher level with advanced imaging sequence and scanner hardware. The order of fMRI voxel dimensions is typically 2 to 4 mm, far superior to EEG. Despite that fMRI offers 3D coverage of the human brain, it has much lower temporal resolution than EEG, mostly limited by the intrinsic properties of BOLD fMRI. For the slow response of the vascular system to the glucose demands of the brain processing, the hemodynamic response generally lags its triggering neuronal events by 1 to 2 seconds and reaches its peak between 5 to 10 seconds. The BOLD signal, determined by the hemodynamic response, cannot capture fast neuronal changes and appears as a delayed, low-pass-filtered version of the neurophysiological response. As mentioned in [KRU97], the ultimate limitation of the temporal resolution may be the blurred intrinsic hemodynamic responses due to neuronal activation and a finite signal-to-noise ratio rather than the imaging techniques. Slow non-neuronal-related drifts (< 0.01Hz) also impose limitations on the temporal sampling frequency.

1.1.4 Simultaneous EEG-fMRI

Different imaging methods and experiments aim to understand the description of the brain dynamics at different scales, but simultaneously acquisition is scare and the integration of the data can be particularly difficult to interpret in such a complex dynamic system. Noninvasive unimodal methods such as EEG and fMRI have been very successful, but each of these methods can map only certain aspects of brain functions. The main sources of scalp EEG signals are postsynaptic currents associated with large pyramidal neurons, which are oriented perpendicular to the cortical surface [Nun81]. Despite the excellent millisecond-

range temporal resolution, reconstruction (inverse problem) of the location of the underlying bioelectrical activity cannot have a unique solution without prior information. On the other hand, being an indirect measure through metabolism, oxygenation and blood flow, BOLD signals appear to be temporally smoothed correlates of neuronal activity with abundant spatial resolution. As both EEG and BOLD signals are linked functionally with different temporal and spatial resolution, they are considered to hold complementary information regarding the underlying brain activity. It is of great value to integrate EEG and fMRI.For example, the temporal dynamics of epileptic activity can be captured with high temporal resolution by EEG, but the origin of the seizure in the brain cannot be determined with high spatial resolution. At this point, it should be mentioned that the we cannot expect a one-to-one relationship between scalp EEG/ERP and BOLD signal changes even though neural activity may be related to BOLD signal.

1.2 Technical Challenges of Simultaneous EEG-fMRI

Concurrent acquisition of EEG in the MR scanner environment has many technical and safety related challenges. While there exist different commercially available MRI compatible EEG technical setups, EEG instrumentation generally consists of three major parts: EEG electrodes, an acquisition system to filter, amplify and digitize the EEG signals, and some display/post-processing facilities. We use the term "EEG electrode" to describe the combination of the electrode head and connecting lead. The EEG electrodes have to be electrically conducting to collect voltage changes, as the EEG measures the electric signals from brain activity. However, one common thing to all EEG instrumentation is that the EEG electrodes are exposed to three major artifact-inducing causes: the strong homogeneous static magnetic B_0 field of the scanner, the rapidly varying magnetic fields from gradient switching and the radio frequency (RF) energy emitted during the imaging sequence [UD10, ML09]. According to the Faraday's law, we have that the electromotive force (emf) induced in a conductive loop is proportional to the rate of changes of magnetic flux cutting the loop and the loop

area:

$$V_{induced} = -\frac{d(\mathbf{B} \cdot \mathbf{S})}{dt} = -\frac{d\Phi}{dt}, \tag{1.1}$$

where $V_{induced}$ is the emf induced in the loop, $\mathbf{S}$ is the loop area perpendicular to the field, $\frac{d(\mathbf{B}\cdot\mathbf{S})}{dt}$ is the rate of changes of magnetic flux cutting the loop and Φ is the magnetic flux through the loop. Hence, not only changing magnetic fields cutting a loop can induce unwanted EEG artifacts, but so does the variation of loop area in the static field. This leads to two major kinds of EEG artifacts, the first MR gradient artifact is from rapidly changing magnetic fields due to imaging sequences; the second ballistocardiogram (BCG) artifact can result from the movement of the electrodes, small head movements, scanner vibration and motion of the blood (Hall effect). In comparison to the extremely detrimental effects of MRI on the quality of EEG recordings, there is no significant adverse degradation of the MR Image quality caused from the presence of properly designed and tested EEG equipment [UD10, ML09].

1.2.1 MR Gradient Artifacts

According to the above equation 1.1, the quality of recorded EEG data inside the MRI scanner depend on the MRI scanner field strength (B_0), the time-varying MR imaging sequence, the subjects' movement and behavior in the scanner and the EEG instrumentation. It was observed early that the MR scanning sequence results in completely indiscernible EEG recordings mainly due to the rapidly varying magnetic field gradients for spatial encoding of the MR signals and radio frequency (RF) pulses for spin excitation. Because RF artifacts appear at a much higher frequency than that of the normal brain EEG signal, it can be effectively filtered by a proper analog low pass filter which is already a mandatory component in the EEG amplifier system designed to avoid saturation and aliasing. Hence, the gradient switching induced artifacts (GA) completely dominates the EEG recordings and it has a broad spectrum overlaps with the frequency range of normal brain signals, as illustrated in Figure 1.2 showing EEG recordings of a few channels from a 3 Tesla MR scanner during BOLD echo planar imaging (EPI) sequence. Visual inspection is not sufficient to identify

EEG patterns.

However, due to the preprogrammed nature of the gradient switching sequence, the EEG artifacts induced by the scanning process are strongly deterministic. As a result, the gradient artifacts are relatively easy to manage using template-based correction methods [HBM95, AJT00, GSE00, CGS01, Coh02, NBI05] while another artifacts called ballistocardiogram (BCG) appearing in the EEG data recorded inside the scanner presents a more challenging obstacle [UD10, MHB13] due to the magnetic influx changes from unpredictable subjects' movement and non-stationary cardiac pulses.

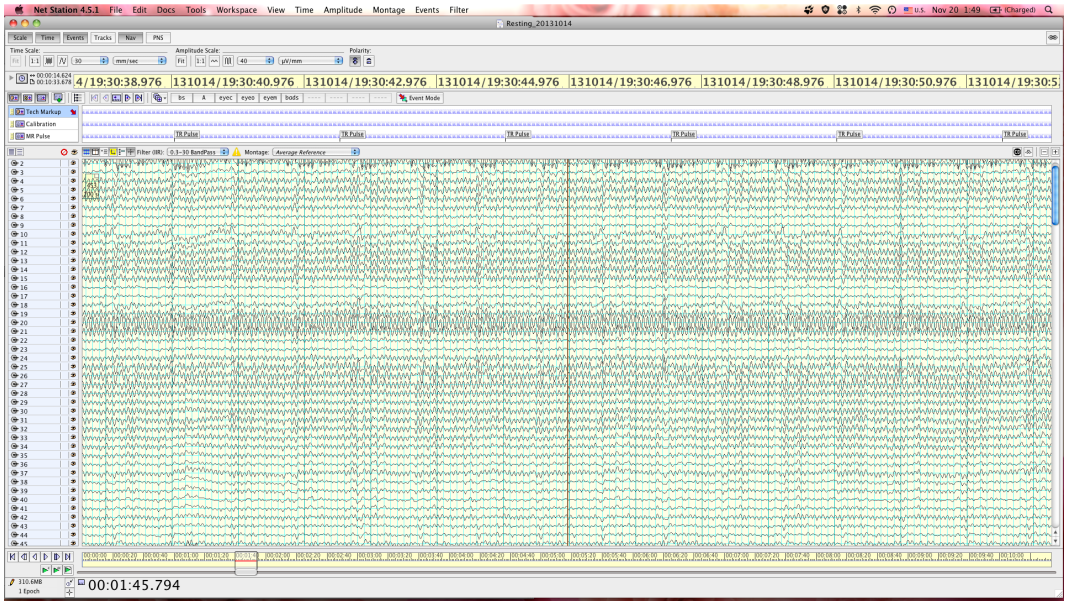

Figure 1.2: Illustration of recorded EEG signals during a fMRI EPI acquisition sequence.

1.2.2 Ballistocardiogram (BCG) Artifacts

As the ballistocardiogram (BCG) is always present, its contribution becomes clearly visible and dominant after gradient artifact removal. In the absence of any scanning sequence, BCG contributes to the frequency range that overlaps with normal EEG signals [UD10]. As shown in Figure 1.3, BCG traces synchronize with the simultaneously recorded electrocardiogram (ECG). But ECG, representing the cardiac rhythm, fluctuates over time and across subjects and is under autonomous nervous system control, resulting in significant temporal

non-stationarity in BCG. In addition to the temporal variability, BCG also presents channel-by-channel spatial variations that cannot be completely accounted for by linear scaling. The variability in both time and space is a key consideration and obstacle for artifact removal methods. [DMN08] has studied in details the spatial-temporal features of BCG.It is observed that a low spatial frequency can characterize the BCG topography which also varies substantially over time. It seems that moving, rotating and polarity-inverting contribute significantly to the dynamic activity of BCG. Although still under discussion, the types of motion that contribute to ballistic effects may be associated with electrodes movements from a rocking, nodding head motion [DMN08, NAM06, ASY02] and/or pulsation effects from nearby blood vessels.As the electrodes cut the magnetic field spatially differently depending on the locations, the BCG artifacts certainly differ across experimental sessions and subjects. The temporal and spatial complexity of the BCG significantly increases the difficulty of removing them thus impedes the wide-spread applications of simultaneous EEG-fMRI techniques. Moreover, experimental results with monkey recordings in [TGM83] demonstrated that the amplitude of the BCG artifacts scaled approximately linearly with the static magnetic field strength B_0 [DMN08], in agreement with the above equation 1.1.

Based on the Faraday's law of induction and the equation 1.1, motion related to cardiac activity (ballistic effects) and the blood movement (Hall effect) can give rise to the induced artifact signals formed by the circuit of the electrodes and subjects. The moving blood is probably electrically conductive and its abrupt changes (acceleration) could lead to Hall effect which dictates that when placed in a strong magnetic field a voltage difference would be created on opposite sides of a moving conductor, which may be a source of current induction that contributes to the BCG artifact.

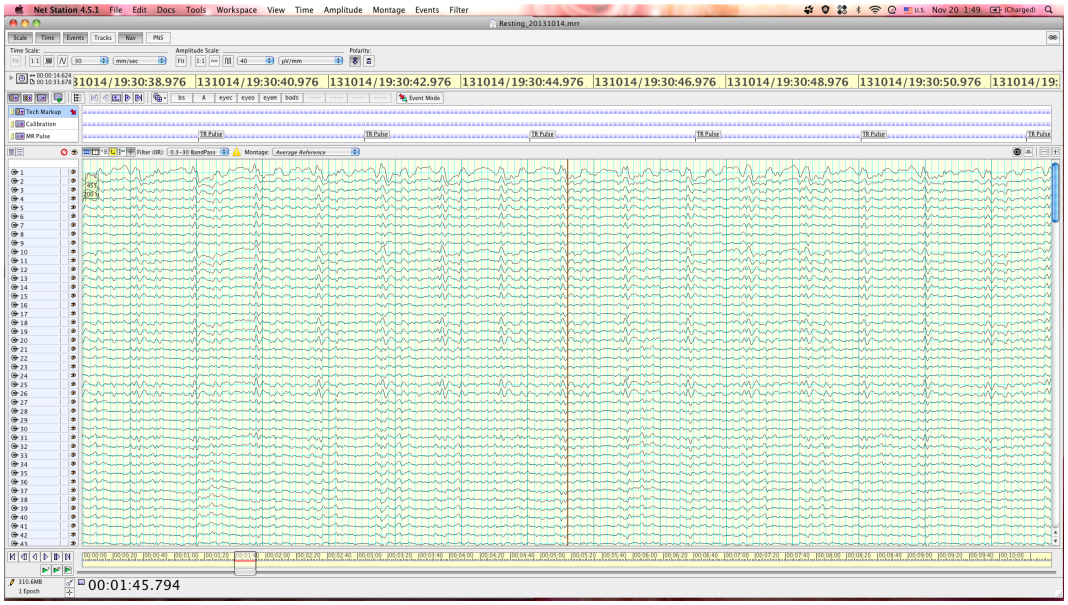

Figure 1.3: Illustration of BCG artifact in EEG signals without MRI scanning in a 3T MRI scanner. BCG is present in all channels and appear to have different morphologies.

1.3 Previous Publications about BCG Artifact Removal

1.3.1 Blind-source separation-based BCG Removal

One of the major attempts to remove the BCG focused primarily on channel-wise denoising from the point of view of blind source separation. Principal component analysis (PCA) and independent component analysis (ICA) are two blind sources separation methods based on distinct assumptions, as reviewed in [GVK07, VDR10].

There are many ways to explain and formulate principal component analysis (PCA). In terms of *analysis*, PCA sequentially projects the data on subspaces that explain the largest fraction of the variance of the data. In terms of *synthesis*, PCA finds a basis or orthogonal dictionary, such that all signals observed admit decompositions with low reconstruction error. For regular PCA, the two views are equivalent. The *analysis* view of PCA is about finding a projection $v \in \mathbb{R}^p$ that maximizes variance of signal $X \in \mathbb{R}^{n \times p}$, where n and p are the

number of samples and the number variables:

$$\begin{aligned} &\max_{v_i \in \mathbb{R}^p} v_i^T X^T X v_i \\ &\text{s.t. } v_i^T v_i = 1 \\ &\quad v_j^T v_i = 0,\ j < i; \end{aligned} \tag{1.2}$$

The *synthesis* view of PCA is about finding V=[v_1,...,v_m] s.t. x_i which gives low reconstruction error on span(V) [ZHT06]:

$$\begin{aligned} &\min_{V \in \mathbb{R}^{p \times m}} \left\| X - XVV^T \right\|_F^2 + \lambda \left\| V \right\|_F^2 \\ &\text{s.t. } V^T V = I \end{aligned} \tag{1.3}$$

The *analysis* interpretation leads to sequential computation of the principal components that captures the maximum variability and guarantees minimal information loss. The resulting principal components are uncorrelated and orthogonal to each other. The *synthesis* interpretation leads to global formations which estimate simultaneously all principal components using a singular value decomposition (SVD), and are referred to as a matrix factorization problem in machine learning and dictionary learning in signal processing.

The most widely used Optimal Basis Sets method (OBS) [NBI05] is a PCA-based approach that regresses out the mean effects and its first few principal components from the contaminated data on a heartbeat-by-heartbeat basis. This PCA-based algorithm, allows for more variations in the shape of successive BCG artifacts than reconstructing BCG from averaging [APK98]. OBS assumes orthogonality between the BCG and EEG subspaces and that the selected principal components span the BCG subspace. Other widely used adaptive template approaches for BCG suppression such as [FF05] can be interpreted as weighted PCA to incorporate temporal model updates.

Independent component analysis (ICA) aims to decompose the time series into statistically independent components, assuming that the observed time series signals are unknown linear mixtures of statistically independent source signals. As a data driven method, ICA has been used successfully and extensively in removing physiological or movement-related noise. Mathematically, let us assume we observed a m-dimensional data vector

$\mathbf{x}(k) = [x_1(k), ..., x_n(k)]^T$ at time instant k linearly mixed by unknown sources $s(k)$ with the mixing coefficients A:

$$\mathbf{x}(k) = \sum_j \mathbf{a_j} s_j(k) = As(k), \tag{1.4}$$

The collected signals (EEG) X can be represented with

$$X = A \cdot S + N, \tag{1.5}$$

where N is assumed to be uncorrelated Gaussian noise with zero-mean. The goal becomes estimating both unknown source S and unknown mixing coefficient A from collected signals X. Recovering the source signal S in principal is done through inverting the mixing coefficients as the following

$$Y = \hat{S} = WX = WAS, \tag{1.6}$$

where $W \approx A^{-1}$ is an unmixing matrix. With the constraint of statistical independence, it becomes possible to determine A and S. In [BAW03, SCL05, MPC07, GNM10, LZG12], ICA-based methods have been shown to be relatively efficient in removing BCG-related components. However as reviewed in [VDR10], there are at least three concerns limiting the application of ICA-based BCG removal methods : 1) there exist many ICA algorithms that rely on different assumptions of statistical independence and implementations, generating different results; 2) The number of BCG-related components is crucial but undetermined; 3) The criteria of selecting BCG-related components is also relatively subjective.

Attempts to incorporate spatial information have also been made with spatial PCA and ICA by [BAW03, SCL05]. However these PCA/ICA-based approaches are based on strong orthogonality/independence assumptions and subject to manual selection of number of components to be included. All such blind source separation approaches, as reviewed in [GVK07, VDR10], are limited to performing component extraction based on the contaminated data alone, agnostic of the structural difference between BCG and EEG.

1.3.2 Reference-signal-based BCG Removal

Another major focus on BCG suppression is to use reference signals to remove the artifacts. With an extra piezoelectric motion sensor located over the temporal artery [BPJ02], Bonmassar et al. obtained an indirect measure of the BCG waveforms and applied an adaptive Kalman filter approach to filter the BCG based on the correlation between the motion sensor signal and the EEG. The Kalman adaptive filter estimates the coefficients of the Finite Impulse Response (FIR) filter from minimizing a linear minimum mean square using a one-step predictor algorithm [BPJ02]. A similar method has been proposed by [MAF07] to record motion using wire loops as motion sensors on an electrode cap, claiming a more complete model of head movements with a linear adaptive filter technique. However the Kalman filter technique relies on the questionable assumption that the EEG signal has a white noise characteristics and appears to be computationally demanding [ILP06].

More recent developments apply an insulating layer to directly acquire BCG-only artifact signals from channels that are electrically isolated from the scalp. A technically innovative fEEG^{TM} system from (Kappametrics Inc., Chantilly, USA) is developed to reduce the artifacts even before the data reaches the amplifier. Their special cap has several layers. The one that is connected to the scalp is the measurement layer, and another layer not connected to the scalp is the reference layer. There is a third layer that creates an ionic-conductive reference loop that is co-located with (on) its scalp electrodes but not in contact with the scalp. Therefore theoretically this layer measures the same amount of artifacts without actual EEG signals. The difference signals between the scalp electrodes and its local reference counterpart in theory becomes artifact-free EEG when the impedance and changes of the impedance in conductivity matches perfectly to that at the scalp electrodes over time at the reference electrodes . [CMG14, MHB13, XRC13b] have published artifact cleaning results based on similar insulation-layer-related acquisition idea but using different hardware modifications and removal methods. Although the measured artifact reference signals are probably not identical to the BCG [MHB13], significant suppression has been achieved by reference layer artifact subtraction (RLAS) [CMG14]. However, RLAS and fEEG^{TM} both

require purpose-built hardware and exploit no further denoising steps than a simple subtraction. Admittedly, there exists some discrepancy between each of these reference signals and the "ground-truth" BCG signals, as a result of either insulation or sensing process. As mentioned in [UD10], these signal differences may become the limiting error term when used simply for linear subtraction.

1.4 Organization of the thesis

This thesis presents three algorithms to separate BCG and EEG and improve the quality of reconstructed EEG. Adapted from our published work [XRC14b], Chapter 2 first proposes a new experimental setup to acquire artifact-only signals. Our modified recording configuration allows us to obtain representative bases of the BCG- and EEG-only signals. With the prior knowledge of BCG/EEG subspaces, we then introduce an optimization-based reconstruction approach to maximally incorporate prior knowledge of the BCG/EEG subspaces, and of the signal characteristics within them. This Direct Recording Prior Encoding (DRPE) method outperforms the OBS method by nearly 7 fold in separating the continuous BCG and EEG signals. Chapter 3, adapted from [XRC13b], further improves the subspace separability by minimizing a cost function consisting of group sparsity penalties for automatic dimension selection and an energy term for encouraging incoherence. Extracted from [XRC13a, XRC14a], chapter 4 introduces an integrated learning and inference approach to reliably estimate the full-scalp BCG artifacts from a near-optimal small subset (20 out of 256) of channels identified through our modified experimental setup. A corresponding weight is also learned. Subsequent recordings can reconstruct BCG-only signals with BCG-only signals from the subset of channels and previously learned weight. The reconstruction of the EEG is performed with a direct subtraction and an optimization scheme. We evaluate the performance on both synthetic, and real contaminated recordings, and compare the performances to the ones from the benchmark Optimal Basis Set (OBS) method. In the non-event-related EEG studies, our reconstruction can yield more than 14-fold improvement in reducing the normalized RMS (nRMS) error of EEG signals. Chapter 5 concludes the

three algorithms and provides some suggestions for future work.

CHAPTER 2

Separation and Reconstruction of BCG and EEG Signals during Continuous EEG and fMRI Recordings

2.1 Abstract

Despite considerable effort to remove it, the ballistocardiogram (BCG) remains a major artifact in electroencephalographic data (EEG) acquired inside magnetic resonance imaging (MRI) scanners, particularly in continuous (as opposed to event-related) recordings. In this study, we have developed a new Direct Recording-Prior Encoding (DRPE) method to extract and separate the BCG and EEG components from contaminated signals, and have demonstrated its performance by comparing it quantitatively to the popular Optimal Basis Set (OBS) method. Our modified recording configuration allows us to obtain representative bases of the BCG- and EEG-only signals. Further, we have developed an optimization-based reconstruction approach to maximally incorporate prior knowledge of the BCG/EEG subspaces, and of the signal characteristics within them. Both OBS and DRPE methods were tested with experimental data, and compared quantitatively using cross-validation. In the challenging continuous EEG studies, DRPE outperforms the OBS method by nearly 7 fold in separating the continuous BCG and EEG signals.

2.2 Introduction

Concurrent acquisition of EEG and functional magnetic resonance imaging (fMRI) is an approach with great potential for studying different, yet connected aspects of cerebral activity, particularly bioelectric and hemodynamic attributes. With their different tempo-

ral and spatial resolutions, EEG and fMRI are understood to be linked functionally, and yet to hold complementary information regarding underlying brain activity. Simultaneous acquisition of both signals has proven its value in many applications, such as studies of spontaneous brain rhythms [GSE02], and the analysis of event-related brain responses [MJS04, DUS05, DUS06, ECM08, MEN08, SGA11, DWS12].

While artifacts in the simultaneously acquired MRI data now are relatively easy to manage [HBM95, AJT00, GSE00, CGS01, Coh02], artifacts appearing in the EEG data recorded inside the scanner presents a more challenging obstacle [UD10, MHB13]. The most prominent magnetically induced artifact in EEG acquired inside the scanner is the ballistocardiogram (BCG) [UD10, YMG10, MHB13]. The BCG is especially difficult to suppress in protocols using continuous recordings, such as studies of the EEG rhythms. The BCG presents high temporal non-stationarity due to variation in cardiac cycles [BPJ02, DSS07], and its amplitude scales with magnetic field strength [YMG10, MHB13]. This explains the considerable variation of success levels among studies, with more successful applications achieved at lower field strength.

Previously published methods to remove the BCG have approached the problem as one of blind source separation. At the time of this writing, the most widely used means of suppressing the BCG artifacts likely is the Optimal Basis Sets (OBS) method [NBI05], which uses principal component analysis (PCA) to identify components in the contaminated recordings, then adaptively removes the linear regression of the mean effect and a fixed number of components. This PCA-based algorithm therefore assumes orthogonality between the BCG and EEG subspaces, and that the selected principal components span the BCG subspace. Other widely used adaptive template approaches for BCG suppression such as [FF05] can be interpreted as weighted PCA to incorporate temporal model updates. Methods based on independent component analysis (ICA) [SCL05, GNM10, LZG12] also are used widely. All such blind source separation approaches, as reviewed in [GVK07, VDR10], are limited to performing component extraction based on the contaminated data alone, agnostic of the structural difference between BCG and EEG.

Another approach to BCG suppression is to utilize reference signals for the artifact itself.

Motion sensors [BPJ02] and wire loops [MAF07] have been proposed to generate such reference signals. Recent developments [CMG14, MHB13, XRC13b] utilize an insulating layer to directly acquire artifact signals from across the scalp. Although the measured artifact reference signals are not identical to the BCG [MHB13], significant suppression can be achieved by a simple reference layer artifact subtraction (RLAS) [CMG14]. However, RLAS requires purpose-built hardware and exploits no further denoising step besides a simple subtraction. We propose a method that has an experimental setup with no hardware modification and includes an additional denoising step using prior knowledge of EEG to further reduce residual BCG signals for continuous (non-ERP) experiments.

More specifically, we address the challenge of BCG artifact removal in spontaneous EEG-fMRI experiment from the perspective of subspace separation. Our method consists of two novel steps: (1) a basis analysis phase where representations of the BCG signal subspace and spontaneous (continuous) EEG signal subspace are characterized separately, and (2) a reconstruction phase where contaminated EEG data are decomposed into BCG and EEG components utilizing the learned bases, as well as structures of corresponding coefficients. For the basis analysis stage, we designed a new and simple recording configuration to obtain BCG-only signals directly inside the scanner, and clean EEG signals outside the scanner, alleviating the risk of model mismatches introduced by strong (and possibly impractical) assumptions about subspace relationships. In the reconstruction phase, we designed and implemented an optimization scheme that incorporated prior knowledge, more specifically the structures we discovered from studying pure BCG noise and clean EEG data individually, derived from our novel experimental setup. To assess the improvements we quantified the performance of the proposed method, and compared it with the OBS method, using both simulated and real contaminated data. In so doing, we demonstrated large improvements in BCG artifact removal.

2.3 Generative Model for Contaminated Data

Though the exact cause of the BCG artifacts is not known completely, EEG and BCG signals are believed to originate from independent sources of different nature, as EEG arises from the brain, while BCG comes from physical movements of the head and blood. Basic electricity and magnetism dictates that the two signals should add linearly without interaction terms. Therefore, the contaminated measurements can be modeled as a superposition of BCG and EEG signals subject to noise contamination according to

$$Y = X_{bcg} + X_{eeg} + \sigma \tag{2.1}$$

where X_{bcg}, X_{eeg} and $\sigma \in \mathbb{R}^{C \times T}$ represent the BCG artifacts and the uncontaminated normal EEG brain signals acquired from our high-density system with noise σ. The dimension $C = 256$ is the number of channels in an EEG system, and T is the time points of the recordings. Moreover, the "independence" is in the sense of physics and physiology, rather than statistical. This generative model makes no presumption about the existence of their subspace relationships such as orthogonality or independence. This superposition model has been applied implicitly in many previous studies [AJT00, GSE00, NBI05, GVK07, VDR10].

2.4 Experimental Setup

Three healthy adult volunteers, (2 males and 1 female, all right-handed, age between 24 to 26 yrs), gave informed consent for participation in this study according to the guidelines of the UCLA medical investigational review board. For our experiments, we used a 3T Siemens Tim Trio scanner (Siemens Medical Solutions, Erlangen, Germany). We acquired EEG data from both inside and outside the scanner using a GES300MR system (Electrical Geodesics, Inc., Eugene OR). This 256-channel apparatus made contact with the scalp via KCL-filled sponge contacts mounted in plastic pedestals with a contact-impedance of 20kΩ or less. EEG data were sampled at 250Hz and amplifier gains were kept constant. To focus on only BCG artifacts, no MRI scanning took place during the acquisition inside the scanner. The overall protocol was designed to record spontaneous brain activity with the focus on the variations

of the alpha (8-13 Hz) EEG rhythm.

2.4.1 Experimental Session I: Acquisition of EEG-only Data

Outside of the scanner room, we acquired EEG from one subject who lay comfortably inside an MR scanner simulator with earphones in place; sponge cushions were used to minimize head movements. The other two were studied in our electromagnetically-shielded EEG acquisition lab. All recordings were carried out in a darkened quiet environment, while the subjects lay supine on a carpet with a blanket, with a pillow made of viscoelastic foam placed under his head. They were asked to stay awake, with their eyes closed, during the whole acquisition. The simulator acquisition was designed to mimic closely the environment inside the scanner (subject posture and claustrophogenic aspects of the MR environment).

2.4.2 Experimental Session II: Acquisition of BCG-only and Contaminated Data

Inside the scanner, BCG-only and contaminated data were acquired at the same time from different channels in this session.

Acquisition of BCG-only data: On the channels chosen to collect BCG-only signal, two layers of material were inserted between the scalp and the electrodes.
1) Insulating Layer: To collect BCG-only artifacts, we first isolated a subset of electrodes from the scalp with a plastic insulating barrier to block brain signals from conduction, as shown in Figure 2.1(A).
2) Semi-conducting Layer: In order to properly collect signals from insulated electrodes, a semi-conductive layer was then inserted between the insulating layer and electrodes. We chose a piece of thin paper dampened with saline (Figure 2.1(B)) as the semi-conductive layer, to provide proper impedance and to avoid any short circuit or alteration of BCG signals.

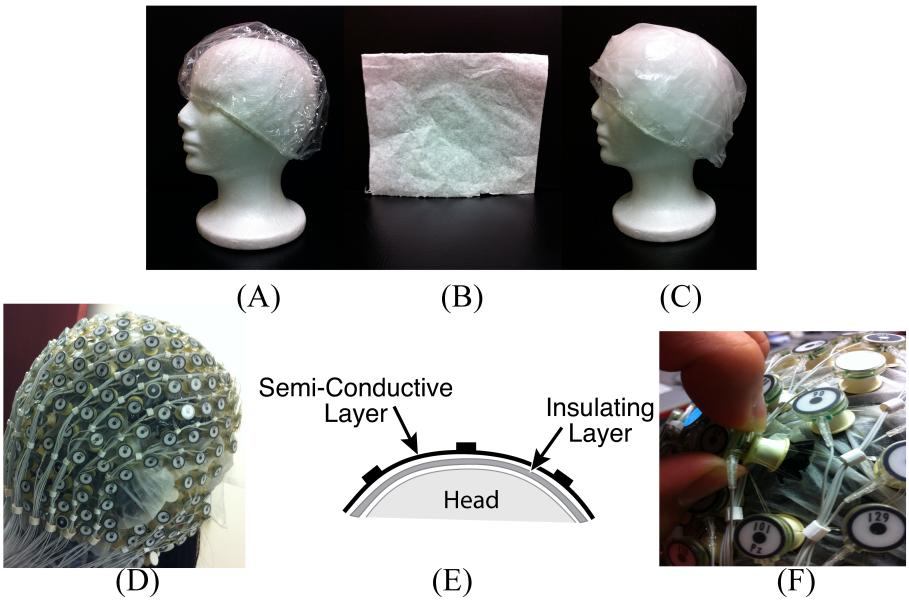

Figure 2.1: (A) Insulation layer: a shower cap (B) Semi-conducting layer: paper layer (C) A piece of thin paper dampened with saline placed on top of the insulation layer (D) A picture with all channels blocked (E) Sandwich diagram of construction (F) Unblocking one channel.

Acquisition of Contaminated EEG data: Inside the scanner, the unblocked channels recorded real EEG data corrupted by the BCG artifacts, simultaneously with the acquisition of BCG artifact-only signals from the blocked channels. We chose to block all channels globally, as shown in Figure 2.1(D), and then unblock selected channels by removing the insulation and paper layers (see Figure 2.1(F)). As most experiments use standard low-density 10-20 systems to investigate the spontaneous brain rhythms, we chose to unblock 20 conventional channels, leaving 236 out of 256 channels blocked. This electrode-blocking pattern was chosen principally for its simplicity to demonstrate the feasibility of our new framework. One can determine which channels to block in advance and use the setup in Figure 2.1(F) to maximize the number of EEG channels that collect EEG signals. Figure 2.2(A) shows the measured impedance when all electrodes were blocked, including the reference and ground electrodes. Figure 2.2(B) is the measured impedance when the reference and ground channels are unblocked along with the 20 conventional channels. The impedance difference before and after unblocking is shown in Figure 2.2(C). Note that the impedance of blocked and unblocked channels were all 20kΩ or less, ensuring the quality of collected BCG-only

signals.

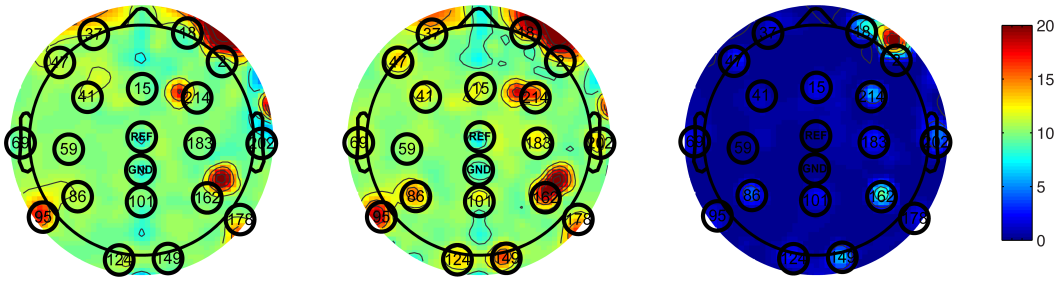

(A) (B) (C)

Figure 2.2: The numbers shown on the topographic maps are channel numbers. The conventional channels along with the reference and ground channels are highlighted with black circles. The color indicates the measured impedance number in kΩ. (A) Measured Impedance when all channels are blocked. (B) Measured impedance when reference and ground channels along with conventional 20 channels are unblocked. (C) The difference of impedance between (A) and (B).

2.5 Data preprocessing

Generally, we use $x \in \mathbb{R}^T$ to represent any collected data from one channel. We followed exactly the preprocessing procedure implemented in EEGLAB plug-in fMRI version 1.2 [NBI05] to divide a channel-wise 1-D signal into a data matrix. First, the slow drifts were removed with a high pass filter with a cutoff frequency at 1Hz. Second, the filtered data x was segmented into k (k=number of heartbeats) segments, $x_i \in \mathbb{R}^m$, for each detected heartbeat retrieved from the ECG channel. Each of these segments is an $m \times 1$ column vector, where m is the number of time points of the signal segment which is centered around the heartbeat and 1.5 times the median length of detected R-R intervals. Third, all segments were aligned in a matrix $\tilde{\mathbf{X}} = [x_1|x_2|...|x_k] \in \mathbb{R}^{m \times k}$. Finally, the mean effect $\bar{x} = \frac{1}{k}\sum_{i=1}^{k} x_i \in \mathbb{R}^m$ was calculated for all segments and removed from the data matrix before a PCA was applied to the residual artifacts, $\mathbf{X}$. The same procedure was applied to all collected data including BCG-only, EEG-only and contaminated signals. While alignment to the heartbeats

facilitates learning of the BCG bases by reducing the data complexity caused by the non-stationary heartbeats, it has no obvious advantage for the EEG data.

Unlike the OBS method, where the mean effect along with the first several PCs were fitted to, and subtracted from, each segment of contaminated data (we now denote the contaminated data $\tilde{\mathbf{Y}}$) to generate the estimated EEG signals, our method operated by separating the demeaned BCG, $\mathbf{X}_b$, and EEG, $\mathbf{X}_e$, matrices from the demeaned contaminated data, $\mathbf{Y}$. The mean effect derived from $\tilde{\mathbf{Y}}$, was added back to the recovered BCG matrix under the assumption that the EEG signals are close to zero-mean, as EEG segments should be relatively uncorrelated with the heartbeats. The same assumption is made in the OBS method [NBI05].

We use $\mathbf{X}[:, j]$ to denote the j^{th} column vector, and $\mathbf{X}[i, :]$ for the i^{th} row vector of matrix $\mathbf{X}$. Subscripts are used to indicate the type of signals. As prior information for the BCG and EEG signals, the pure BCG from one channel (B) in session II is denoted as $\mathbf{X}_{b\_prior} \in \mathbb{R}^{m \times k_1}$ and the EEG in session I, from another channel (A or B), is denoted as $\mathbf{X}_{e\_prior} \in \mathbb{R}^{m \times k_2}$. To minimize spatial variations of the BCG artifacts we chose the BCG prior data from a channel adjacent to the contaminated data as well as the BCG data used in the following simulation. This adjacent channel was placed to avoid major surface vessels.

2.6 Stage I: Basis Construction

Unlike the OBS method, where basis vectors are retrieved from contaminated data, our direct-recording prior encoding (DRPE) approach generates them from the experimentally acquired BCG-only and EEG-only signals. We expect direct characterization of the BCG and EEG subspaces to be advantageous, in that they remain more faithful to each signal type. We use principal component analysis (PCA) in this pilot investigation. The prior data matrices for BCG ($\mathbf{X}_{b\_prior}$) and EEG ($\mathbf{X}_{e\_prior}$) correspond to the following decomposition:

$$\begin{aligned} \mathbf{X}_{b\_prior} &= \mathbf{B}_{b\_prior}\mathbf{C}_{b\_prior} \\ \mathbf{X}_{e\_prior} &= \mathbf{B}_{e\_prior}\mathbf{C}_{e\_prior} \end{aligned} \tag{2.2}$$

where $\mathbf{C}_{b\_prior}$ and $\mathbf{C}_{e\_prior}$ are coefficient matrices, and $\mathbf{B}_{b\_prior}$ and $\mathbf{B}_{e\_prior}$ are full-rank basis matrices with orthonormal columns. The resulting PCA basis, $\mathbf{B}_{e\_prior}$, expands a subspace that best incorporates all possible phases presented in this training session. One may envision the basis set as a set of typical temporal signatures, and the specific phase in each segment is captured by the variation in the weighting coefficients.

2.6.1 Justification of BCG Prior Basis Vectors

BCG artifacts can be caused by the magnetic flux changes from either the magnetic field or wire loop movement from either local electrodes movement or more global head rotation [YMG10]. Surface blood flow is an example of the former, while the latter include respiration-induced movement of electrodes, and pulsation of blood vessels. In the our experimental setup, using the 256-channel collection net, we expect surface blood flow velocities, and the electrode movements, to be locally consistent, given the close placement of the neighboring electrodes in the dense net. With the BCG from the fully blocked net, the relative errors (RE) between BCG signal from each target channel (here we use conventional 20 channels for illustration-purposes), and those from the remaining channels, are calculated. We show in Figure 2.3(A) that each target channel has a corresponding neighboring channel that gives the smallest relative error. Figure 2.3(B) reveals the similarities of BCG traces among four neighboring channels. It is therefore safe to assume that for any channel under examination, there exists a neighboring blocked channel whose BCG reading closely resembles the BCG artifact from the unblocked channel. This is ensured further by creating blocking patterns that provide a sufficient number of adjacent ground-truth BCG signals as candidates for this purpose.

2.6.2 Justification of EEG Prior Basis Vectors

Although the EEG measurements recorded inside and outside of the MR scanner may not be exactly equivalent [SBG05, DUS06], potentially being affected by the posture, and by the magnetic and claustrophobogenic MR scanner environment, it still is reasonable to assume

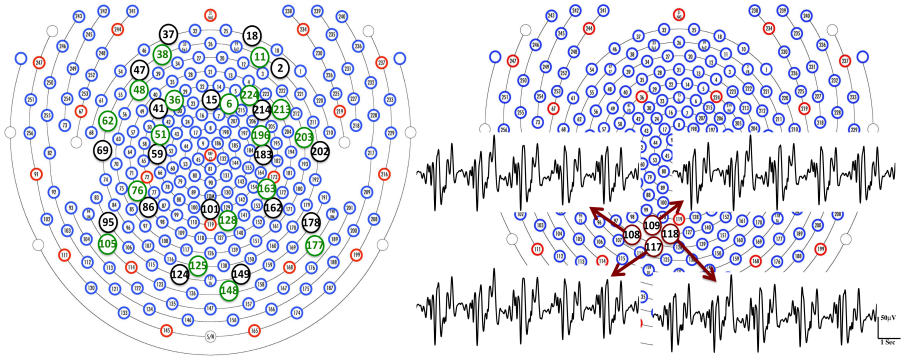

Figure 2.3: (A) We are able to find a channel (green circle) that gives the smallest relative error in the neighborhood of each target channel (black circle). (B) BCG temporal traces from four neighboring channels are displayed with highlighted channel location in red circles.

that the brain EEG generates consistent recordings both inside and outside the scanner, produces similar EEG characteristics, such as the dimensionality of normal brain EEG data and global power spectrum. For ERP-type EEG signals, a different prior should be considered, as the timing of triggering events is available. For continuous EEG signals, we opt for an approximate prior in terms of a consistency requirement. In continuous EEG, one does not have access to strong structural alignment references such as trigger timing in ERP, and has to rely on weaker consistency type priors for signal modeling. Here we assume the EEG signal representation space is approximately consistent, and extrapolate from the bases learned from outside the scanner to estimate the EEG-only signal inside the scanner. The difference in the signal, per se, and the temporal non-stationarity, is characterized by the variation in the weighting coefficient with respect to the basis. In other words, we utilize the same set of basis functions for EEG signal acquired outside and inside scanner, but with different composition weightings.

On the experimental level, we have tested our signal separation power (see the Result Sect. 2.9.3) with bases learned from different subjects under different acquisition environments (with or without a mock scanner), keeping only the posture of subjects the same. Furthermore, on the theoretical level, we use the basis function, rather than the data themselves, from EEG-only collected data outside of the scanner, to facilitate inside scanner

reconstruction and analysis: this requires only a rough consistency of signal space, rather than strict equivalence.

2.7 Stage II: Separation and Reconstruction

Based on the assumption that the characteristics of continuous EEG signals generated inside and outside the scanner are reasonably consistent for the same subject, and that the BCG signals acquired from our insulated channels are similar to the BCG components in the unblocked channels, we propose to reconstruct the BCG/EEG components from the contaminated data by estimating the coefficients for the bases from BCG (inside the scanner) of a neighboring channel and EEG (outside the scanner) from the same subjects.

2.7.1 Regularizations for Reconstruction

2.7.1.1 BCG:

Significant temporal variations exist in the BCG artifacts, as illustrated in Figure 2.4. Based on the premise that the reconstructed BCG should be similar to the concurrently acquired BCG-only signals from the blocked electrodes ($\mathbf{X}_{b\_prior}$), we chose an ℓ_2 penalty as the first term in the minimization objective in Equation (2.5).

2.7.1.2 EEG:

To incorporate the likely temporal non-stationarity of the continuous EEG signal (as shown in Figure 2.5), we impose a flexible prior based on a general low-dimensionality argument. We expect the EEG signals to span only a small number of bases. This not only is consistent from the perspective of dipole model, but it can be validated further by analyzing the non-white continuous EEG data acquired from outside the scanner, which have low intrinsic dimensionality. Furthermore, the variation of coefficients across different segments (rows) may be due to phase changes, which we attempt to preserve: Segments with similar phases would correspond to similar distribution patterns of significant coefficients, as the bases

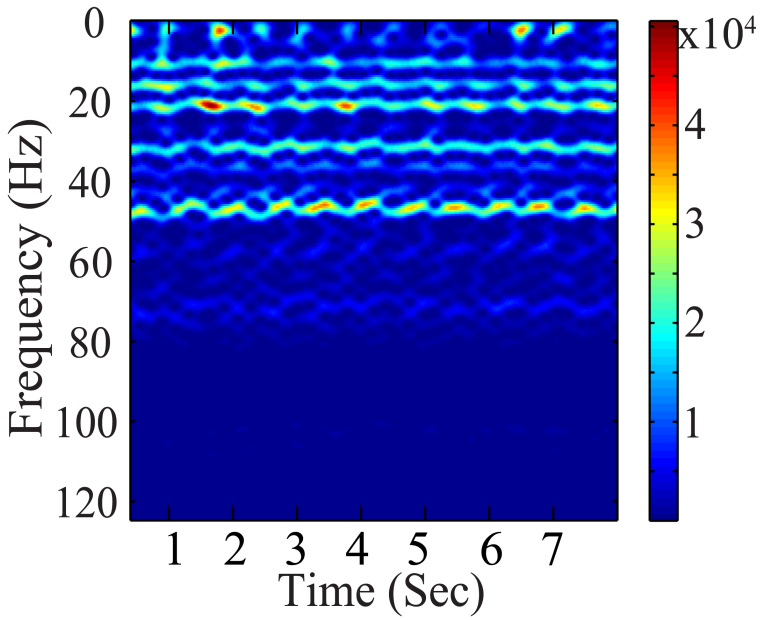

Figure 2.4: Spectrogram (μV^2) of BCG artifacts (from one channel)

are the same for all segments. Therefore, 1) each EEG segment should be represented as the superposition of a few bases (corresponding to sparsity along column direction of the coefficient matrix); and 2) the distribution of the significant coefficient values is dense along the temporal (segment-indexing) direction, represented as dense rows, because the same bases are involved in the generation of phase shifts. These considerations gave rise to a structural regularization of the group-sparsity type [DYZ11] whose columns are sparse, and whose rows are dense. Mathematically, this can be achieved by imposing a weighted group sparsity penalty with $\ell_{2,1}$ norm, $\|\mathbf{C}_e\|_{2,1} \stackrel{def}{=} \sum_{i=1}^{m} \|\mathbf{C}_e[i,:]\|_2$, on the reconstructed EEG coefficient $\mathbf{C}_e$, where m is the number of rows in $\mathbf{C}_e$. Given these considerations, we expect the group-sparsity regularization to help steer the coefficient estimates towards a more favorable reconstruction.

2.7.2 Objective Function

Let $\mathbf{Y}$ denote the contaminated data from a target channel, A, with unknown BCG component, $\mathbf{X}_b$, and unknown EEG component, $\mathbf{X}_e$. A neighboring channel, B, is blocked, and its BCG-only signals are recorded concurrently to provide prior BCG basis $\mathbf{B}_{b\_prior}$, and

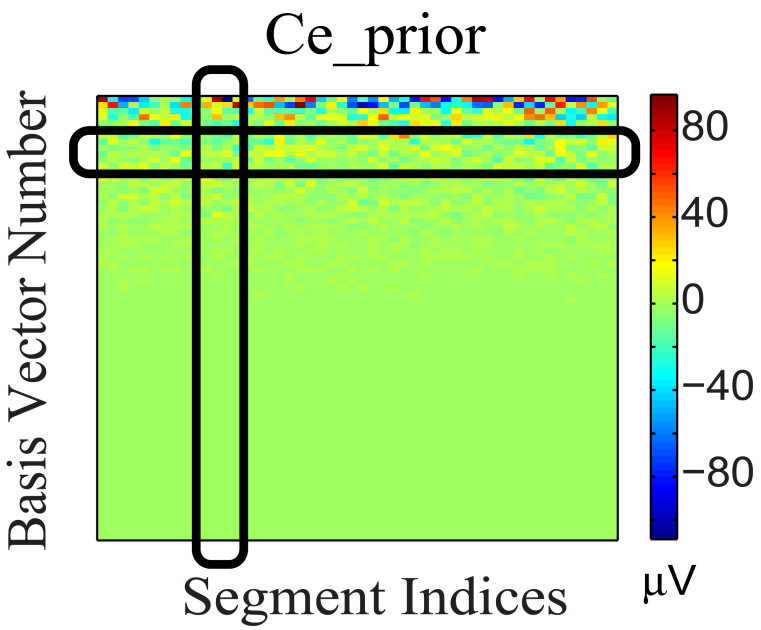

Figure 2.5: Coefficient matrix ($\mathbf{C}_{e\_prior}$) of the EEG prior data. The black column and row highlights show that $\mathbf{C}_{e\_prior}$ is sparse in basis vector representation (column) and dense across segments (row).

coefficients $\mathbf{C}_{b\_prior}$. The prior EEG basis, $\mathbf{B}_{e\_prior}$, (from either channel A or B) comes from the recordings made in experimental session I. These considerations yield an overall reconstruction model:

$$\begin{aligned} &\min_{\mathbf{C}_b, \mathbf{C}_e} \lambda \left\| \mathbf{C}_{b\_prior} - \mathbf{C}_b \right\|_F^2 + \left\| \mathbf{C}_e \right\|_{2,1} \\ &\text{s.t.} \mathbf{Y} = \mathbf{B}_{b\_prior}\mathbf{C}_b + \mathbf{B}_{e\_prior}\mathbf{C}_e \end{aligned} \tag{2.3}$$

where λ is a parameter to balance the BCG and EEG prior contributions. We apply the alternative direction method of multipliers (ADMM) to solve the augmented Lagrangian problem of our reconstruction model (see the supplementary material). After obtaining the estimated coefficients ($\mathbf{C}_b$ and $\mathbf{C}_e$), we proceed to recover the BCG and EEG of target channel A by multiplying those with the basis vectors from the training data,

$$\begin{aligned} \hat{\mathbf{X}}_b &= \mathbf{B}_{b\_prior}\mathbf{C}_b, \\ \hat{\mathbf{X}}_e &= \mathbf{B}_{e\_prior}\mathbf{C}_e. \end{aligned} \tag{2.4}$$

2.8 Results from Synthesized Contaminated Data

To evaluate different artifact removal approaches quantitatively, and to provide parameter selection guidance when real contaminated data is used, we simulated contaminated EEG data from known BCG-only and EEG-only recordings according to the generative model, allowing direct comparison between reconstructed and ground-truth component signals. First, we selected k_1 segments of EEG-only signals as ground-truth EEG (the red EEG recordings in Figure 2.6), denoted as $\tilde{\mathbf{X}}_e \in \mathbb{R}^{m \times k_1}$, which were acquired from one unblocked channel A outside the scanner in session I. Then, the ground-truth BCG-only signals, denoted as $\tilde{\mathbf{X}}_b \in \mathbb{R}^{m \times k_1}$, were chosen from the acquisition of channel A from inside the scanner in session II. Finally, the contaminated data, denoted as $\tilde{\mathbf{Y}} \in \mathbb{R}^{m \times k_1}$, were synthesized according to the generative model $\tilde{\mathbf{Y}} = \tilde{\mathbf{X}}_b + \tilde{\mathbf{X}}_e$. Figure 2.6 illustrates this process. Notice that the EEG-only signals, $\tilde{\mathbf{X}}_{e\_prior}$, were from either channel A or B (a neighbor of channel A) recorded at a time different than that used for EEG data, $\tilde{\mathbf{X}}_e$, in simulating the contaminated data $\tilde{\mathbf{Y}}$; BCG prior data, $\tilde{\mathbf{X}}_{b\_prior}$, were collected at the same time as $\tilde{\mathbf{X}}_e$ and $\tilde{\mathbf{X}}_b$, but from channel B.

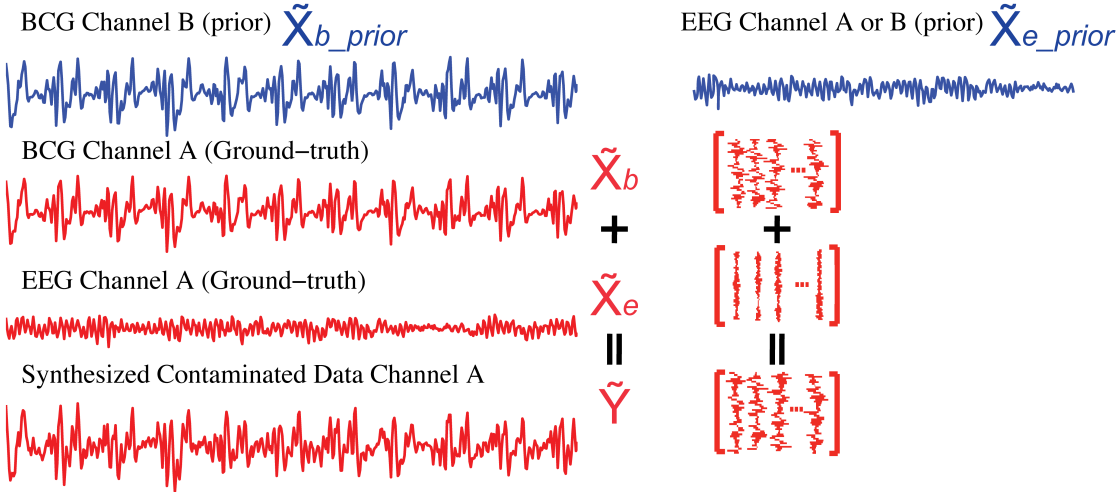

Figure 2.6: We use the BCG data from channel B (blue) as the prior BCG data denoted as $\tilde{\mathbf{X}}_{b\_prior}$ after alignment. The EEG data from channel A or B (blue) can be used as the prior EEG data $\tilde{\mathbf{X}}_{e\_prior}$. Simulated contaminated data ($\tilde{\mathbf{Y}}$) is summed from the BCG ($\tilde{\mathbf{X}}_b$) and EEG ($\tilde{\mathbf{X}}_e$) data (red) both from channel A.

2.8.1 Assessment of validity of orthogonal assumption between subspaces

To demonstrate the limitation of OBS, and to motivate our effort to develop a more realistic and data-driven approach in DRPE, we first checked the relationship of the BCG and EEG subspaces. The OBS method generates bases from contaminated data, and its reconstruction follows the assumption that the first several sequential PCs approximate the subspace of the BCG. The residual of projecting onto the span of segment-wise mean, and the PCs, yields the EEG component. This rationale assumes implicitly that the BCG and EEG subspaces are approximately orthogonal. Without ground-truth BCG- and EEG-only signals, there is no good way to test the feasibility of the assumption. Our experimental data from Sect. 2.4 provides observations of these BCG- and EEG-only signals, and offers an opportunity to examine the validity of the assumptions of OBS, and to explore further methodological improvements. In Figure 2.7 we show the multiplication ($\mathbf{B}_{b\_prior}^{\intercal}\mathbf{B}_{e\_prior}$) result from up to 40 of the BCG and EEG basis vectors (PCs) from prior BCG and EEG data, $\tilde{\mathbf{X}}_{b\_prior}$ and $\tilde{\mathbf{X}}_{e\_prior}$. The $[i,j]^{th}$ element value of this matrix is the inner product of the i^{th} basis of BCG and the j^{th} basis of EEG. Complete orthogonality of the EEG and BCG subspaces would correspond to a matrix containing only zero elements. The fact that the matrix of Figure 2.7 contains many significant values of PC interaction, especially in its upper left corner, indicates that the assumption of orthogonality of the BCG and EEG subspaces is invalid, and necessitates the development of denoising methods beyond OBS.

2.8.2 Performance Evaluation of Reconstruction

We quantified the signal separation performance of DRPE and OBS method, in terms of relative error RE, defined as $RE = \|\hat{\mathbf{X}} - \mathbf{X}_{truth}\|_F / \|\mathbf{X}_{truth}\|_F$. Recovered BCG and EEG components, and their corresponding ground-truth, are represented with $\hat{\mathbf{X}} \in \mathbb{R}^{m\times k_1}$ and $\mathbf{X}_{truth} \in \mathbb{R}^{m\times k_1}$, respectively. The results from the DRPE method were derived with parameters ($\lambda = 10^{-2.4}$, $\beta_1 = 10^{-6.4}$ and $\beta_2 = 10^{4.2}$), and all of the results of the OBS method were obtained from the OBS implementation in the EEGLAB plug-in fMRI version 1.2 [NBI05] with the number of PCs (including the mean vector) set to 3 (N_{pc}=3). The contaminated

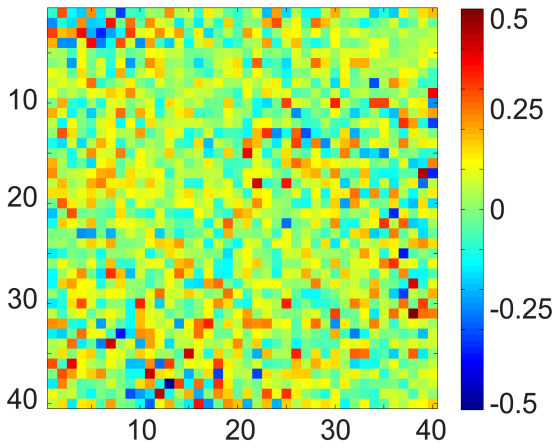

Figure 2.7: Matrix product of the normalized BCG and EEG basis vectors using up to 40 PCs. In fully orthogonal subspaces the expected value of al elements would be zero, whereas here the values are large.

data were simulated from 13.6-minute BCG-only and EEG-only data both from channel A. We learned the prior BCG basis vectors from BCG-only data concurrently from a neighboring channel, B, and learned the prior EEG basis vectors from non-concurrent EEG-only data from channel B from a different 8.9-minute time segment. To reduce the computational burden, we down-sampled all data from 250Hz to 50Hz (with an anti-aliasing filter as explained in Sect. 2.5.) After aligning the recordings to the detected heartbeats, the resulting data from the 13.6-minute, and 8.9-minute, recordings were re-formed as matrices of size 73×848 and 73×556 respectively. Figure 2.8 shows a typical portion of the reconstructed results from the two methods, alongside the ground-truth data. Figure 2.9 shows the corresponding frequency spectra. It is clear that the BCG and EEG components are much better separated and preserved by the DRPE method; the relative errors for EEG components are reduced by approximately 7-fold. Figure 2.8 shows as well that the DRPE successfully recovers the qualitative temporal behavior of the EEG signals much better than does OBS.

We further employed a standard 3-fold cross-validation [FHT01] to quantify the overfitting and the consistency of our DRPE method, and compared the results to that of OBS (with $N_{pc} = 3$). Letting $Y^{(1)}$ denote a 73×251 (4.5-minute) matrix containing a randomly selected subset of column vectors from synthesized contaminated matrix $\mathbf{Y}$ (13.6-minute),

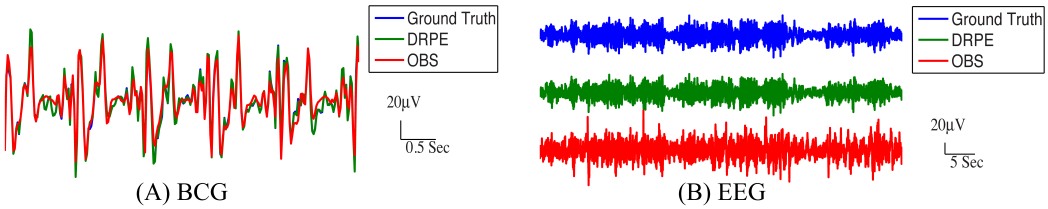

Figure 2.8: Comparison of the reconstruction results from DRPE and OBS. Ground truth, DRPE and OBS results are shown in each panel. The DRPE method yields only 6.685% and 16.45% relative errors for the BCG and EEG reconstruction, while the OBS generates 47.50% and 117.5% relative errors for BCG and EEG. The reconstructed BCG (A) from DRPE almost overlaps with the Ground truth BCG. The large spikes in reconstructed EEG (B) from OBS are due to the residual BCG signals.

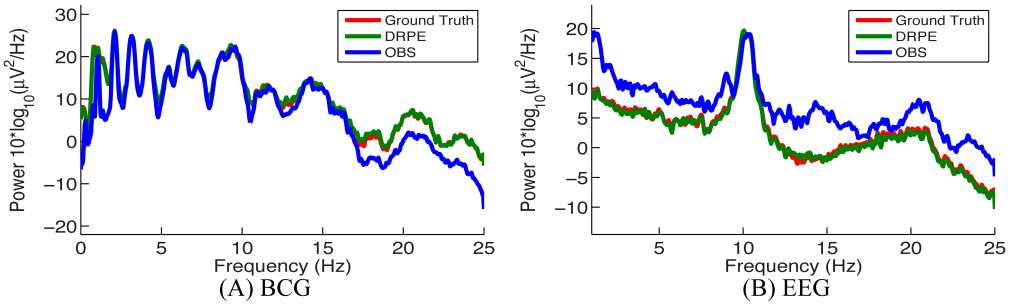

Figure 2.9: Comparison of the frequency spectra of reconstructed BCG and EEG signals from the DRPE and the OBS methods as well as their corresponding ground-truth data.

and letting $\bar{\mathbf{Y}}^{(1)}$ be a 73×607 matrix (9.1-minute) containing the complementary set of data vectors used for training parameters we then applied DRPE and OBS to recover BCG and EEG components from the $\bar{\mathbf{Y}}^{(1)}$. The parameters (λ, β_1 and β_2) of the DRPE were tuned for the best recovery of the EEG components. Once the optimal parameters were determined for the training dataset $\bar{\mathbf{Y}}^{(1)}$, they were used in recovering the BCG and EEG signals from the validation dataset $\mathbf{Y}^{(1)}$. The process was then repeated using 3 non-intersecting subsets of the data to calculate reconstruction errors of the training and validation for each subset. The relative errors of the cross-validation process are listed in Table 2.1. Selected parameters in the table are relatively consistent, and result in similarly good reconstruction results for all the training sets, with only slightly worse results for the validation sets. This strongly

Table 2.1: Cross validation results from 3 groups: Relative Errors (RE) in percentage. Each group has a different segment as validation set with the remaining two segments as training set.

	DRPE							OBS			
	BCG Segments		EEG Segments		Parameters			BCG Segments		EEG Segments	
$RE(\%)$	T	V	T	V	$\log_{10}\lambda$	$\log_{10}\beta_1$	$\log_{10}\beta_2$	T	V	T	V
Group 1	6.66	6.90	16.53	17.18	-2.2	-6.2	-3.6	52.31	61.50	130.5	153.5
Group 2	6.78	6.96	16.69	16.98	-2.2	-6.2	-4.2	52.47	61.54	129.9	150.6
Group 3	6.70	6.88	16.42	16.90	-2.2	-6.2	-4.2	51.97	61.02	128.0	150.5

T: Training Session. V: Validation Session

β_1 and β_2: penalty parameters for the corresponding augmented Lagrangian problem (See Supp. Material).

suggests that the DRPE method is stable, with nearly negligible overfitting.

2.9 Results from Real Contaminated Data

One of the most robust effects on the EEG results from signal comparisons of eyes-closed (EC) and eyes-open (EO) states at rest, which results in large alpha band increases in the EC condition [Ber29]. Without access to ground-truth EEG-only signals acquired inside a scanner, we demonstrated the feasibility and advantage of our DRPE method on real contaminated data in an EC/EO paradigm using parameters selected from the same simulation process above, whose contaminated data was composed of EEG-only signals acquired outside the scanner, and BCG-only signals acquired *inside* the scanner.

2.9.1 Experimental Setup

We acquired new data for both experiment session I and II when the subject was cued verbally to open and close his or her eyes every 30 seconds, for a total time of 15 minutes

for each session.

2.9.2 Statistical Analysis

We followed the procedure of Chen and colleagues [CFZ08] to quantify the EC/EO effects. Each 30-sec EEG sample, omitting 2-sec before and after each EC/EO event onset, was analyzed in 3 sec epochs, resulting in 112 epochs for each EC/EO state, from a total 14-minute recordings. The absolute EEG band power (μV^2) in the alpha band from each epoch of EC/EO state was calculated using the Fast Fourier Transform. As the alpha band power values failed a normality test, Wilcoxon test for nonparametric comparison of ranks was performed, with $p < 0.05$ accepted as significant, to assess the hypothesis that EC and EO states have similar population mean rank based on alpha band power [CFZ08].

2.9.3 Effects of States from Reconstructed Signals

Figure 2.10 shows the reconstructed EEG signals from real contaminated data of channel 124 with prior BCG and EEG data sampled from neighboring channel 137. Parameters used in reconstruction were selected from the simulation process, but using the new BCG- and EEG-only data from experiment sessions I and II. The differences in alpha energy between the EC to EO states can be identified clearly at around 30s, 60s, 90s... as the subject closed and opened his eyes. With both the BCG and EEG prior data from the neighboring channel, the reconstructed EEG signals of channel 124 from the DRPE method have shown more prominent distinctions than OBS, between the EC and EO states.

When the contaminated data were used (EC: mean 342.0, median 328.0μV^2, EO: mean 325.1, median 310.2μV^2; $p = 0.09 > 0.05$), our test indicated no significant reduction in the alpha band power in the EO, as shown in Figure 2.11(A). By contrast, statistically significant differences (Figure 2.11(B)) between the EC and EO states were present in the magnitude of the alpha band power in the recovered EEG signals from OBS (EC: mean 73.95, median 66.87μV^2, EO: mean 54.02, median 45.59μV^2; $p = 0.0036 < 0.05$), agreeing with the results in the original OBS paper [NBI05]. In addition, the EEG signals estimated from DRPE also

reveal statistically significant difference (Figure 2.11(C)) between the EC and EO states (EC: mean 26.23, median 26.07μV^2, EO: mean 14.93, median 11.38μV^2; $p = 1.9 \times 10^{-7} < 0.05$). To test the robustness of the DRPE method in terms of basis characterization, we have (1) applied EEG prior acquired from one subject to the BCG denoising for another subject, (2) used EEG prior acquired in a normal EEG room without the mock scanner. For the DRPE method, the EEG prior signals from two other subjects were also employed, both of which were acquired when subjects lying in a normal EEG room without mock scanner. A spectrogram of the EEG signals, and the corresponding Wilcoxon test results, are displayed in Figure 2.11.

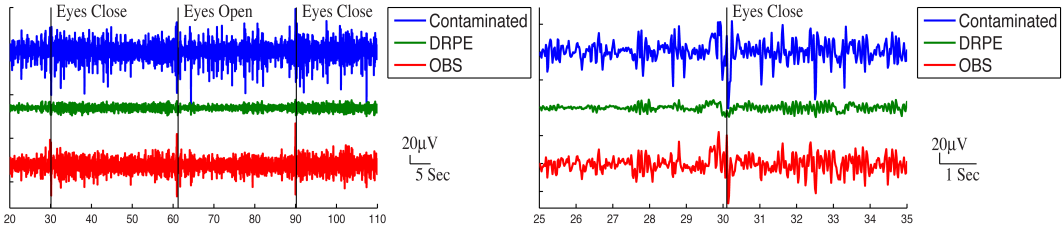

Figure 2.10: Roughly 90-sec and 10-sec ranges of reconstructed EEG signals (in μV) were shown here with events (eyes open (red) and eyes close (green)). In (A) and (B), top panel: reconstructed EEG signal from the DRPE method. Bottom panel: reconstructed EEG signals from the OBS method.

2.10 Discussion and Conclusions

Removing BCG artifacts from contaminated EEG data is a major bottleneck for the successful integration of simultaneously recorded data. First, the BCG component (magnitude>200μV) often dominates the EEG component (10-100μV) in the contaminated signal by an order of magnitude [YMG10]. Second, the BCG artifacts show considerable temporal variation as shown in Figure 2.5 [HBM95, BPJ02, DSS07]. Third, the BCG and EEG subspaces have a complex geometric relationship with nontrivial overlap that violates the assumption of simple mutual-orthogonality (c.f. Sect. 2.8.1) making common approaches, such as PCA, both inappropriate and ineffective. Finally, unless ground-truth BCG data are accessible, overfitting

and relative error of recovered signals cannot be quantified directly [NBI05, GVK07, VDR10].

When both BCG and EEG signals exist, accurate representations of the subspaces are necessary to decompose contaminated signals. Powerful, and widely used, the optimal basis sets (OBS) method of Niazy derived the subspace representations solely from contaminated signals, but it relies on questionable presumptions (e.g., orthogonality) about the BCG and EEG subspaces. By contrast, our procedure enables separate access to BCG and EEG subspaces, providing more accurate basis vectors for the purpose of reconstruction. Our DRPE approach is based on the assumption that, in the case of continuous spontaneous EEG experiments, the EEG basis learned from outside the scanner is a sufficient representation of the EEG component measured inside the scanner. This allows us to facilitate the separation of BCG and EEG using prior knowledge of the coefficient structures of the EEG, and neighboring BCG-only, signals. Moreover, we have demonstrated (Figure 2.11) that the EEG bases learned from different subjects and acquisition environment are sufficiently consistent for effective denoising. We recognize that the challenges of ERP signals and continuous EEG signals differ: with knowledge of triggering event timing information, we are designing a different type of prior and objective function to take advantage of the problem structures. One possible limitation of the present work lies in the additive generative model of the contaminated data in Equation (2.1). While we cannot verify this directly, there is little reason to believe that strong interactions couple EEG and BCG in the biologically recorded signals. The effectiveness of recovering EEG signals is demonstrated here by its application to real contaminated data from an eyes open/eyes closed study with denoising parameters tuned from the simulation study.

In addition to providing more representative basis vectors, the DRPE method yields a novel means to introduce structures on the coefficient sets. In particular, penalty functions are designed to regularize the temporal pattern of the BCG by the ℓ_2-norm, and the group characteristics of EEG coefficients by $\ell_{2,1}$-norm. The feasibility of enforcing ℓ_2 and $\ell_{2,1}$-regularizations is demonstrated qualitatively and quantitatively by our studies on both simulated and real contaminated data. In our evaluation of the contaminated data simulated from BCG-only and EEG-only signals, the relative errors of the reconstructed BCG and EEG

data are as low as 6.685% and 16.45%, compared to 47.50% and 117.5% from the benchmark OBS method. Notably, both the BCG and EEG priors are acquired from an adjacent channel, while the EEG priors were obtained from outside the scanner. This demonstrates that the prior data is relatively insensitive to small spatial location changes across different experiment sessions. It suggests also the potential of extending this result to the whole head, by creating blocking patterns that provide multiple BCG channels. Our recording configuration is compatible with various blocking patterns, and we are in the process of evaluating the merits of different options.

Moreover, the DRPE method can be integrated with other approaches that generate BCG reference signals – some potential candidates are the more recently developed reference layer artifact subtraction (RLAS) method [CMG14] and others [BPJ02, MAF07] which have provided alternative means to record BCG reference signals. Admittedly, there exists some discrepancy between each of these reference signals and the "ground-truth" BCG signals, as a result of either insulation or sensing process. While these signal differences become the limiting error term [UD10] when used simply for linear subtraction, DRPE utilizes the reference signals as statistical priors, and flexibly compensates this discrepancy with the incorporation of priors built on continuous EEG from outside the scanner. The RLAS method potentially will alleviate the needs to find consistent neighboring channels that provide BCG reference for the DRPE method. In principal, Hall effects occurring in the MR imaging field might distort the scalp topography of the EEG signals. It is difficult to estimate the magnitude of this contaminant, which is common to OBS and DRPE.

Our recording configuration enables quantitative comparison of various artifact removal techniques. We used the Frobenius-norm $\|A\|_F = \sqrt{\sum_{i=1}^{m}\sum_{j=1}^{n}|a_{ij}|^2}$, which resembles the root mean square error, to quantify the difference between reconstructed signals and their corresponding source signals. The relative errors facilitate the comparison of the results among different signal type. Here, we used this approach, and K-fold cross-validation, to quantify and compare the DRPE and OBS methods.

Although PCA is used in this paper to generate the basis matrix for each of the EEG and BCG subspace representations, other representations, such as ICA, can be substituted

without affecting the integrity and compatibility of the recording configuration for subspace-specific data collection and the reconstruction process, though different basis representation may give rise to different coefficient behavior, and the objective function of equation (2.5) would need to be designed accordingly. We expect different choices of basis representation to affect the reconstruction performance, and it is our next step to optimize over such representations.

Preliminary tests have demonstrated the feasibility and efficacy of the proposed approach. There are a few practical issues for the clinical applications of this new method. First, the computational demand is high compared to the OBS method, and subject-specific parameter optimizations may be necessary. The alternating direction method of multipliers (ADMM) we applied in solving the objective function (see the supplementary material) takes 1-2 sec to evaluate each set of parameters. We expect, however, that this problem will yield readily to computational optimizations. Second, the additional time needed to acquire clean EEG data could impose some burdens in clinical or research studies. Improvement of workflow might be able to minimize this impact.

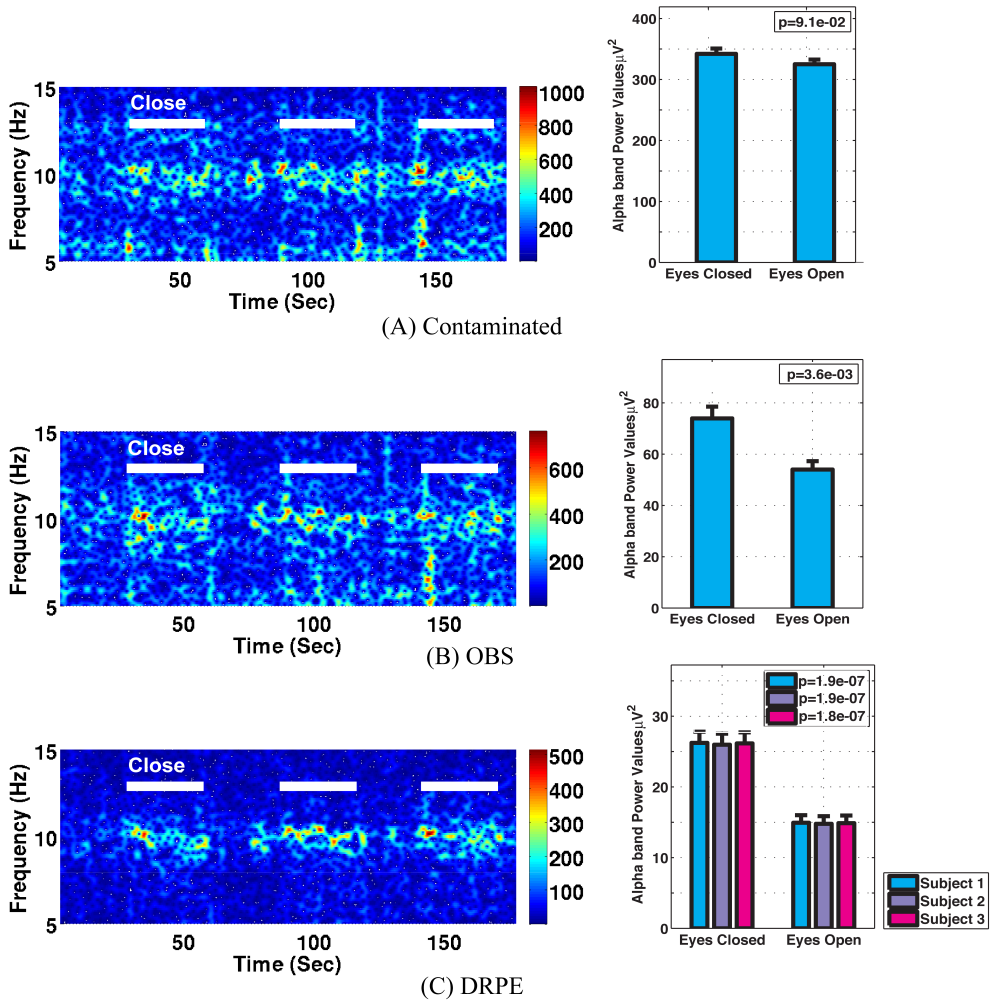

Figure 2.11: Comparison of performance in differentiating the eyes open (EC) and eyes closed (EO) states: (A) based directly on contaminated EEG recording, (B) recovered EEG signals with the OBS method, and (C) the proposed DRPE method. The left panel depicts the reconstructed spectrograms. The right panel displays the Wilcoxon rank test results of alpha band power comparisons between the EO and EC states; standard errors are indicated. No significant change in alpha power was detected in the contaminated signal, while both the DRPE and OBS methods display the expected decreases from EC to EO conditions. In (C), the EC and EO results are compared when the EEG basis was derived from subject 1 (blue) or from subject 2 and 3 (purple and red). The reconstruction results were virtually identical when the EEG bases were derived from the original subject, or from the other two participants, recorded in different environments.

2.11 Supplementary Derivations

We use a split Bregman method [COS09, GO09] (also known as augmented Lagrangian method) to solve this problem. In particular, by introducing an auxiliary variable $\mathbf{Z}$, the primary problem equation (2.5)

$$\begin{aligned} &\min_{\mathbf{C}_b,\mathbf{C}_e} \lambda \left\|\mathbf{C}_{b\_prior} - \mathbf{C}_b\right\|_F^2 + \left\|\mathbf{C}_e\right\|_{2,1} \\ &\text{s.t.} \mathbf{Y} = \mathbf{B}_{b\_prior}\mathbf{C}_b + \mathbf{B}_{e\_prior}\mathbf{C}_e \end{aligned} \tag{2.5}$$

is equivalent to:

$$\begin{aligned} &\min_{\mathbf{C}_b,\mathbf{Z}} \ \left\|\mathbf{Z}\right\|_{2,1} + \lambda \left\|\mathbf{C}_{b\_prior} - \mathbf{C}_b\right\|_F^2 \\ &\text{s.t. } \mathbf{Y} = \mathbf{B}_{b\_prior}\mathbf{C}_b + \mathbf{B}_{e\_prior}\mathbf{C}_e \\ &\quad \mathbf{Z} = \mathbf{C}_e \end{aligned} \tag{2.6}$$

The corresponding augmented Lagrangian problem is of the form:

$$\begin{aligned} &E(\Lambda_1, \Lambda_2, \mathbf{Z}, \mathbf{C}_b, \mathbf{C}_e) = \\ &\left\|\mathbf{Z}\right\|_{2,1} + \left\|\mathbf{C}_{b\_prior} - \mathbf{C}_b\right\|_F^2 - < \Lambda_1, \mathbf{Z} - \mathbf{C}_e > \\ &+ \frac{\beta_1}{2} \left\|\mathbf{Z} - \mathbf{C}_e\right\|_F^2 - < \Lambda_2, \mathbf{B}_{b\_prior}\mathbf{C}_b - \mathbf{B}_{e\_prior}\mathbf{C}_e - \mathbf{Y} > \\ &+ \frac{\beta_2}{2} \left\|\mathbf{B}_{b\_prior}\mathbf{C}_b - \mathbf{B}_{e\_prior}\mathbf{C}_e - \mathbf{Y}\right\|_F^2, \end{aligned} \tag{2.7}$$

where $< ., . >$ is the inner product, Λ_1 and Λ_2 are Lagrange multipliers, while $\beta_1, \beta_2 > 0$ are penalty parameters. We then apply the classic alternating direction method (ADM) to solve the augmented Lagrangian problem with respect to $\mathbf{Z}$, $\mathbf{C}_b$ and $\mathbf{C}_e$ alternately. We stop the iteration as soon as the relative change $\left\|\mathbf{C}_e^{k+1} - \mathbf{C}_e^k\right\| / \left\|\mathbf{C}_e^k\right\|$ between two iterations is less than 10^{-6}. We chose the step length to be 1.618 according to [DYZ11].

In short, we have derived an ADM iteration scheme as follows:

Algorithm: ADM for Group Sparsity

Initialize $\mathbf{Z}, \Lambda_1, \Lambda_2, \beta_1, \beta_2 > 0$, step lengths $\gamma_1, \gamma_2 > 0$

While *stopping criterion is not met* **do**

$$\mathbf{C}_e \leftarrow (\beta_1 \mathbf{I} + \beta_2 \mathbf{B}_{e\_prior}^T)^{-1} \times$$

$$(\beta_1 \mathbf{Z} - \Lambda_1 + \beta_2 \mathbf{B}_{e\_prior}^T (\mathbf{Y} - \mathbf{C}_e \mathbf{C}_b) - \mathbf{B}_{e\_prior}^T \Lambda_2)$$

$$\mathbf{C}_b \leftarrow (2\lambda \mathbf{I} + \beta_2 \mathbf{B}_{b\_prior}^T \mathbf{B}_{b\_prior})^{-1} \times$$

$$(2\lambda \mathbf{C}_{b\_prior} + \mathbf{B}_{b\_prior}^T \Lambda_2 + \beta_2 \mathbf{B}_{b\_prior}^T (\mathbf{Y} - \mathbf{B}_{e\_prior} \mathbf{C}_e))$$

$$\mathbf{Z} \leftarrow shrink(\mathbf{C}_e + \frac{\lambda_1}{\beta_2}, \frac{w}{\beta_2})$$

$$\Lambda_1 \leftarrow \Lambda_1 - \gamma_1 \beta_1 (\mathbf{Z} - \mathbf{C}_e)$$

$$\Lambda_2 \leftarrow \Lambda_2 - \gamma_2 \beta_2 (\mathbf{B}_e \mathbf{C}_e + \mathbf{B}_b \mathbf{C}_b - \mathbf{Y})$$

CHAPTER 3

Coupled Basis Learning and Regularized Reconstruction for BCG Artifact Removal in Simultaneous EEG-fMRI Studies

3.1 Abstract

The ballistocardiogram (BCG) is a major artifact in electroencephalographic (EEG) data acquired inside a magnetic resonance imaging (MRI) scanner, and is several times larger in magnitude than the actual EEG signals. Removing the BCG artifacts remains an unresolved challenge, especially in studies of continuous EEG recordings. In this work, we propose a Direct Recording Joint Incoherent Basis (DRJIB) method to decompose the observed noisy EEG measurements into BCG and underlying EEG components. We compare its preliminary performance quantitatively with that of the benchmark Optimal Basis Set (OBS) method. Without assuming orthogonality or independence of the BCG and EEG subspaces, as in conventional methods, our approach learns the bases faithfully from BCG-only and EEG-only signals acquired from a new experimental setup. Specifically, to promote subspace separability, a paired set of low-dimensional and semi-orthogonal (BCG, EEG) basis representations is obtained by minimizing a cost function consisting of group sparsity penalties for automatic dimension selection and an energy term for encouraging incoherence. Reconstruction is subsequently obtained by fitting the contaminated data to a generative model using the learned bases subject to regularization. In the challenging non-event-related continuous EEG studies, our DRJIB method outperforms the OBS method by nearly 7.5-fold in separating and preserving the continuous BCG and EEG signals.

3.2 Introduction and Motivation

Simultaneous electroencephalography (EEG) and functional magnetic resonance imaging (fMRI) has become a widely used and exciting approach for studying different yet connected aspects of cerebral activity, particularly bioelectric and haemodynamic attributes. With different temporal and spatial resolutions, concurrently acquired EEG and fMRI data are considered to hold complementary yet functionally linked information regarding the underlying brain activities. This multi-modal approach has proven its value in numerous applications such as the study of ongoing brain rhythms [GSE02], the analysis of event-related brain responses [DUS06, DUS05, ECM08, MEN08, MJS04]. Despite the many reported successful examples in the neurosciences, current investigations are still limited by the quality of the EEG data acquired inside the scanner.

While artifacts introduced to the simultaneously acquired MRI data are relatively easy to manage [HBM95, GSE00], artifacts appearing in the EEG data recorded inside the scanner presents a more challenging obstacle. The most prominent magnetically-induced artifact is called ballistocardiogram (BCG). BCG is difficult to suppress especially in studies of continuous recordings such as studies of ongoing spontaneous brain rhythms. It has been suggested [YMG10, MHB13] that BCG is related to cardiac cycles and magnetic field strength. In event-related experiments, residual artifacts would be damped by averaging around events as the events are generally designed to be randomly distributed with respect to the cardiac cycles. In experiments at lower field strength, the BCG is significant lower in magnitude than the ones generated at higher field strength, since the BCG amplitude scales with field strength. This explains the consideration variation of success levels among studies, with more successful applications achieved at event-related studies and lower field strength.

The most widely used means of suppressing the BCG artifacts is the optimal basis sets (OBS) method [NBI05]. It applies principal component analysis (PCA) to the contaminated EEG data and removes the primary (usually 3) principal components as contributions from BCG artifacts. PCA-based source separation methods are implicitly based on that the BCG and EEG subspaces are orthogonal, as indicated by partitioning the PCs sequentially. Not

only PCA-related methods, other existing methods such as the ICA-related blind source separation [MPC07, BGB06] and the spatial-filtering of the EEG measurements [BMS08] have a commonality that BCG and EEG components are directly extracted from contaminated EEG measurements with no, or minimal characterizations of the true subspaces of the underlying BCG and EEG components.

By contrast, we propose a framework to address the BCG removal challenge from the perspective of signal separation where the underlying components are well represented with a set of learned basis vectors. The first stage of the proposed framework aims to generate the BCG and EEG bases that are least correlated with each other while remain faithfully and sparsely in representation of the BCG/EEG-only signals. To do so, we insert a group sparsity term for the coefficients to encourage sparse representation and add a basis/dictionary incoherence term that promotes the incoherence between the BCG and EEG bases, inspired in part by the works from Ramiriez, et al. [RSS10].

In the second stage, we reconstruct the BCG/EEG signal by estimating the coefficients of the corresponding learned bases, while the group sparsity structures of the coefficients are taken care of by a column reduction operation. With our special experimental setup where BCG-only signals are collected simultaneously with contaminated signals but from different yet adjacent channels, the complexity of modeling the non-stationary temporal variations of the BCG signals has greatly reduced by directly enforcing the similarity of the BCG coefficients from adjacent channels with the same BCG basis.

In summary, our DRJIB method consists of two phases: (1) a basis-learning phase where the bases for BCG and EEG signals are optimized jointly to sparesly represent the BCG-only and EEG-only signals, and to be as independent as possible with an incoherence term in order to promise better signal separability; (2) a reconstruction phase where the underlying BCG and EEG components are estimated from the contaminated EEG measurements using the learned bases and regularization terms on the structures of the coefficients.

The rest of the paper is organized as follows. Sect.3.3.1 introduces an assumption upon which we construct the simulation of the contaminated EEG data in order to quantitatively

compare the results of different artifact removal methods. Sect.3.3.2 provides an introduction to our newly developed experimental setup that collects BCG/EEG-only data as priors for the purpose of basis learning. The preprocessing of the collected measurements is discussed in Sect.3.3.3 along with the simulation of the contaminated data. In Sect.3.3.4 we describe the optimization framework with an objective function that encodes low-dimensional subspace modeling and incoherence regularization. Reconstruction with coefficient regularization is reported in Sect.3.3.5. Results and discussions are given in Sect.3.4.

3.3 Methods

3.3.1 Generative Model for Contaminated EEG Data

It is reasonable to assume that the BCG artifacts and the normal brain EEG signals are generated from independent sources. Thereby, the noisy measurements can be modeled as their superposition subject to noise contamination, according to

$$y = x_{bcg} + x_{eeg} + \text{noise}, \tag{3.1}$$

for data from one channel, where y, x_{bcg}, x_{eeg} and noise $\in \mathbb{R}^n$, n is the time length of recordings. y denotes simulated contaminated measurements from a channel while $x_{bcg}$and x_{eeg} denote the BCG-only and EEG-only data, respectively.

3.3.2 Experimental Setup

3.3.2.1 Acquisition of EEG-only data:

Outside the scanner room, the subject lay comfortably on a carpet with a blanket and a pillow made of viscoelastic foam placed under the subject's head. Recordings were carried out in a quiet, electromagnetically shielded room kept in the dark while the subject rested quietly with the eyes closed and without falling asleep during the whole acquisition. This protocol was designed to record spontaneous brain activity with the focus on the spontaneous variations of the alpha rhythm.

3.3.2.2 Acquisition of BCG-only data:

Inside the scanner, it is desirable to collect BCG artifacts only signals from a subset of channels to generate prior information for modeling the BCG artifacts for the rest of the channels. To realize that, two layers of material were inserted between the scalp and the electrodes.

Insulating Layer: To collect only BCG artifacts, we isolated a subset of electrodes from the scalp with a plastic insulating barrier as shown in Fig.3.2(a). The purpose of the insulating layer is to block brain signals from conduction.

Semi-conducting Layer: In order to properly collect signals from insulated electrodes, a semi-conductive layer was inserted between the insulating layer and electrodes. We chose a piece of dampened thin paper as the semi-conductive layer, providing proper impedance to avoid any short circuit or alteration of BCG signals. As shown in Fig.3.1(a), the impedance measured from the blocked electrodes were mostly 20kΩ, on the same level of the impedance measured from the other unblocked electrodes, ensuring the collection of unaltered BCG-only signals.

(a) (b)

Figure 3.1: Experimental Setup: (a) Topographic map of measured impedance (kΩ) of the electrodes with two layers inserted (b) Inserted Two Layers between electrodes and head

3.3.2.3 Acquisition of Contaminated EEG data:

Inside the scanner, the unblocked channels record actual experiment EEG data that were corrupted by the BCG artifacts. As shown in Fig. 3.1(b), this experimental configuration acquires the contaminated EEG data as well as simultaneous BCG-only artifacts from different set of channels inside the scanner. As most traditional experiments used conventional 10-20 EEG system (20 channels) to investigate the spontaneous brain rhythms, we chose to block 236 out of the 256 channels, leaving 20 channels unblocked. As shown in the enlargement in Fig. 3.2(b), each unblocked channel was surrounded by multiple blocked channels. We chose this electrode blocking pattern mainly out of its simplicity to demonstrate the feasibility of our new framework. Other blocking patterns with the majority of channels unblocked will be compared and discussed in our next paper.

3.3.3 Data Preprocessing

Following the preprocessing procedure in [NBI05] with EEGLAB plug-in fMRI version 1.2, the slow drifts were first removed with a high pass filter (cutoff=1Hz). Let $x \in \mathbb{R}^n$ be the filtered data from one channel. Then x was divided into k columns according to retrieved heartbeats from ECG channel when $x_i \in \mathbb{R}^m$ is the i^{th} column and m is the number of time points of the signal segment which is centered around the heartbeat and 1.5 times the median length of detected R-R intervals. After aligning all segments into a matrix $\tilde{\mathbf{X}} = [x_1|x_2 \ldots |x_k] \in \mathbb{R}^{m \times k}$, the mean effect $\bar{x} = \frac{1}{k}\sum_{i=1}^{k} x_i \in \mathbb{R}^m$ was calculated and removed from the data matrix, resulting the residual artifacts $\mathbf{X}$. The same procedure was applied to all collected data including BCG-only, EEG-only and contaminated recordings. Note that

(a) (b)

Figure 3.2: Diagram of the inserted two layers

the alignment to the heartbeats facilitates learning of the BCG basis by reducing the data complexity caused by the non-stationary heartbeats, it has no obvious advantage for the EEG data.

Unlike the OBS method, where the mean effect along with the first several PCs were fitted to, and subtracted from each segment of contaminated data, $\tilde{\mathbf{Y}}$, to generate the estimated EEG signals, our method operated by separating the demeaned BCG $\mathbf{X}_b$ and EEG $\mathbf{X}_e$ matrices from the demeaned contaminated data $\mathbf{Y}$. The mean effect from $\tilde{\mathbf{Y}}$ was added back to the recovered BCG matrix, assuming, as does the OBS method, that the EEG signals are close to zero-mean since EEG segments should be relatively uncorrelated with the heartbeats.

We use $\mathbf{X}[:, j]$ to denote the j^{th} column vector and $\mathbf{X}[i, :]$for the i^{th} row vector of matrix $\mathbf{X}$. Subscripts are used to indicate the type of signals. As prior information for the BCG and EEG signals, the pure BCG from one channel (B) in the session II is denoted as $\mathbf{X}_{b_prior} \in \mathbb{R}^{m\times k_1}$and the EEG in session I from another channel (A or B) is denoted as $\mathbf{X}_{e\_prior} \in \mathbb{R}^{m\times k_2}$. From a channel that is adjacent to the contaminated channel we chose the BCG prior data as well as the BCG data used in the following simulation, to minimize spatial variations of the BCG artifacts. This adjacent channel was also away from major surface vessels.

3.3.4 Basis Learning

We aim to generate a pair of full-rank bases: $\mathbf{B}_{b\_prior}$ and $\mathbf{B}_{e\_prior} \in \mathbb{R}^{m\times m}$, respectively, such that (1) they properly represent the BCG-only $\mathbf{X}_{b\_prior}$ and EEG-only prior data $\mathbf{X}_{e\_prior}$, (2) they span subspaces that are as orthogonal to each other as possible, yet allow intersection when strongly supported by data, and (3) their intrinsic dimensions are low. To this end, we consider the following optimization problem:

$$\begin{aligned}\min_{\mathbf{B}_{b\_prior},\mathbf{B}_{e\_prior}} \quad & \frac{\beta_1}{2}\left\|\mathbf{X}_{b\_prior}-\mathbf{B}_{b\_prior}\mathbf{C}_{b\_prior}\right\|_F^2 \\ & +\frac{\beta_2}{2}\left\|\mathbf{X}_{e\_prior}-\mathbf{B}_{e\_prior}\mathbf{C}_{e\_prior}\right\|_F^2 \\ & +\left\|\mathbf{C}_{e\_prior}\right\|_{2,1}+\lambda\left\|\mathbf{C}_{b\_prior}\right\|_{2,1} \\ & +\mu\left\|\mathbf{B}_{b\_prior}^T\mathbf{B}_{e\_prior}\right\|_F^2,\end{aligned} \tag{3.2}$$

where $\mathbf{C}_{b\_prior}$ and $\mathbf{C}_{e\_prior} \in \mathbb{R}^{m\times k}$, and λ is a scalar balancing the contribution of group sparsity penalties. β_1 and β_2 are also scalars ensuring the contribution of data fidelity terms. And μ is a scalar controlling the orthogonality enforced to the learned bases.

In Eqn.3.2, the first two data fidelity cost terms ensure proper representation of the prior data. The $\ell_{2,1}$-norm defined as $\|\mathbf{Z}\|_{2,1} \stackrel{def}{=} \sum_{i=1}^{m} \|\mathbf{Z}[i,:]\|_2$ where $i \in \{1,...,m\}$ is an index set corresponding to the i^{th} group (row), and m is the number of rows in $\mathbf{Z}$. The $\ell_{2,1}$-norm encourages group sparsity structure on the coefficients of the $\mathbf{C}_{b\_prior}$ and $\mathbf{C}_{e\_prior}$, leading to the concentration of significant values to a few rows of the coefficient matrices. This structure effectively "nullifies" the contribution of the basis columns corresponding to the insignificant rows of the coefficient matrices, and results in low-dimensional representations of the BCG and EEG subspaces. Motived by incoherent dictionary learning in Ramirez, et al.[RSS10], we use $\left\|\mathbf{B}_{b\_prior}^T \mathbf{B}_{e\_prior}\right\|_F^2$ to penalize the coherence between the two bases and encourage the orthogonality of the spanned subspaces for the purpose of signal separation.

In practice, the BCG and EEG subspaces are neither orthogonal nor independent. Therefore, large enough subspaces intersection should be allowed even though we encourage incoherence during basis learning. Thus, overly heavy weight to the incoherence term tends to falsely enforce orthogonal structures on the insignificant basis vectors, resulting in lower the separability of the two signals for later reconstruction phase.

Based on the $\ell_{2,1}$-norm promoted sparse entries of $\mathbf{C}_{b\_prior}$ and $\mathbf{C}_{e\_prior}$, we perform an explicit column reduction in the reconstruction stage to $\mathbf{B}_{b\_prior}$ and $\mathbf{B}_{e\_prior}$ to eliminate the basis columns corresponding to insignificant coefficients, and denote the column-reduced bases as $\mathbf{B}_{b\_prior\_sub} \in \mathbb{R}^{m\times k_1}$ and $\mathbf{B}_{e\_prior\_sub} \in \mathbb{R}^{m\times k_2}$, where k_1 and k_2 are the number of columns in the new bases.

Once the bases have been learned from the prior data, we use them in estimating the coefficients of the BCG and EEG components of the contaminated data in the reconstruction stage. Even though the EEG measurements recorded inside and outside the MR environment may not be exactly equivalent[SBG05, DUS06], potentially affected by the posture, the magnetic and claustrophogenic MR scanner environment, it is reasonable to assume that

the brain originates consistent EEG recordings both inside and outside the scanner, and produces similar EEG characteristics such as the global power spectrum and certain local activation patterns. Therefore one may use the EEG bases from the prior data acquired outside the scanner to represent the EEG components acquired inside the scanner.

Additionally, despite the possibility that BCG artifacts may vary spatially, caused by movement of the electrodes, rotation of the head, or changes of influx from conductive surface blood flow, we have observed that BCG artifacts vary smoothly in small neighborhoods. This is particularly true with our high-density EEG cap of over 200 electrodes, as each channel has multiple physically connected and closely located adjacent channels. Therefore we propose to block neighboring channels without major vessels crossing to represent the BCG from an unblocked channel under examination. Moreover, as our experiment has blocked over 200 channels for demonstration-purposes, each unblocked channel is surrounded by multiple blocked channels providing abundant similar BCG-only signals.

3.3.5 Reconstruction

To best capture the strong temporal variations present in BCG artifacts, as illustrated in Fig.3.3, we impose an ℓ_2 penalty on the BCG coefficients to encourage the reconstruction to temporally resemble the prior BCG which is acquired synchronously with the contaminated data at a different blocked channel. With the learned basis vectors ($\mathbf{B}_{b\_prior\_sub}$ and $\mathbf{B}_{e\_prior\_sub}$), we reconstruct the signal components by seeking $\mathbf{C}_b$ and $\mathbf{C}_e$ to minimize

$$\begin{aligned}\min_{\mathbf{C}_b,\mathbf{C}_e} \|\mathbf{B}_{b\_prio\_subr}\mathbf{C}_b + \mathbf{B}_{e\_prior\_sub}\mathbf{C}_e - \mathbf{Y}\|_F^2 \\ + \sigma \|\mathbf{C}_{b\_prior} - \mathbf{C}_b\|_F^2 ,\end{aligned} \tag{3.3}$$

where σ is a regularization control parameter.. Subsequently, we recover the BCG and EEG components in the contaminated data $\mathbf{Y}$ with

$$\begin{aligned}\hat{\mathbf{X}}_b &= \mathbf{B}_{b\_prior\_sub}\mathbf{C}_b, \\ \hat{\mathbf{X}}_e &= \mathbf{B}_{e\_prior\_sub}\mathbf{C}_e.\end{aligned} \tag{3.4}$$

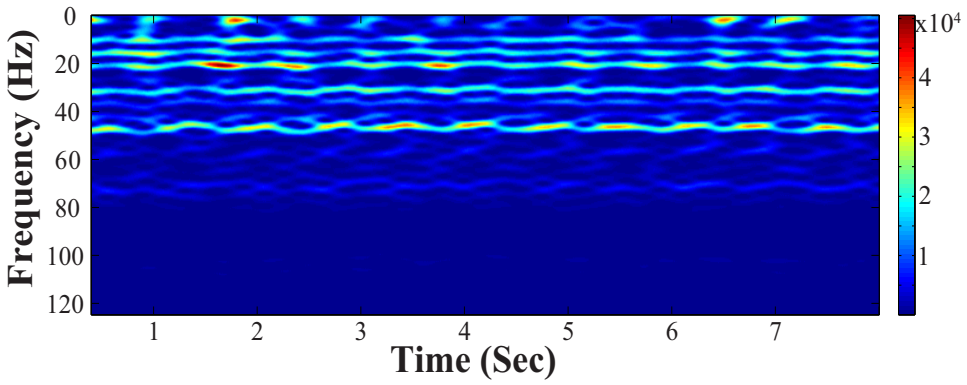

Figure 3.3: Power changes of BCG artifacts (from one channel) in time-frequency domain

3.4 Experimental Results and Discussion

To evaluate different artifact removal approaches quantitatively, and to provide parameter selection guidance when real contaminated data is used, we simulated contaminated EEG data from known BCG-only and EEG-only recordings according to the generative model introduced in Sect.3.3.1, to enable direct comparison between reconstructed and ground-truth component signals. First, we selected k_1 segments of EEG-only signals as ground-truth EEG (the red EEG recordings in Figure 3.4), denoted as $\tilde{\mathbf{X}}_e \in \mathbb{R}^{m \times k_1}$, which were acquired from one unblocked channel A outside the scanner in session I. Then, the ground-truth BCG-only signals, denoted as $\tilde{\mathbf{X}}_b \in \mathbb{R}^{m \times k_1}$, were chosen from the acquisition of channel A from inside the scanner in session II. Finally, the contaminated data, denoted as $\tilde{\mathbf{Y}} \in \mathbb{R}^{m \times k_1}$, was synthesized according to the generative model $\tilde{\mathbf{Y}} = \tilde{\mathbf{X}}_b + \tilde{\mathbf{X}}_e$. Figure 3.4 illustrates this process. Notice that the EEG-only signals $\tilde{\mathbf{X}}_{e\_prior}$ used as prior information were from either channel A or B (a neighboring channel to channel A) at a different time than the EEG data $\tilde{\mathbf{X}}_e$ we applied in simulating the contaminated data $\tilde{\mathbf{Y}}$, and BCG prior data $\tilde{\mathbf{X}}_{b\_prior}$ was collected at the same time as $\tilde{\mathbf{X}}_e$ and $\tilde{\mathbf{X}}_b$ but from a neighboring channel B.

In this section we show the strength of the proposed basis-learning and reconstruction framework. We start by comparing the jointly learned bases from our basis-learning step with that from the OBS method, using the experimentally acquired BCG-only and EEG-only data. To reduce the computation time, we downsampled the BCG/EEG-only data

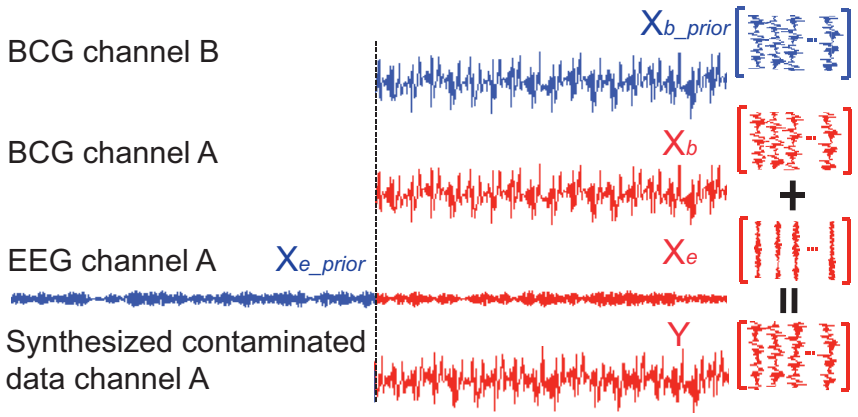

Figure 3.4: We use the BCG data from channel B (blue) as the prior BCG data denoted as $\tilde{\mathbf{X}}_{b\_prior}$ after alignment. The EEG data from channel A or B (blue) can be used as the prior EEG data $\tilde{\mathbf{X}}_{e\_prior}$. Simulated contaminated data ($\tilde{\mathbf{Y}}$) is summed from the BCG ($\tilde{\mathbf{X}}_b$) and EEG ($\tilde{\mathbf{X}}_e$) data (red) both from channel A.

from 250Hz to 50Hz with an anti-aliasing filter after the preprocessing process explained in Sect.3.3.3. Upon aligning recordings to the detected heartbeats, the resulting $m \times k$ dimension of a 13.6-minute recording from one channel was reformatted as a matrix $\mathbf{X}_{e\_prior}$ of size 73×856.

3.4.1 Performance Evaluation of Basis Learning

We chose columns belonging to the first 5.4 minutes recordings as prior data for generating the BCG/EEG-only basis matrices, with $\mathbf{X}_{b\_prior}$ and $\mathbf{X}_{e\_prior}$ of dimension 73×340. The columns of the basis matrices were normalized to have unit ℓ_2 norms.

We then applied our basis learning scheme onto the first 5.4 minutes of prior data. We stop the iteration as soon as the relative change $\left\|\mathbf{C}_e^{k+1} - \mathbf{C}_e^k\right\| / \left\|\mathbf{C}_e^k\right\|$ between two iterations is less than 10^{-6}. We chose the step length to be 1.618 according to [DYZ11]. The parameters of the basis learning function were tuned not for the best orthogonality between the bases but for the best recovery results of the EEG components in the next 8.2 minutes, as reconstruction module is simple with a signal parameter σ, and can be solved efficiently. The navigation of the parameter space was performed with 3 levels of grid density. On the first level, we aimed

to find the best orders for μ, β_1 and β_2 by sampling finely in the log-space of the directions of μ and ratios (β_1/μ) and (β_2/β_1). On the second and third level, we refined sampling on the linear space of μ, β_1 and β_2. We tuned λ by making it extremely small ($\lambda = 10^{-8}$) at first and then gradually increasing its value after the other three parameters are found.

Unlike the DRJIB method, where BCG and EEG basis vectors are retrieved from experimentally acquired BCG-only and EEG-only signals, the OBS method generates them from contaminated data, claiming that the first several sequential PCs describe the subspace of the BCG, and that removing the contribution of these PCs would remove the BCG artifacts. This rationale implicitly assumes that the BCG and EEG subspaces do not overlap and furthermore are orthogonal, as the PCs are orthonormal basis vectors. Without ground-truth BCG/EEG-only signals, there is no good way to test the feasibility of assumptions and one may need to accept the results as they are, in the absence of better alternatives. However our new experimental setup in Sect.3.3.2 provides observations of BCG/EEG-only signals, and offers an opportunity to examine the validity of those assumptions for further improvement of the signal separation results. To this end, we assessed the degree of orthogonality presented in the BCG and EEG subspaces. Basis vectors directly derived from each subspace were obtained by applying PCA to the BCG-only and EEG-only data respectively. We then calculated the non-orthogonal index, defined as $\eta = \|\mathbf{B}_{bcg}^T \times \mathbf{B}_{eeg}\|_F / \|I\|_F$ where $\mathbf{B}_{bcg}$, $\mathbf{B}_{eeg}$ and $I \in \mathbb{R}^{m \times m}$, between the principal component matrices $\mathbf{B}_{bcg}$, $\mathbf{B}_{eeg}$. We then evaluated this index for different choice of included PCs. As we sequentially include less significant PCs, shown in Fig.3.5, the orthogonal index starts from 0.1487 rather 0, suggesting that the BCG and EEG subspaces are *not* orthogonal even if represented with a single basis vector.

We further compared the feasibility of the bases from both the DRJIB and the OBS methods by calculating the relative errors by projecting the demeaned ground-truth BCG/EEG-only data onto the basis vectors. For the DRJIB method, the prior basis vectors were obtained with the parameters of our basis learning step to be $\mu = 5.05 \times 10^4$, $\beta_1 = 5.05 \times 10^8$, $\beta_2 = 5.05 \times 10^6$ and $\lambda = 10^{-8}$. Figure. 3.6(a)–(b) presents the relative error changes as the number of the columns of the BCG and EEG bases was reduced. For the OBS method, we obtained the bases (PCs) from the contaminated data and generated the residual energy

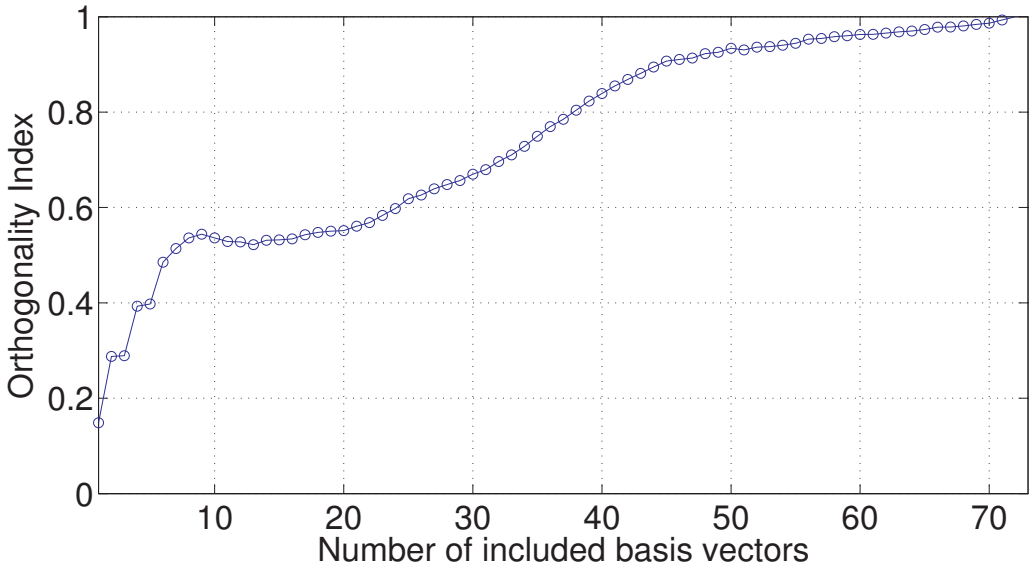

Figure 3.5: Orthogonal Index

changes shown in Fig. 3.6(c)–(d) as we varied the number of PCs considered to be the BCG basis while the remaining PCs was considered to be the EEG basis.

The OBS bases leave as much as 43.09% error in representing the BCG-only data, and 100% for the EEG-only signals when the curves of relative errors achieve minimum (when all 72 PCs are used for BCG basis and the remaining 1 PC as EEG basis). For default parameter (3 PCs for BCG basis and the rest 70 PCs for EEG basis), there is 69.71% and 161.8% error in representing BCG-only and EEG-only data.

It is not surprising that the bases derived from contaminated data result in large residuals due to the model mismatch from the nebulous assumption of orthogonal subspace relationship. By contrast, our jointly learned bases leave only $5.71 \times 10^{-14}\%$ and $1.36 \times 10^{-12}\%$ error for the BCG and EEG signals without column reduction, demonstrating the significant benefit of deriving bases from pure signals.

We also performed explicit column reduction to the learned bases $\mathbf{B}_{b\_prior}$ and $\mathbf{B}_{e\_prior}$ to reflect $\ell_{2,1}$ promoted sparse entries of $\mathbf{C}_{b\_prior}$ and $\mathbf{C}_{e\_prior}$. As achieving best recovery results was the goal in basis-learning step, the reconstruction procedure was performed at each iteration with varying number of basis columns. Applying column reduction at each iteration incurs additional computational cost. However, as the BCG prior coefficient $\mathbf{C}_{b\_prior}$

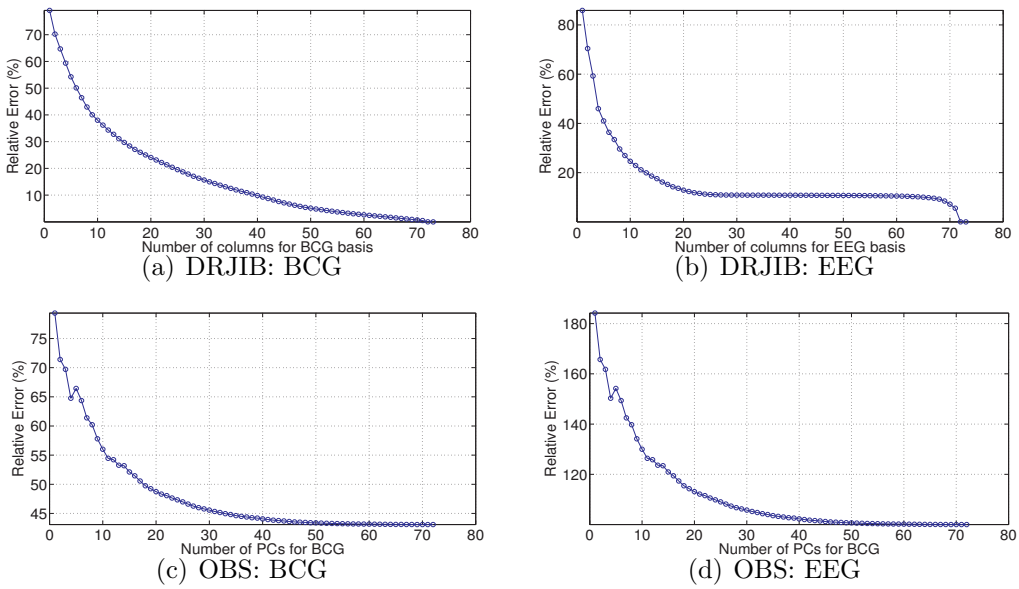

(a) DRJIB: BCG (b) DRJIB: EEG

(c) OBS: BCG (d) OBS: EEG

Figure 3.6: Relative errors from representing the demeaned BCG and EEG signals using different number of PCs.

is intrinsically dense and the dimension changes for the EEG prior coefficient are within a narrow range, column reduction only needs to be performed for a few number of iterations during updates of the basis vectors.

3.4.2 Performance Evaluation of Reconstruction

To evaluate the signal separation performance of the DRJIB, the OBS method was also performed for comparison. We measure their recovery performances in terms of relative error RE, defined as $RE = \|\hat{\mathbf{X}} - \mathbf{X}_{truth}\|_F / \|\mathbf{X}_{truth}\|_F$. Recovered BCG/EEG signals and their corresponding groundtruth are represented with $\hat{\mathbf{X}}$ and $\mathbf{X}_{truth}$ respectively. The $\hat{\mathbf{X}} \in \mathbb{R}^{m \times k}$ represent recovered BCG/EEG signals and $\mathbf{X}_{truth} \in \mathbb{R}^{m \times k}$ denotes the ground-truth BCG/EEG data. Both methods were conducted without further residual artifact removal techniques [NBI05], and applied to the 5.3-minute contaminated data synthesized from the BCG/EEG-only data that were acquired at different time than the recordings used for basis learning phase (the first 3.4-minute).

The prior BCG and EEG bases used in the reconstruction phase have the size of 73×73

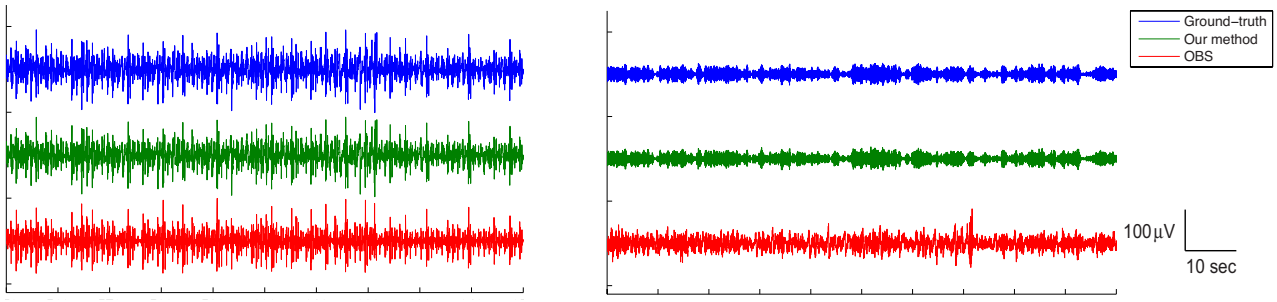

(a) BCG

(b) EEG

Figure 3.7: Comparison of the reconstruction results from DRPE and OBS. (a) and (b) display information regarding BCG and EEG signals, respectively. The top row of both (a) and (b) presents ground-truth BCG and EEG signals used in simulation. The middle row shows the reconstructed BCG and EEG signals from the DRJIB method, which is compared to the reconstructed signals from the OBS method shown in the bottom row. DRPE method yields only 6.414% and 15.80% relative errors for the BCG and EEG reconstruction, while the OBS generates 47.5% and 117.5% relative errors for BCG and EEG.

and 73×72 dimensions respectively after column reduction. In our reconstruction process we used a penalty parameter $\sigma = 1.06$. For the OBS method, we chose the default number 3 as the number of primary principle components for the BCG reconstruction. Thus, the remaining 70 PCs from the contaminated data were implied to be the EEG basis.

To save space, Fig.3.7 shows only a small portion of the reconstructed results from two methods alongside the ground-truth data. It can be observed from Fig.3.7, the BCG and EEG components are better separated and preserved by the DRJIB method than the OBS method and reduced the relative errors for EEG components by approximately 7.5-fold. Furthermore, Fig.3.7 shows that the DRJIB successfully recovers the qualitative temporal behavior of the EEG signals thanks to its use of the basis from the prior and group sparsity structures for the coefficients, whereas the OBS method distorts the temporal behaviors. The benefits of modeling each signal type specifically rather than as a whole appear to have alleviated the potential influence of basis inconsistency from different acquisition environments and different channel locations.

Table 3.1: Cross validation results from 3 groups: Relative Errors (RE) in percentage. Each group has a different segment as validation set with the remaining two segments (2) as training set.

	DRJIB				OBS			
	BCG Segments		EEG Segments		BCG Segments		EEG Segments	
RE(%)	Training	Validation	Training	Validation	Training	Validation	Training	Validation
Group 1	6.41	6.58	15.64	16.24	52.31	61.50	130.5	153.5
Group 2	6.45	6.48	15.78	16.21	52.47	61.54	129.9	150.6
Group 3	6.52	6.80	16.16	16.90	51.97	61.02	128.0	150.5

We also employed a standard 3-fold cross-validation [FHT01] to quantify the overfitting and the consistency of our DRJIB method and that of the OBS. Let $Y^{(1)}$ denote a 73×158 (2.5-minute) matrix containing a randomly selected subset of column vectors from synthesized contaminated matrix $\mathbf{Y}$(8.2-minute). And let $\bar{\mathbf{Y}}^{(1)}$ be a 73×356 matrix (5.7-minute) containing the complimentary set of data vectors that will be used for training. We then applied the DRJIB and the OBS to recover BCG and EEG components from the $\bar{\mathbf{Y}}^{(1)}$. The parameter σ of the DRJIB was tuned to aim for the best recovery of the EEG components. The parameter of the OBS is the number of PCs (N_{pc}) used to represent BCG artifacts. We chose $N_{pc} = 3$. Once the optimal parameters were determined for the training dataset $\bar{\mathbf{Y}}^{(1)}$, they were used as parameters for recovering the BCG/EEG signals from the validation dataset $\mathbf{Y}^{(1)}$. The process is then repeated using $t = 3$ non-intersecting subsets of the data to yield the reconstruction errors of the training and validation for each subset. The relative errors of the cross-validation process are listed in Tabel.3.1. All reconstruction parameters in Tabel.3.1 are the same ($\sigma = 1.1$) and result in similar good reconstruction results for all the training sets, with only slightly worse results for the validation sets. This strongly suggests that the DRJIB method is consistent with essentially negligible overfitting.

Furthermore, Fig.3.6(c)–(d) reveals the changes of the relative errors evaluated on various

testing sets as the number of PCs for the BCG is varied. Consistent to all testing sets, we observe that the lower bound for the EEG data recovery is actually 100%, indicating that the reconstruction, via projection onto PCs based on the OBS method, fails to recover EEG useful signal information. These significant reconstruction errors are introduced primarily by model mismatch and may result in false interpretations to the continuous EEG studies inside the scanner. This 100% lower bound may be explained by the large difference in energy between the BCG artifacts and the normal EEG signals, as the BCG energy appears to completely dominate PCA results from the contaminated signals.

3.5 Conclusions and Future Works

A framework for separating the BCG artifacts from the brain EEG signals in noisy EEG measurements was introduced in this paper. The basic idea is to first jointly learn a pair of BCG and EEG bases that optimally represent the BCG and EEG components in terms of signal separation, then separate the two components of the contaminated signals with the learned bases and regularizations. Toward this goal, we introduced a new experimental setup that acquires BCG/EEG-only signals. We have investigated and developed a basis learning procedure based on group sparse representations for the BCG and EEG signals and a new term that promotes incoherence between the bases, yet still allows subspace intersection. Furthermore, a specific column reduction of the learned bases is performed and the ℓ_2-norm regularization on the BCG coefficients is introduced to preserve the non-stationary temporal variations of the BCG signals. The experimental results demonstrate that our DRJIB method surpasses the OBS method whose assumption is shown to be questionable. Finally, the cross-validation results show minimal overfitting of our proposed scheme. In future work, we will focus on: 1) extending the framework to incorporate the BCG spatial variations and 2) implementing the proposed method for on-line artifact removal.

CHAPTER 4

Removing ballistocardiogram (BCG) artifact from full-scalp EEG acquired inside the MR scanner with Orthogonal Matching Pursuit (OMP)

4.1 Abstract

Ballistocardiogram (BCG) artifact remains a major challenge that renders electroencephalographic (EEG) signals hard to interpret in simultaneous EEG and functional MRI (fMRI) data acquisition. Here, we propose an integrated learning and inference approach that takes advantage of a commercial high-density EEG cap, to estimate the BCG contribution in noisy EEG recordings from inside the MR scanner. To estimate reliably the full-scalp BCG artifacts, a near-optimal subset (20 out of 256) of channels first was identified using a modified recording setup. In subsequent recordings inside the MR scanner, BCG-only signal from this subset of channels was used to generate continuous estimates of the full-scalp BCG artifacts via inference, from which the intended EEG signal was recovered. The reconstruction of the EEG was performed with both a direct subtraction and an optimization scheme. We evaluated the performance on both synthetic and real contaminated recordings, and compared it to the benchmark Optimal Basis Set (OBS) method. In the challenging non-event-related-potential (non-ERP) EEG studies, our reconstruction can yield more than fourteen-fold improvement in reducing the normalized RMS error of EEG signals, compared to OBS.

4.2 Introduction

Simultaneous electroencephalography and functional magnetic resonance imaging acquisition offers a promising probe to study different, yet connected, bioelectric and hemodynamic attributes of brain activity with complementary temporal and spatial resolutions. This non-invasive neuroimaging technique has applications in the analysis of event-related brain responses [BSG07, DUS06, ESM05], studies of ongoing brain rhythms and networks [GSE02, LKS03], and studies of epileptic activity [BAW03, KML01, LSJ01]. Despite many successful applications, ballistocardiogram (BCG) artifact in concurrent EEG-fMRI acquisition still presents a challenge in continuous recoding (e.g., non-ERP) studies especially when the magnetic field strength is high. BCG presents high temporal non-stationarity due to variation in cardiac cycles [BPJ02, DSS07], and its amplitude scales with magnetic field strength [YMG10, MHB13].

Previous attempts to suppress the BCG artifacts have focused primarily on channel-wise denoising, with major developments in template-subtraction, principal component analysis (PCA)-based methods [AJT00, ELS04, GSE00, NBI05] and independent component analysis (ICA)-based methods [GNM10, LZG12, SCL05], as reviewed in [GVK07, VDR10]. The widely used Optimal Basis Sets method (OBS) [NBI05] is a PCA-based approach that regresses out the mean effects and its first few principal components from the contaminated data on a heartbeat-by-heartbeat basis. Attempts to incorporate spatial information have also been made with spatial PCA and ICA by [BAW03, SCL05]. However these PCA/ICA-based approaches are based on strong orthogonality/independence assumptions and subject to manual selection of number of components to be included.

Another focus on BCG suppression is based on reference signals, generated by motion sensors [BPJ02] or wire loops [MAF07], for the artifact itself. More recent developments, such as [CMG14, MHB13, XRC13a] and the fEEG^{TM} system from (Kappametrics Inc., Chantilly, USA), apply an insulating layer to directly acquire BCG-only artifact signals from channels that are electrically isolated from the scalp. Although the measured artifact reference signals are not identical to the BCG [MHB13], significant suppression has been achieved by reference

layer artifact subtraction (RLAS) [CMG14]. However, RLAS and fEEG$^{\text{TM}}$ require purpose-built hardware and exploit no further denoising steps than a simple subtraction.

We propose a method to remove BCG from the uninsulated channels using inferential relationship amongst whole-scalp BCG signals, which provides an additional denoising benefit yet requires no hardware modification. As the BCG artifacts [YMG10, MHB13] are related to the movements of conductive liquid such as surface blood flow, or movements from electrodes caused by pulsation of blood vessels or head motion, we expect similar BCG temporal behaviors from adjacent channels. In our previous study [XRC14b], we proposed surrounding each uninsulated channel with a neighborhood of shielded channels that provide BCG-only signals, to ensure access to at least one proper prior. This approach, though performs well, is limited by its ad hoc neighboring channel selection and the potential requirement of a large number of insulated channels. Therefore, a sparse, and stable, insulation pattern is highly desirable in contrast to local probing in order to explore brain activity patterns.

We aim here to balance two conflicting goals: (1) minimize the number of insulated channels; and (2) denoise the EEG signals in the uninsulated channels with high accuracy. In an optimization framework, we jointly seek the optimal subset of a small cardinality to insulate, and an inference model to estimate the BCG components for the other uninsulated channels based on the BCG readings from the insulated set. We propose here a simple greedy scheme based on orthogonal matching pursuit (OMP), and report its performance in comparison with both the benchmark OBS method and inference with two alternative *ad hoc* insulation patterns.

4.3 Generative Model for Contaminated EEG Data

As BCG and EEG are believed to originate from independent sources, they should add linearly with minimal interaction and subject to noise contamination. Mathematically,

$$\mathbf{Y}=\mathbf{X}_{bcg}+\mathbf{X}_{eeg}+\varepsilon, \tag{4.1}$$

where $\mathbf{X}_{bcg}$, $\mathbf{X}_{eeg}$ and $\varepsilon \in \mathbb{R}^{C\times T}$ represent BCG artifacts, underlying uncontaminated EEG signals, and noise respectively. C and T are the number of channels and the number of time points of the recordings, respectively. This model does not presume any statistical relationship between BCG and EEG: independence of the noise sources is in the sense of physics and physiology, rather than statistics. This model has been applied implicitly in many previous studies and simulation studies [AJT00, GSE00, GVK07, NBI05, VDR10].

4.4 Experimental Setup

Three healthy right-handed adult volunteers, (2 male and 1 female, with age between 24 and 28 yrs), gave informed consent for participation in this study according to the guidelines of the UCLA medical investigational review board. For our experiments, we used a 3T Siemens Tim Trio scanner (Siemens Medical Solutions, Erlangen, Germany). We acquired EEG data with a GES300MR system (Electrical Geodesics, Inc., Eugene OR). This 256-channel apparatus made contact with the scalp via KCL-filled sponge contacts mounted in plastic pedestals with a contact-impedance of 20kΩ or less. EEG data were sampled at 250Hz and amplifier gains were kept constant. To focus on only BCG artifacts, no MRI scanning took place during the acquisitions inside the scanner. The overall protocol is kept consistent for recording spontaneous EEG as well as eyes open/close EEG activity (see more experimental setup details in [XRC14b]).

4.4.1 Acquisition of BCG-only data:

Two layers of material were inserted between the scalp and the electrodes to collect BCG-only data while electrically blocking conductance of EEG brain signals.

(1) Insulating Layer: To collect BCG-only artifacts, we first isolated electrodes from the scalp with a plastic insulating barrier to block brain signals from conduction, as shown in Figure 4.1(A).

(2) Semi-conducting Layer: To collect properly signals from insulated electrodes, a semi-conductive layer was then inserted between the insulating layer and the electrodes. For this

we used a thin piece of paper, dampened with saline (Figure 4.1(B)), as the semi-conductive layer, which provided the proper impedance while avoiding short circuits or alteration of BCG signals.

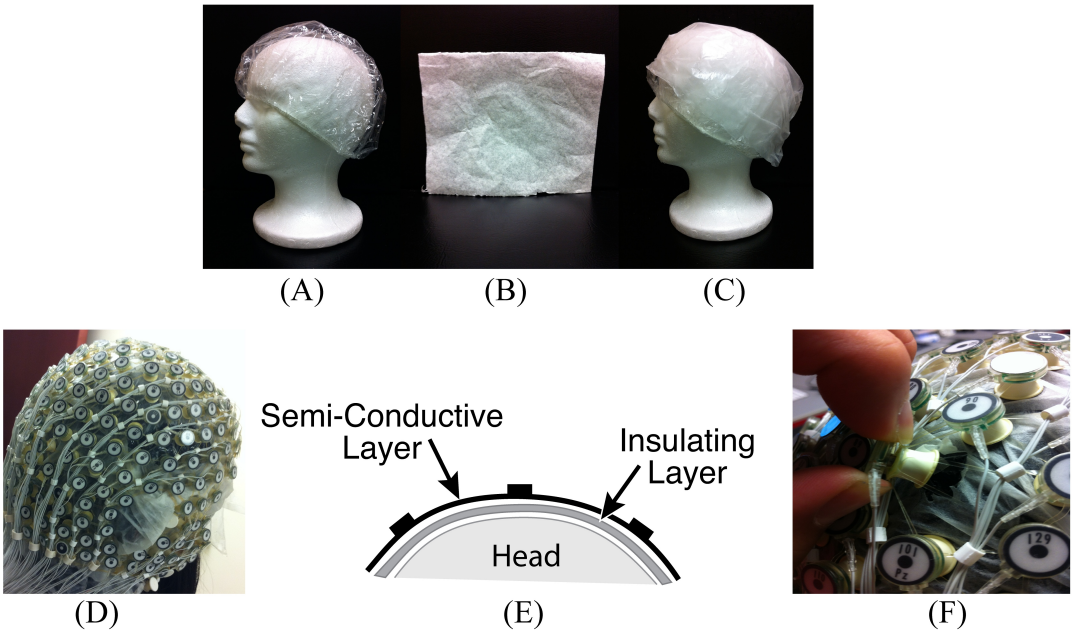

Figure 4.1: (A) Insulation layer: a shower cap (B) Semi-conducting layer: paper layer (C) A piece of thin paper dampened with saline placed on top of the insulation layer (D) A picture with all channels blocked (E) Sandwich diagram of construction (F) Unblocking one channel.

4.4.2 Acquisition of Contaminated EEG and BCG-only data :

Inside the scanner, we acquired contaminated and BCG-only data at the same time, but from different channels. After inserting two layers for acquiring BCG-only signals, we recorded simultaneously contaminated EEG data from selected channels by removing the insulation and paper layers underneath, as shown in Figure 4.1(F). We chose to unblock 20 conventional channels, approximating the standard 10-20 systems. In practice, and as discussed below, one can determine which channels to block in advance, and use setup in Figure 4.1(F) to maximize the number of channels that collect EEG signals. The measured impedance before and after unblocking and their difference are provided in the Supplementary Material. On average, the impedance differed by 100Ω for electrodes in the blocked, and unblocked, conditions.

4.5 General Inference Logic and Work Flow

BCG signals, which are linked to pulsation and other motion effects [MHB13, NBI05], exhibit high temporal non-stationarity, making direct temporal modeling extremely difficult with classic parametric/nonparametric approaches. Despite this, we expect the correlations of the BCG traces across multiple channels to be approximately consistent, as illustrated in Figure 4.2. We hypothesize that the full-scalp BCG-only signals can be of intrinsically low dimension along the spatial direction when signals acquired from multiple locations contain redundant/correlated information; this is supported by the observation (see the Supplementary Material) that just four principal components (PCs) explain more than 95% total energy after applying spatial PCA to the full-scalp BCG-only signals, $\mathbf{X}_{bcg} \in \mathbb{R}^{C\times T}$. A similar observation was made also in [BAW03] via visual inspection. These preliminary analyses allude to the possibility of inferring the full-scalp BCG artifacts from BCG signals collected from a subset of channels.

In the equations below, we adopt several MATLAB (the Mathworks, Natick, MA) notations for their compactness and clarity. For any subset $\Lambda \subseteq \{1, 2, ..., C\}$ and matrix $\mathbf{X} \in \mathbb{R}^{C\times T}$, $\mathbf{X}[\Lambda, :]$ denotes a submatrix of $\mathbf{X}$ consisting of rows $\mathbf{X}_i$ for $i \in \Lambda$. The cardinality of the set Λ is denoted by $|\Lambda|$. In this paper, we describe a set of full-scalp channels as Λ_{full} ($|\Lambda_{full}| = C$), the subset of insulated channels as Λ_{ins}, and the complementary set of non-insulated channels as $\Lambda_{nins} = \Lambda_{full}\backslash\Lambda_{ins}$. The linear inference seeks a relation with

$$\mathbf{X}_{bcg}[\Lambda_{nins}, :] = \mathbf{W}\mathbf{X}_{bcg}[\Lambda_{ins}, :] + \text{noise}, \tag{4.2}$$

where $\mathbf{W}$ is of dimension $|\Lambda_{nins}| \times |\Lambda_{ins}|$. We propose a two-stage procedure to estimate the full-scalp BCG artifacts with BCG-only signals from a subset of insulated channels, based on the assumption that the spatial correlation of full-scalp BCG is relatively consistent. See Section 4.5.4 and 4.6.2.1 for greater detail.

In the first stage for model building, all channels are insulated to collect full-scalp BCG-only signals, $\mathbf{X}_{bcg}$, which are used to estimate an inference matrix $\mathbf{W}$ and select a subset Λ_{ins} via Equation 4.2. In the second stage for acquisition, the channels in Λ_{ins} remain insulated to acquire BCG-only signals $\mathbf{X}_{bcg}[\Lambda_{ins}, :]$ while the remainder of the channels Λ_{nins}

collects normal contaminated EEG recordings $\mathbf{Y}[\Lambda_{nins}, :]$ in which the BCG contributions are estimated subsequently via Equation 4.2 with the inference, $\mathbf{W}$, from the model-building stage.

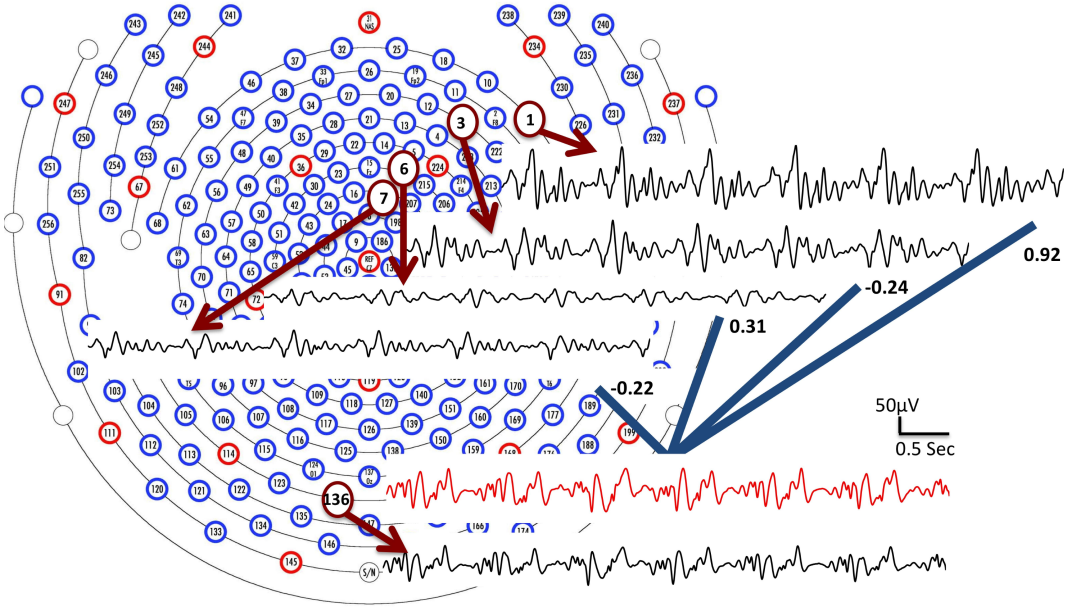

Figure 4.2: BCG traces from four channels (1, 3, 6 and 7) are combined linearly with weights to form an estimate of the BCG trace from channel 136 (shown in red). The collected BCG signals (channel 1, 3, 6, 7 and 136) are shown in black.

4.5.1 Stage I: Model Building

It is desirable to use a small number of channels for BCG estimations, so that the proposed approach can be applied to a wide range of EEG caps and preserve the value of high-density EEG recordings. We choose a "budget" size (the cardinality of insulation set $|\Lambda_{ins}|$) to be 20 by cross validation, as reported in Section 4.6.2.2. The goal of selecting the optimal subset of electrodes with the best inference performance can be formulated into a minimization-minimization problem:

$$\min_{\Lambda_{ins}} \{ \min_{\mathbf{W}(\Lambda_{ins})} \|\mathbf{X}_{bcg}[\Lambda_{nins}, :] - \mathbf{W}\mathbf{X}_{bcg}[\Lambda_{ins}, :]\|_F^2 \}, \tag{4.3}$$

where $\|\|\|_F$ denotes Frobenius norm and we use $\mathbf{W}(\Lambda_{ins})$to explicitly indicate the dependence of the optimal $\mathbf{W}$ on the subset Λ_{ins}. By introducing an identity map on the insulated portion and reformulation with an expanded inference matrix $\widetilde{\mathbf{W}} = [\mathbf{I}; \mathbf{W}]$, it can be shown that optimizing Equation 4.3 is equivalent to solving

$$\min_{\Lambda_{ins}} \{\min_{\widetilde{\mathbf{W}}} \left\| \mathbf{X}_{bcg}[\Lambda_{full}, :] - \widetilde{\mathbf{W}} \mathbf{X}_{bcg}[\Lambda_{ins}, :] \right\|_F^2 \}, \tag{4.4}$$

which has a regression goal independent of the insulation set Λ_{ins}. The inner problem of solving for $\widetilde{\mathbf{W}}$ given Λ_{ins} is an ℓ_2 problem with a closed-form solution, but the outer set selection problem is NP-hard. For practical purposes, we adopt a greedy Orthogonal Matching Pursuit (OMP) approach [TG07] for the set selection problem. At each step the subset Λ_{ins} is expanded by one channel that maximizes the inner product of the signal from the selected channel and the residual signals not yet explained by the already selected channels. The inference matrix, $\widetilde{\mathbf{W}}$, is updated at each step with an updated subset Λ_{ins}.

The OMP procedure is as follows:

- Step 1: Initialize the insulating subset as empty ${\Lambda^{(0)}}_{ins} = \{\}$, the inference matrix $\widetilde{\mathbf{W}}^{(0)} = \mathbf{0}$, and the residual signals $\mathbf{R}^{(0)} = \mathbf{X}_{bcg}[\Lambda_{full}, :]$. Then, initialize the full-scalp BCG-only signals to be $\mathbf{X} = \mathbf{X}_{bcg}[\Lambda_{full}, :]$, and set the iteration counter $k = 1$.

- Step 2: Find a channel that solves the maximization problem:

$$i = \arg\max_i \sum_{j \in \Lambda_{full}} \left\langle {\mathbf{R}^{(k-1)}}_j \quad , \frac{\mathbf{X}_i}{\|\mathbf{X}_i\|_F} \right\rangle^2.$$

- Step 3: With this selection, update everything as follows:

$${\Lambda^{(k)}}_{ins} = {\Lambda^{(k-1)}}_{ins} \quad \bigcup \{i\};$$
$$\widetilde{\mathbf{W}}^{(k)} = \arg\min_{\widetilde{\mathbf{W}}} \left\| \mathbf{X}_{bcg}[\Lambda_{full}, :] - \widetilde{\mathbf{W}} \mathbf{X}_{bcg}[{\Lambda^{(k)}}_{ins}, :] \right\|_F^2;$$
$$\mathbf{R}^{(k)} = \mathbf{X}_{bcg}[\Lambda_{full}, :] - \widetilde{\mathbf{W}}^{(k)} \mathbf{X}_{bcg}[{\Lambda_{ins}}^{(k)}, :];$$
$$k = k + 1.$$

Go back to step 2 until the budget number of insulated channels has been reached.

- Step 4: Store the final set $\Lambda_{ins} = \Lambda^{(k)}{}_{ins}$ and the inference matrix $\widetilde{\mathbf{W}} = \widetilde{\mathbf{W}}^{(k)}$.

After obtaining the inference matrix $\widetilde{\mathbf{W}}$ and insulation subset Λ_{ins} from the full-scalp BCG-only signals, the estimated BCG components $\widehat{\mathbf{X}}_{bcg}[\Lambda_{nins}, :]$ in the contaminated EEG recordings are reconstructed according to Equation 4.2 using simultaneously collected BCG-only signals $\mathbf{X}_{bcg}[\Lambda_{ins}, :]$ by the following solution:

$$\widehat{\mathbf{X}}_{bcg}[\Lambda_{nins}, :] = \mathbf{W}\mathbf{X}_{bcg}[\Lambda_{ins}, :]. \tag{4.5}$$

As an alternative to automatic set selection methods, we devised two *ad hoc* patterns: a "lines" pattern with 4 groups of 5 channels, as shown in Figure 4.3(A); and a "patches" pattern containing 4 groups of 5 channels arranged in circles, as shown in Figure 4.3(B). In addition, the selected pattern from OMP is presented in Figure 4.3(C).

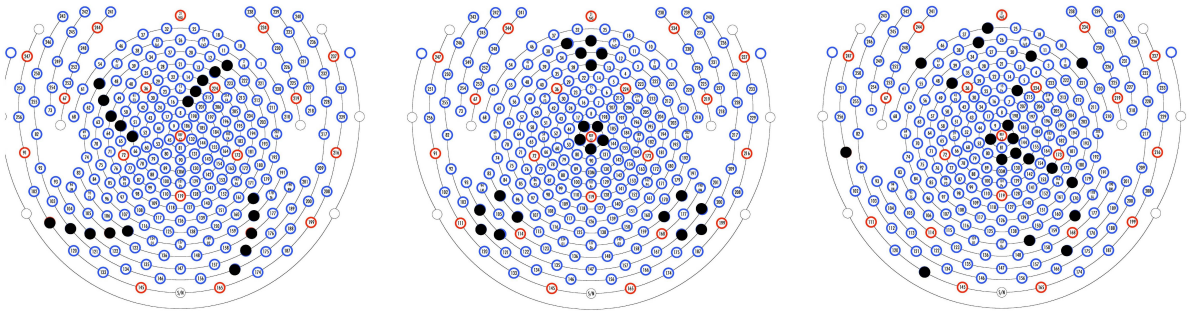

Figure 4.3: Three patterns for insulating channels (solid black dots): (A) the Lines pattern, (B) the Patches pattern, and (C) a pattern selected by OMP.

4.5.2 Stage II: Reconstruction of clean EEG

Here, we investigate two methods for reconstruction: direct subtraction approach, and optimization-based. (1) Direct subtraction: A straightforward and assumption-free method for denoising EEG is to subtract the estimated BCG components directly from the recorded noisy data $\mathbf{Y}$:

$$\widehat{\mathbf{X}}_{eeg}[\Lambda_{nins}, :] = \mathbf{Y}[\Lambda_{nins}, :] - \widehat{\mathbf{X}}_{bcg}[\Lambda_{nins}, :]. \tag{4.6}$$

(2) Optimization-based reconstruction: To further separate EEG from BCG, we incorporate an optimization-based scheme for temporally-concatenated segments that utilizes prior information from the EEG acquired outside the scanner. Based on patterns observed from BCG-only and EEG-only data, we devised a regularized optimization framework to separate the signals using group sparsity technique developed in compressive sensing [DYZ11]. The detailed explanation is provided in our previous work [XRC14b]. Mathematically, we impose a group sparsity penalty with $\ell_{2,1}$ norm, $\|\mathbf{C}_{eeg}\|_{2,1} \stackrel{def}{=} \sum_{i=1}^{m} \|\mathbf{C}_{eeg}[\,i,:\,]\|_2$, on the reconstructed EEG coefficient $\mathbf{C}_{eeg}$, where $i \in \{1, ..., m\}$ is an index set indicating the i^{th} group (row), and m is the number of rows in $\mathbf{C}_{eeg}$. In addition, the energy function adopts the EEG basis $\mathbf{B}_{e\_prior}$ learned from the out-of-scanner experiment. Therefore, one may reconstruct the EEG signals by estimating the EEG coefficients, $\mathbf{C}_{eeg}$, corresponding to the learned basis, $\mathbf{B}_{e\_prior}$ for each uninsulated channel by minimizing:

$$\min_{\mathbf{C}_{eeg}} \|\mathbf{C}_{eeg}\|_{2,1} + \frac{1}{2}\mu\|\mathbf{Y}_{eeg} - \mathbf{B}_{e\_prior}\mathbf{C}_{eeg}\|_F^2, \tag{4.7}$$

where the first term regularizes the group sparsity structure of the coefficients, and the second term imposes data fidelity. The scalar parameter, μ, balances the contribution of these two terms. $\mathbf{Y}_{eeg}$ is derived by subtracting the estimated BCG from recorded noisy data from one channel. The EEG component of the uninsulated channel is recovered by multiplying the prior basis with the estimated coefficients.

4.5.3 Construction of Synthetic contaminated EEG data

To compare the EEG reconstruction performance quantitatively among different artifact removal methods, we simulate contaminated EEG data by combining 12 minutes of BCG-only, and EEG signals (Equation 4.1) (see more details in [XRC13a]). This provides us with access to ground-truth that is absent in normal EEG-fMRI acquisitions. We use "clean" EEG signals collected from outside the scanner. Our simulation differs from the published works [GNM10, GVK07, VDR10], in that we use the true BCG signals to synthesize the contaminated data. The inference models used in the comparison include two *ad hoc* patterns, "lines" and "patches", and the pattern from the OMP approach. We compare the

performance among three methods: Channel-wise OBS (EEGLAB plug-in FMRIB version 1.2 [NBI05] with 3 principal components), inference + direct subtraction, and inference + optimization.

4.5.4 Consistency of the Inference Relationship

Our method assumes substantial consistency of the inference relationship over time, which reflects the temporal consistency of BCG spatial correlations among multiple channels. Once an inference matrix is sufficient in estimating one BCG segment, it is assumed to be adequate in recovering other segments that are distant in time. We perform a validation test with a 13-minute full-scalp BCG-only recordings in Section 4.6.2.1.

A second assumption of our methods is of nominal consistency of the inference relationship across experimental sessions. Between stage I and II sessions, subjects are removed from the scanner, and their caps are replaced. As a result of the physical movements, artifacts may differ substantially due to variations of scalp-electrode impedances and channel locations. Two kinds of inconsistencies may occur regarding our inference model. First, the channels selected from the first session may not suffice to represent BCG from another. Second, even if the selected channels remain representative, the inference matrix from the first session may not carry the proper weights to reconstruct the BCG from the second.

To verify the representativeness of selected channels, the subset selected from one training session is used to recover BCG from a testing session with an optimal inference matrix calculated from also the testing session, minimizing the contribution of the inconsistent inference matrix. After demonstrating the representativeness of selected channels, we proceed to examine the impact of physical movements on inference matrix. The inference matrix learned from the training session is applied to recover BCG from other testing sessions. The mean reconstruction errors of the two inconsistency tests are presented in Table 4.2 and 4.3.

In addition, we propose an inference matrix recalculation method to be used in the event that the inference matrix varies too much to recover adequate BCG. Our method divides time series signals for each channel into segments according to a fixed number of heartbeats, then

computes the averages of the segments for each channel. As noted by others [NBI05, AJT00], it is safe to assume that such ECG-synced averages contains negligible EEG after applying a 1-Hz high-pass filter to remove slow drifts in EEG, and only averaged BCG segments. As a result, we can obtain a new inference matrix from the BCG-only segments of all channels, and recover BCG following the same steps as Section 4.5. This amendment operates on the temporal domain of full-scalp BCG signals with negligible alteration of the BCG spatial relationships among channels. The BCG reconstruction errors from the new matrix are theoretically (see the Supplementary Material) and experimentally (Section 4.6.2.1) proven to be small. Furthermore, we applied the consistency tests not only on 5-minute BCG-only recordings from different experimental sessions from one subject, but also on 9-minute BCG-only recordings from three subjects. The results are shown in Section 4.6.2.1.

4.6 Results

When ground truth $\mathbf{X}_i$ is available, we define the normalized root mean squared error $nRMSE_i = ||\mathbf{X}_i - \widehat{\mathbf{X}}_i||_2 / ||\mathbf{X}_i||_2$ for the channel index i to quantify the performance of either BCG or EEG estimation $\widehat{\mathbf{X}}_i$. This channel-wise error can be displayed as a topographic map, showing the accuracy of estimations in the spatial domain across multiple channels. In addition, the spatial collective average over a set Λ is denoted by $ave\ nRMSE = \frac{1}{|\Lambda|} \sum_{i \in \Lambda} nRMSE_i$.

4.6.1 Performance Evaluation on EEG Reconstruction

4.6.1.1 EEG Reconstruction Results from Synthesized Data

For the purpose of evaluating the overfitting and consistency of our proposed framework, the 12-minute long synthesized data were partitioned further into three equal size datasets for cross-validation, in which parameters were selected by a grid-search over parameter space from training datasets and tested on the validation datasets. The topographic maps of $nRMSE$ averaged from the validation datasets are reported in Figure 4.4 with their collective averages $ave\ nRMSE$ in the brackets. Our methods show improvements not only in a few

selected channels but across the topology of the scalp. In addition, the temporal and spectral plots of ground-truth and reconstructed BCG and EEG signals appear in Figure 4.5 and Figure 4.6.

As shown in Figure 4.4, the best result, obtained by combining OMP approach with the optimization-based reconstruction, offers approximately 14.6-fold improvement compared to OBS in full-scalp EEG reconstruction. In comparison, our previous results using neighboring channel as BCG prior reported only 7 fold improvement. Even the simple direct subtraction with two *ad hoc* patterns can improve the EEG reconstruction quality by 10 to 12-fold. We interpret the overall reduced energy in the spectrum and spectrogram of reconstructed data in Figure 4.6(B) and Figure 4.7 as a reflection of the artifact contribution. All spectrograms were produced with 0.1Hz frequency resolution, a Hamming window of length 256 and the number of points that each segment overlaps being 200.

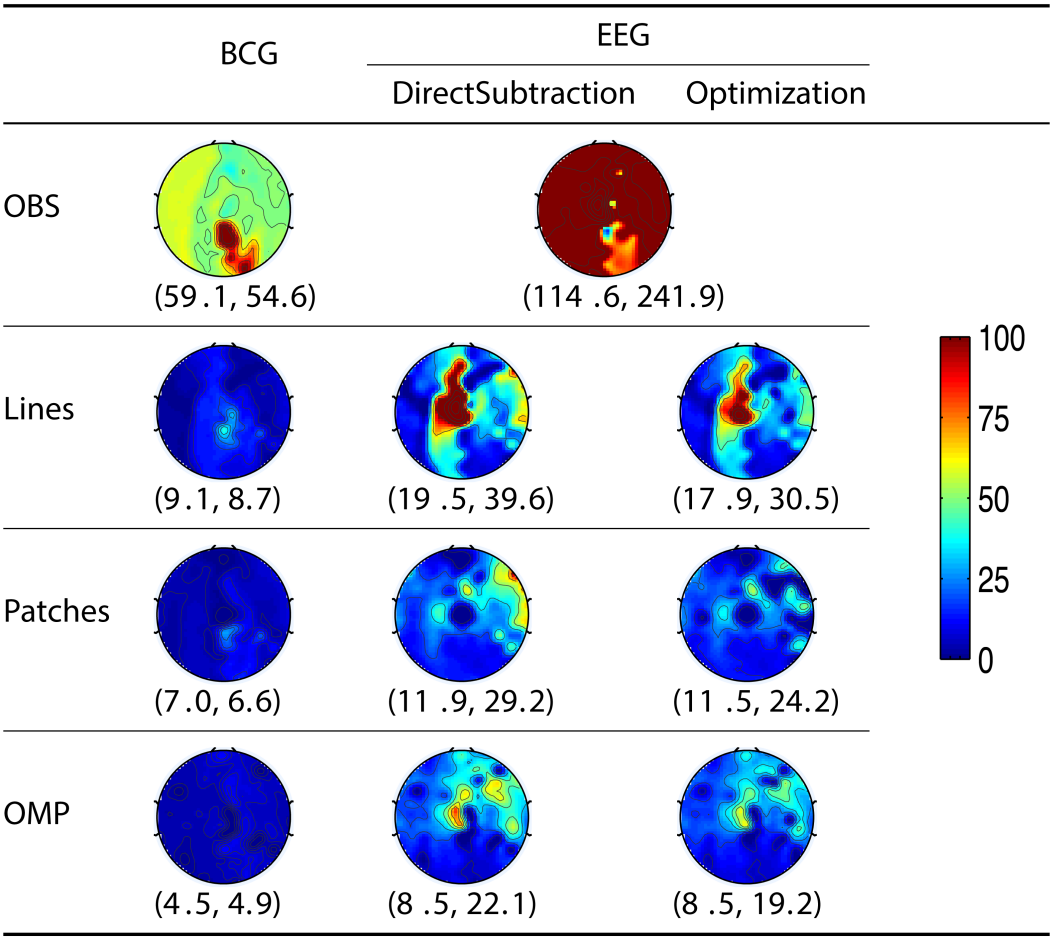

Figure 4.4: Topographic maps of $nRMSE(\%)$ after averaging all cross-validation results. The spatially collective *ave* $nRMSE$s(%) over all channels are in the brackets.

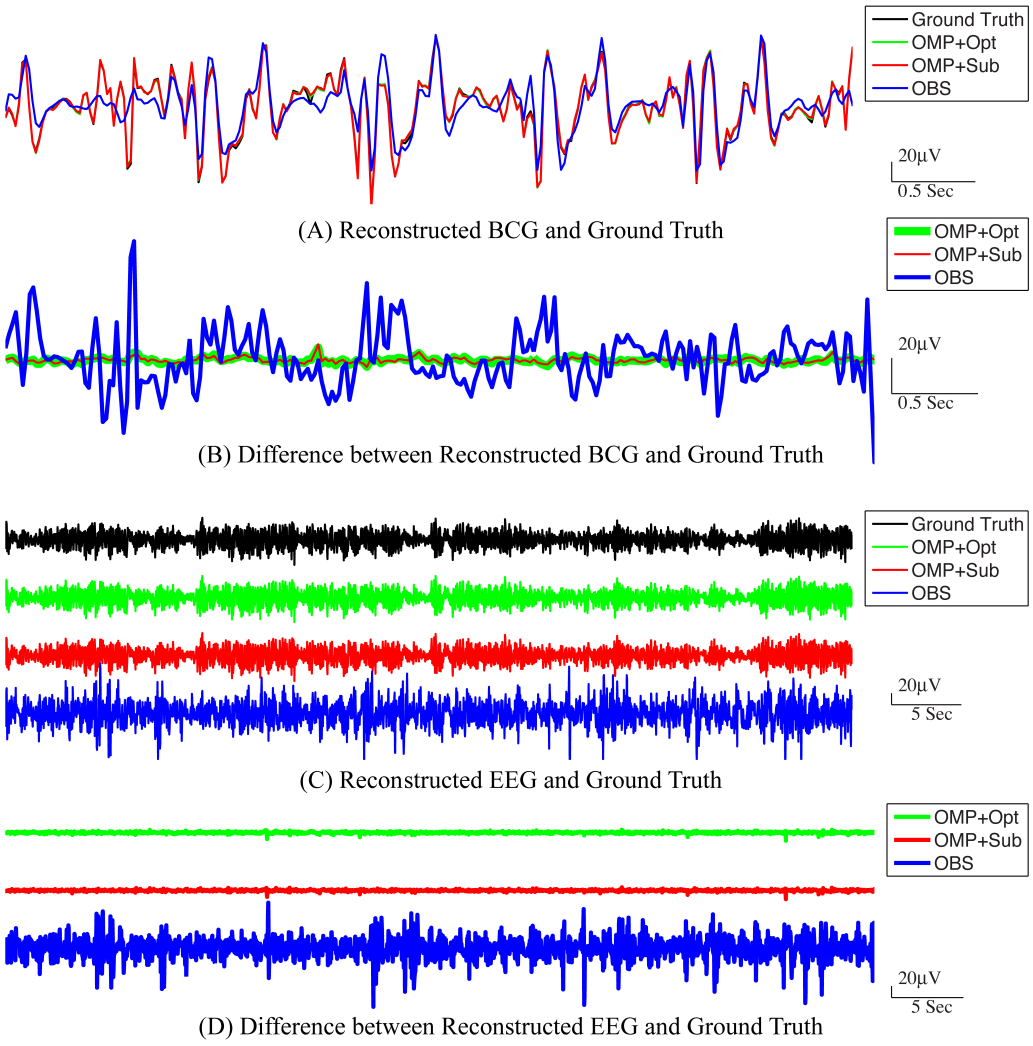

Figure 4.5: Reconstructed BCG (A) and EEG (C) from channel 118. In (A) and (C), the top panel: ground-truth used in simulation. From second to bottom panels, the methods used to reconstruct the signals are OMP with direct subtraction, OMP with Optimization-based reconstruction and OBS. The difference between the reconstructed signals and the ground truth are displayed in (B) for BCG and EEG signals, respectively.

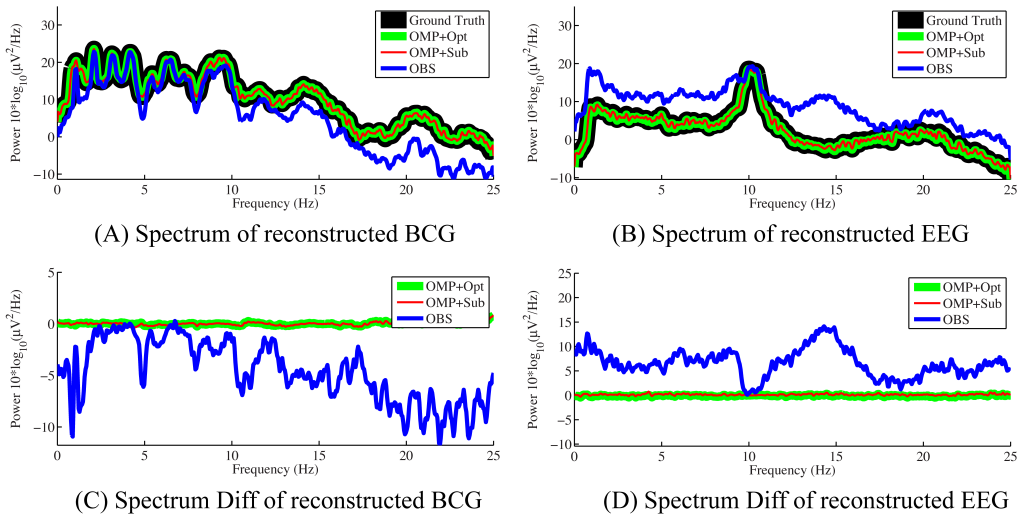

(A) Spectrum of reconstructed BCG

(B) Spectrum of reconstructed EEG

(C) Spectrum Diff of reconstructed BCG

(D) Spectrum Diff of reconstructed EEG

Figure 4.6: Frequency spectra of reconstructed BCG (A) and EEG (B) from channel 118 with 0.05Hz frequency resolution. The OMP related approaches reconstruct signals that are so close to the ground truth that their spectra almost perfectly overlap. The subtractions of the spectra between reconstructed signals and ground truth are displayed in (C) and (D) for BCG and EEG signals, respectively.

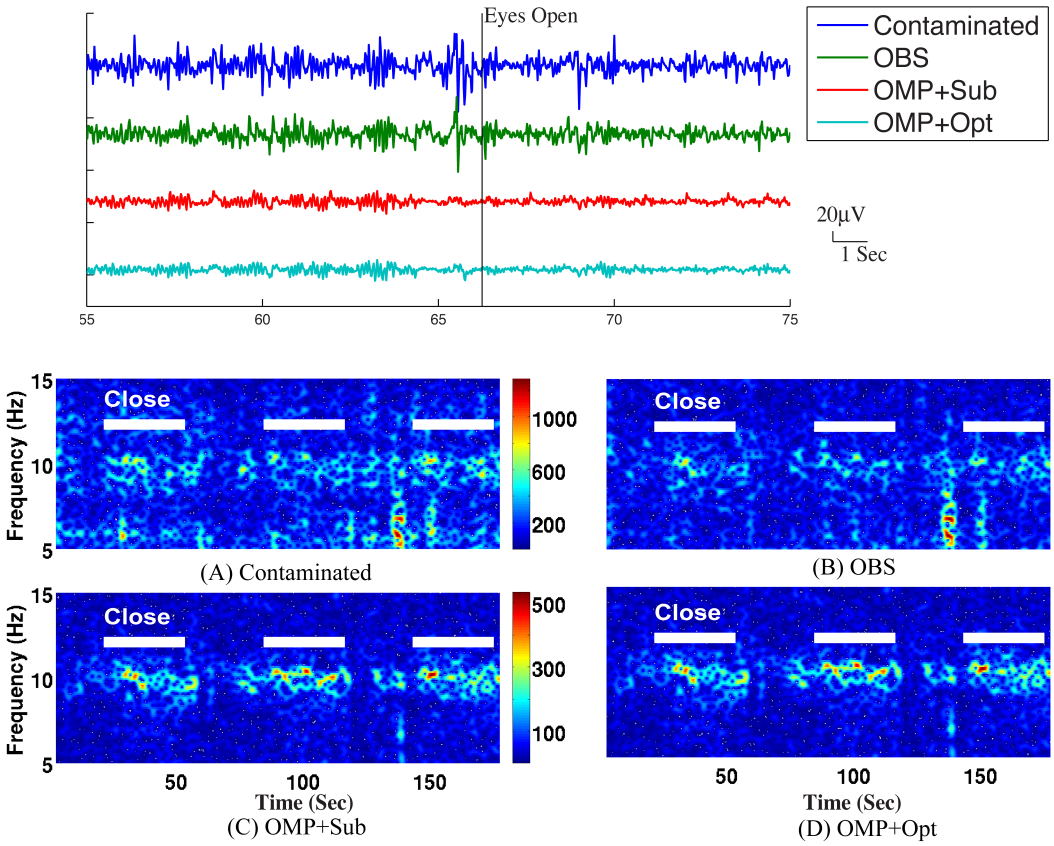

Figure 4.7: Top panel: Roughly 20-sec ranges of reconstructed EEG signals are shown here with event onsets (eyes open and eyes close). Bottom panel: Comparison of performance in differentiating the eyes open (EC) and eyes closed (EO) states: (A) based directly on contaminated EEG recording, (B) recovered EEG signals with the OBS method, and (C) the OMP with direct subtraction and (D) the OMP with optimization-based method. The left panel depicts the reconstructed EEG spectrograms.

4.6.1.2 EEG Reconstruction Results from Real Contaminated Measurements

Because it is not possible to measure ground-truth BCG and EEG components from uninsulated channels inside the scanner, the performance of EEG reconstruction can only be examined qualitatively for known EEG features. One important feature is the increased power in the alpha band (8-10Hz), primarily in the posterior electrodes, when the subjects eyes are closed (EC), compared to the eyes open (EO) condition. We collected recordings from 20 unblocked channels with BCG contamination, arranged according to the conventional 10-20 system, when three subjects were cued verbally to open and close their eyes every 30 seconds for a total time of 14 minutes. The same protocol was used to collect EEG signals outside the scanner as well, for optimization-based reconstruction, as explained in our previous work [XRC13b].

We followed the procedure of Chen, et al., [CFZ08] to quantify the EC/EO effects. Each 30-sec EEG sample, omitting 3-sec before and after each EC/EO event onset, was analyzed in 3 sec epochs, resulting in 112 epochs for each EC/EO state. The absolute EEG band power (μV^2) in the alpha band from each epoch of EC/EO state was calculated using the Fast Fourier Transform. As the alpha band power values failed a normality test, the Wilcoxon test for nonparametric comparison of ranks was performed, with $p < 0.05$ accepted as significant, to assess the hypothesis that EC and EO states have similar population mean rank based on alpha band power [CFZ08].

The top panel of Figure 4.7 illustrates qualitatively the experimentally acquired contaminated data from an occipital channel (channel 124) from one of the subjects, and the corresponding reconstructed EEG signals from OBS, OMP inference with direct subtraction and optimization-based reconstruction methods. The transition from EC to EO states are clearly identifiable at around 65 sec. EEG signals reconstructed with OMP inference model have revealed better-preserved alpha rhythm in EC state than OBS.

The spectrogram of recovered EEG from one subject are shown in the bottom panel of Figure 4.7 for quantitative comparisons while statistical results from all subjects are presented in Table 4.1. With 112 epochs, the Wilcoxon-test on the contaminated data

Table 4.1: Statistical results of one occipital channel from 3 subjects. EC columns contain mean (μV^2) alpha power when the subjects eyes were closed. EO columns contain mean (μV^2) alpha power when the eyes were open. P-values are from the Wilcoxon test. No significant change in alpha power was detected in the contaminated signal, while the OMP-based and OBS methods display the expected decreases from EC to EO conditions.

	Subject 1			Subject 2			Subject 3		
	EC	EO	p-value	EC	EO	p-value	EC	EO	p-value
Contaminated	341.6	330.8	**1.8e-01**	1781.9	1790.3	**6.6e-01**	695.2	676.4	**3.8e-01**
OBS	74.1	59.6	**2.1e-02**	75.9	65.0	**4.5e-02**	72.3	56.2	**3.1e-03**
OMP+Sub	26.7	15.4	**5.1e-06**	8.2	3.1	**9.1e-07**	5.4	1.1	**1.3e-25**
OMP+Opt	26.6	15.3	**4.4e-06**	8.1	3.0	**7.1e-08**	5.2	0.9	**6.5e-26**

indicates no marked reduction in the magnitude of alpha band power in the EO states. Agreeing with the results reported in [NBI05], statistically significant difference in alpha band power is present between the EC and EO states of the recovered EEG signals from the OBS. As expected, a more significant statistical difference is revealed using the OMP inference plus direct subtraction, and even greater difference is reported with OMP plus optimization-based reconstruction, in accordance with our results in the simulation study. Similar results are obtained from other subjects and are presented in the Supplementary Material.

4.6.2 Performance Evaluation of the Inference Model

For the purpose of efficiency and stability, it is desirable to learn the inference matrix, $\mathbf{W}$, from a short full-scalp BCG-only dataset while maintaining high estimation accuracy. To this end, we first acquired 13-min full-scalp BCG-only recordings to assess the impact of the model building length on the estimation accuracy. We then derived inference matrices from data that varied from 1 min to 4 min in the model building stage, and evaluated

the corresponding full-scalp BCG recovery errors ($nRMSE$) on the remainder. We have observed that the duration of model building has negligible effect of less than 0.3%. Hence the results in this paper are reported with the inference matrix from 1 min model building length.

4.6.2.1 Consistency Test Results for Single and Multiple Subjects

Consistency Test over Time: As discussed above, it is reasonable to expect that the spatial correlations of BCG traces among multiple channels remain consistent over time. This assumption ensures acceptable BCG estimation over time under our inference model. We validated this presumption using the following steps: First, a total of 13-minute full-scalp BCG-only recordings were partitioned into 13 equal length segments. Then, the inference matrix built from each segment (training segment) was evaluated on each of the remainder segments (testing segments), forming an error matrix of spatially collective average $ave\ nRMSE$ whose $(i,j)^{th}$ entry contains the $ave\ nRMSE$ of segment j in column direction based on the model built on segment i along row direction. The evolution of the inference relationship is visualized in Figure 4.8. As expected, the (sub)diagonal structure of the error matrix in Figure 4.8 suggests mild non-stationarity, but with a uniform upper bound of less than 10%, confirming the presence of a generally stable inference relationship.

Table 4.2: Mean values of the error matrices whose element is the BCG estimation error ($ave\ nRMSE$) in percentage (%) for a model whose subset of channels and inference matrix were learned from one training segment and applied to another testing segment. Data were from three different experimental sessions. Three columns represent three different conditions for estimating the BCG of the testing segments. Channel Consistency column: an optimal inference matrix was used in estimation. Training Inference column: both channels and inference matrix were from the training data. Recalculated Inference column: Inference matrix was updated with the proposed recalculation method.(All error matrices are presented in the supplementary material.)

	Channel Consistency			Training Inference			Recalculated Inference		
(%)	Session1	Session2	Session3	Session1	Session2	Session3	Session1	Session2	Session3
Session1	3.98	7.56	5.10	4.02	46.69	38.67	4.59	8.50	5.48
Session2	4.98	6.52	4.90	33.14	6.85	30.76	5.87	7.33	5.28
Session3	4.33	7.25	4.44	31.02	36.82	4.53	5.07	8.06	4.79

Table 4.3: The same as Table 4.2 but data were from three subjects.

	Channel Consistency			Training Inference			Recalculated Inference		
(%)	Subject1	Subject2	Subject3	Subject1	Subject2	Subject3	Subject1	Subject2	Subject3
Subject1	3.92	5.43	5.51	4.11	38.88	38.23	4.44	6.49	6.81
Subject2	5.01	4.68	5.63	41.94	4.83	50.15	5.83	5.44	6.72
Subject3	5.36	5.63	4.78	47.32	48.13	5.04	6.24	6.62	5.51

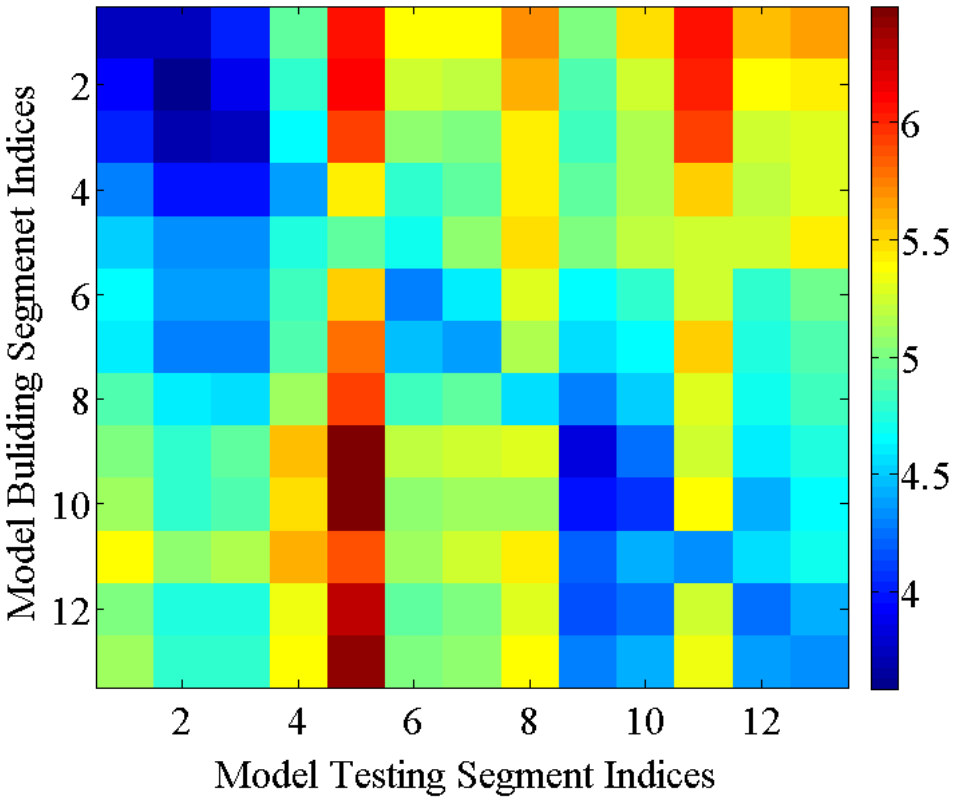

Figure 4.8: BCG estimation errors (*ave nRMSE*) in percentage (%) exhibit (sub)diagonal structure for models built on one segment and applied to another segment.

Channel Consistency Test: We performed a similar validation testing the representativeness of selected channels on full-scalp 5-minute BCG-only recordings from three experimental sessions of the same subjects, and three sessions of 9-minute recordings from three subjects. Error matrices were generated after dividing each recording into 1-minute long segments. Mean values of the error matrices are presented in Channel Consistency column of both Table 4.2 and 4.3, while the raw error matrices of all consistency tests are shown in the Supplementary Material. Highest accuracy is achieved in general when the training and testing segments are from the same session or subject, emphasizing the necessity of subject-specific channel selection.

An optimal inference matrix, built directly from the testing rather than the training segment, was applied in each testing segment estimation using the channels selected from the training segment. With less than 2% increase in errors (from the consistent errors for each testing data), the selected channels are representative not only for different experiment sessions but also for different subjects.

Consistency Test with Inference Matrix from Training: Without applying the optimal inference matrix, we obtained the mean values from the error matrices when the channels and inference matrix were both from the training data and presented the result in Training Inference column of both Table 4.2 and 4.3. Combining the results from Channel Consistency column and Training Inference column, it is safe to conclude that the observed excessive errors (in Training Inference column) should originate mainly from the inconsistency of inference matrix rather than from the selecting channels failing to be representative. This observation also helps us to determine a fixed blocking pattern, especially when lower BCG-only estimation accuracy is tolerable; in practice this might greatly reduce experiment time and complexity

Consistency Test with Recalculated Inference Matrix: Furthermore, the application of our inference matrix recalculation method decreases the errors to reasonable levels (most errors are approximately bounded above by 10%) as illustrated in Table 4.2 and 4.3

(Recalculated Inference column), agreeing with the theoretical proof in the Supplementary Material.

4.6.2.2 Determination of "Budget" Size

A 13-fold cross-validation was employed to determine the size of the subset Λ_{ins} with 13 one-minute segments from the 13-minute full-scalp BCG-only signals: for each test in the k-fold process, the one minute training data from the k^{th}-minute BCG signals was denoted as $\mathbf{X}_{bcg}{}^{(k)}$, and the validation data from the remaining 12-minutes was denoted as $\overline{\mathbf{X}}^{(k)}{}_{bcg}$. The inference matrix $\mathbf{W}$ was built first by solving Equation 4.3. on the training data with a specific "budget" size, and then applied on the validation set to estimate the BCG components from the non-insulated channels. Spatial collective average errors from estimating the validation sets were calculated for different folds, and for different "budget" sizes. The averaged *ave nRMSE*s over 13 different validation sets decreases as the "budget" size increases, as shown in Figure 4.9. In this paper, we chose $|\Lambda_{ins}|$ to be 20 as we determined that a consistent 5% estimation error is acceptable.

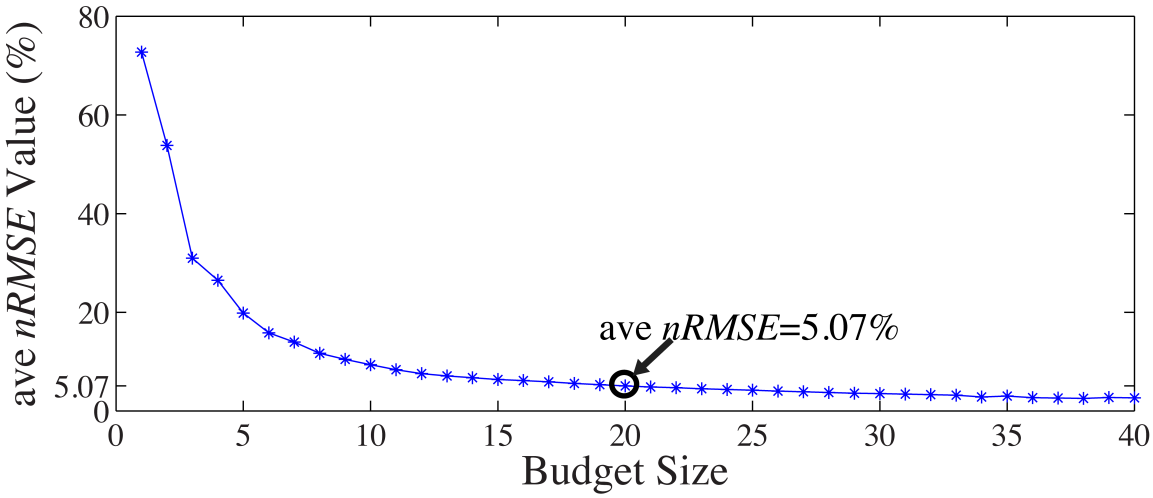

Figure 4.9: Mean *ave nRMSE*(%) of 12 validation sets as a function of "budget" size.

4.6.2.3 Inference Performance of "Random" Patterns

The general set selection problem resembles "set selection" problems in compressed sensing, which maximizes the ℓ_2 fidelity (inference goal here) subject to ℓ_0 constraint (the cardinality of Λ_{ins}). In practice, the Restricted Isometry Property-type [CT05] conditions are hard to verify, especially with the high variation in BCG. However, it would be desirable to obtain insights from reconstruction performance based on randomly selected subsets. To this end, we repeated the channel selection process, drawing $|\Lambda_{ins}| = 20$ channels from Λ_{full} with random permutation. Figure 4.10(A) illustrates one of the "random" patterns and Figure 4.10(B) shows a histogram of the errors ($ave\ nRMSE$) corresponding to 500 "random" patterns. The average of $ave\ nRMSE$ over 500 realizations is 5.65% with a maximum error at 7.85% and a minimum at 4.7%. Figure 4.11 reports the topographic maps of $nRMSE$ when the model building length is 1 min, and shows that the OMP approach achieves better BCG estimation performance than the other two *ad hoc* insulation patterns. Comparing Figure 4.10 and Figure 4.11, we notice that the "random" pattern consistently performs better than the "lines" pattern. On average, the "random" pattern performs better than the "patches" pattern and worse than the pattern from the OMP approach. As can be observed, only a few instances would result in estimation accuracies higher than the one from the OMP approach who yields consistently good estimation results.

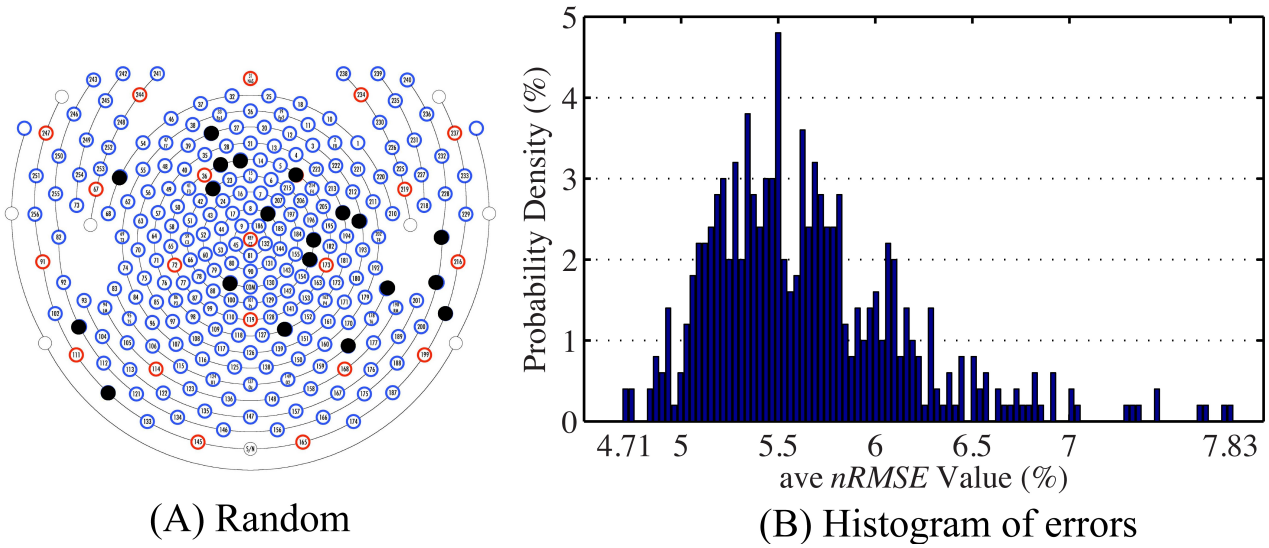

Figure 4.10: (A) One of the patterns selected with random permutation. (B) Histogram of the estimation errors (*ave nRMSE*) from 500 realizations of random patterns. The highest error is 7.83% when the lowest error is 4.71%.

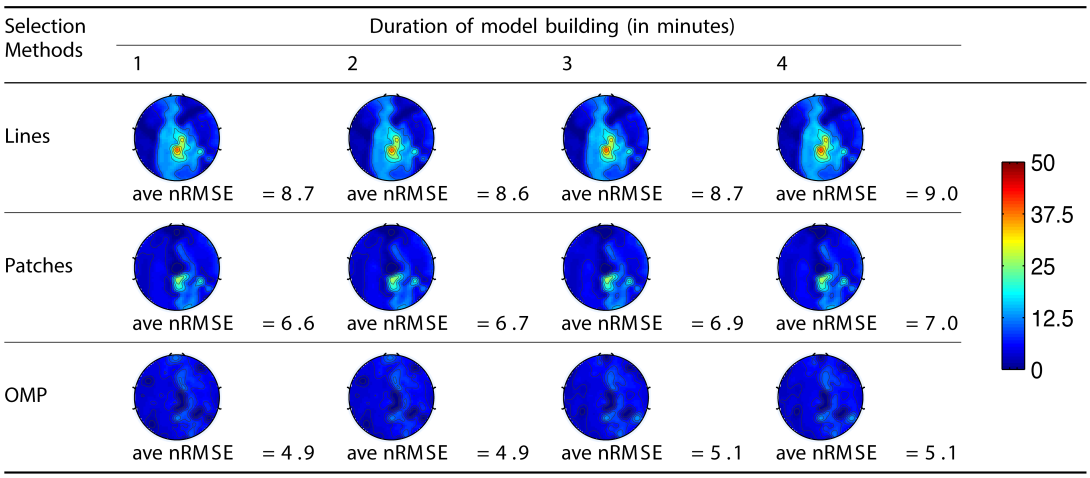

Figure 4.11: Topographic BCG estimation error (*nRMSE*) maps in percentage (%) for different channel selection methods when the model building duration is 1 min. The number at the bottom of each error map: the *ave nRMSE* averaged spatially across all channels.

4.7 Discussions and Conclusion

With increased magnitude at higher MR field strengths and high temporal non-stationarity, BCG artifacts have impeded further investigations using concurrent EEG-fMRI. Previous solutions to this problem focus mainly on PCA or ICA-based approaches, addressing this issue by channel-wise temporal modeling of BCG. To take full advantage of the spatial information from a high-density EEG cap, it is natural to extend to spatial PCA/ICA [BAW03, SCL05]. However, the success of modeling BCG with such spatial PCA/ICA approaches demands the existence of questionable [GVK07, VDR10]orthogonality or independence relationship between the full-scalp BCG and EEG signals. By contrast, our approach imposes no presumptions on the relationship between BCG and EEG, and relies on a consistent inference model that maps BCG from a subset of channels to BCG from all channels. With 20 degrees of freedom, the inference model produces an observation-space-to-observation-space map that is robust to variations in BCG source space. Unlike spatial PCA/ICA that requires prior selection of the number of components or subjective identification of components, our estimation of BCG is based on the widely accepted additive generative model.

Extending from our previous work, which used the BCG recordings from subjectively-selected insulated neighboring channels, the present study: (1) estimates the full-scalp BCG components for all channels from an automatically selected insulation set; (2) reconstructs all channels at once with significantly improve quality since it relies on stable global rather than ad-hoc local neighboring BCG information; (3) simplifies the experimental setup by insulating only a small subset of channels. The inference model has improved the estimation accuracy of BCG greatly across all channels, since the inference relationship is generally consistent in time and the selected channels are reasonably consistent not only across experimental sessions but also across subjects, suggesting that the subject-specific channel selection is less essential when some inaccuracy of BCG estimation accuracy is tolerated. In spite of the observed rather significant inconsistency of the inference matrix across sessions, our proposed inference matrix recalculation method effectively keeps the errors below 10% upper bound which is only approximately 1-2% worse in comparison to those where optimal

inference matrices were adopted.

In practice, our inference model involving only linear regressions is easy to build and calculate, with a few minutes of experimental time for model-building stage I, and with no hardware modifications, unlike other methods [DGS09] utilizing multiple channels of EEG cap. In addition, while we developed our method on a high density cap, it can be applied to a lower density cap with some variations in BCG reconstruction accuracy. Once the inference matrix is learned, the mitigation of BCG artifacts, with our inference approach and direct subtraction-based reconstruction, is suitable for on-line artifact removal, requiring only multiplication and subtraction that can be performed in real-time. Note that the direct subtraction approach in Equation 4.6 works best when the observation noise ε in Equation 4.1 is relatively low. In realistic measurement settings, the noise level is not accessible directly, and can be estimated only under certain distributional assumptions. Practically, this seems to be reasonable: we have observed that subtraction-based reconstruction works well on both synthesized and real contaminated data. For localized inference of interest, e.g. occipital channels for alpha rhythm studies, the proposed method can be modified trivially (the regression goal in Equation 4.3) to for selective optimization.

Moreover, our method can be integrated with these approaches, such as the KappaMetrics fEEG$^{\text{TM}}$ system and others [BPJ02, MAF07, CMG14], that generate BCG reference signals, providing guidance for placements of motion sensors, wire loops and fewer number of channels for the reference layer. Those reference-based methods are attractive however require specialized hardware. For example we were not able to compare it directly because it is not available. Admittedly, there exists some discrepancy between each of these reference signals and the "ground-truth" BCG signals, as a result of insulation, sensing process or impedance mismatch. In principle, Hall effects [CMG14, MHB13, YMG10] occurring in the MR imaging field might distort the scalp topography of the EEG signals. It is difficult to estimate the magnitude of this contaminant, which is common to OBS and other reference signal based methods.

This paper has focused mainly on removing BCG signals for non-ERP studies. Although our method in principle extends to ERP studies, the artifact suppression effects may not

significantly outperform the OBS method, as shown in Supplementary Material, due to the fact that averaging around known triggering events will reduce BCG residual signals when event timing is not correlated to the heartbeats. A crucial result reported here, is that our method is robust in exposing alpha power fluctuations under experimental conditions. In our hands this had been a difficult challenge when using other artifact removal methods, and has limited sharply the value of combined EEG-fMRI experiments that seek to look at continuously recorded signals and to analyze their spectral content.

Combined, the proposed framework can do much to mitigate the serious artifacts that otherwise limit combined EEG-fMRI recordings. The practical advantage of doing so may be very large. While many groups have shown important results of combined EEG-fMRI in the event-related designs that are relatively resistant to the BCG artifacts; few reports show success in continuous recordings. The latter, however, are necessary to study the tantalizing relationships between BOLD signal and brain EEG rhythms, as well as important disease entities such as epilepsy, where there is little opportunity to average EEG events.

4.8 Supplementary Material

4.8.1 Proof of the inference matrix recalculation method

We denote the contaminated data as $\mathbf{Y} \in \mathbb{R}^{C \times T}$, with C being the number of channels and T being the number of time points of the recordings. The time points are further decomposed into K segments with L points each according to some integer number of heartbeat cycles.

Averaging of all the segments is equivalent to right multiplying a circulant matrix $\mathbf{A} \in$

$\mathbb{R}^{KL\times L}$ formed from a scalar $\frac{1}{K}$ and vertically stacking K identity matrices $\mathbb{1}$ with length L:

$$\mathbb{1} = \begin{pmatrix} 1 & 0 & \cdots & 0 \\ 0 & 1 & \cdots & 0 \\ \vdots & \vdots & \ddots & \vdots \\ 0 & 0 & \cdots & 1 \end{pmatrix} \in \mathbb{R}^{L\times L}, \mathbf{A} = \frac{1}{K} \begin{pmatrix} 1 & 0 & \cdots & 0 \\ 0 & 1 & \cdots & 0 \\ \vdots & \vdots & \ddots & \vdots \\ 0 & 0 & \cdots & 1 \\ \vdots & \vdots & \vdots & \vdots \\ 1 & 0 & \cdots & 0 \\ 0 & 1 & \cdots & 0 \\ \vdots & \vdots & \ddots & \vdots \\ 0 & 0 & \cdots & 1 \end{pmatrix} = \frac{1}{K} \begin{pmatrix} \mathbb{1} \\ \vdots \\ \mathbb{1} \end{pmatrix} \in \mathbb{R}^{KL\times L}.$$

To maintain the size along the time direction after averaging, the resultant matrix is replicated K times, which is equivalent to right multiplying another circulant matrix formed from stacking identify matrices with length L horizontally. Combined, averaging and replicating the segments is equivalent to right multiplying a circulant matrix $\mathbf{C} \in \mathbb{R}^{KL\times KL}$:

$$\mathbf{C} = \frac{1}{K} \begin{pmatrix} \mathbb{1} & \cdots & \mathbb{1} \\ \vdots & \ddots & \vdots \\ \mathbb{1} & \cdots & \mathbb{1} \end{pmatrix} \in \mathbb{R}^{KL\times KL}.$$

Naturally, we have the following relations:

$$\begin{aligned} \bar{\mathbf{Y}} &= \mathbf{Y}\mathbf{C}, \\ \bar{\mathbf{X}}_{bcg} &= \mathbf{X}_{bcg}\mathbf{C}, \\ \bar{\mathbf{X}}_{eeg} &= \mathbf{X}_{eeg}\mathbf{C}, \\ \bar{\mathbf{Y}} &= \bar{\mathbf{X}}_{bcg} + \bar{\mathbf{X}}_{eeg} \in \mathbb{R}^{C\times KL}, \end{aligned} \tag{4.8}$$

As in previous papers by [NBI05, AJT00], we assume that EEG becomes uncorrelated after 3 sec. Choosing K and L properly, we assume $\bar{\mathbf{X}}_{eeg} \to 0$ and $\bar{\mathbf{Y}}$ becomes a good representation of $\bar{\mathbf{X}}_{bcg}$ as as result of the averaging.

Ideally, we derive our inference matrix from the following:

$$\widetilde{\mathbf{W}} = \arg\min_{\widetilde{\mathbf{W}}} \left\| \mathbf{X}_{bcg}[\Lambda_{full}, :] - \widetilde{\mathbf{W}}\mathbf{X}_{bcg}[\Lambda_{ins}, :] \right\|_F^2. \tag{4.9}$$

We propose to recalculate the inference matrix from the following:

$$\bar{\mathbf{W}} = \arg\min_{\bar{\mathbf{W}}} \left\| \bar{\mathbf{Y}}[\Lambda_{full}, :] - \bar{\mathbf{W}} \mathbf{X}_{bcg}[\Lambda_{ins}, :] \right\|_F^2. \tag{4.10}$$

We will show that $\bar{\mathbf{W}}$ can recover $\bar{\mathbf{X}}_{bcg}[\Lambda_{full}, :]$ from $\mathbf{X}_{bcg}[\Lambda_{ins}, :]$ with high accuracy. For convenience, we denote $\mathbf{X}_{bcg}[\Lambda_{ins}, :]$ as $\mathbf{X}_0$, $\mathbf{X}_{bcg}[\Lambda_{full}, :]$ as $\mathbf{X}$, and $\bar{\mathbf{X}}_{bcg}[\Lambda_{full}, :]$ as $\bar{\mathbf{X}}$.

After replacing $\bar{\mathbf{Y}}$ with $\bar{\mathbf{X}}_{bcg}$, the solutions to the least square problems above are:

$$\begin{aligned}
\widetilde{\mathbf{W}} &= \mathbf{X}\mathbf{X}_0^T(\mathbf{X}_0\mathbf{X}_0^T)^{-1}, \\
\bar{\mathbf{W}} &= \bar{\mathbf{X}}\mathbf{X}_0^T(\mathbf{X}_0\mathbf{X}_0^T)^{-1} = \mathbf{X}\mathbf{C}\mathbf{X}_0^T(\mathbf{X}_0\mathbf{X}_0^T)^{-1}, \\
\widetilde{\mathbf{W}} - \bar{\mathbf{W}} &= (\mathbf{X} - \mathbf{X}\mathbf{C})\,\mathbf{X}_0^T(\mathbf{X}_0\mathbf{X}_0^T)^{-1}.
\end{aligned} \tag{4.11}$$

The solutions above in Equation 4.11 minimize the residuals of the least square problems, where these residuals ϵ_1 and ϵ_2 are small quantities:

$$\begin{aligned}
\epsilon_1 &= \frac{\left\| \widetilde{\mathbf{W}}\mathbf{X}_0 - \mathbf{X} \right\|_F^2}{\|\mathbf{X}\|_F^2}, \\
\epsilon_2 &= \frac{\left\| \bar{\mathbf{W}}\mathbf{X}_0 - \mathbf{X}\mathbf{C} \right\|_F^2}{\|\mathbf{X}\mathbf{C}\|_F^2}.
\end{aligned} \tag{4.12}$$

As any circulant matrix can be diagonalized by the Discrete Fourier Transform (DFT) matrix $\mathbf{F}$, we have $\mathbf{C} = \mathbf{F}\mathbf{\Lambda}\mathbf{F}^T$. In addition, the eigenvalues of $\mathbf{C}$ are known, and have a certain structure: $\mathbf{\Lambda}$ contains zeros except L ones at its diagonal.

$$\lambda_{i,j} = \begin{cases} 1 & \text{if } i = j \text{ and } i,j \leq L \\ 0 & \text{otherwise} \end{cases}$$

Therefore,

$$\begin{aligned}
&\mathbf{X}\mathbf{C} = \mathbf{X}\mathbf{F}\mathbf{\Lambda}\mathbf{F}^T \\
&\mathbf{I} - \mathbf{\Lambda} = (\mathbf{I} - \mathbf{\Lambda})^2 = \mathbf{I} - \mathbf{\Lambda}^2 \\
&\|\mathbf{X}\|_F^2 = \mathbf{X}\mathbf{X}^T = \mathbf{X}\mathbf{F}\mathbf{I}\mathbf{F}^T = \mathbf{X}\mathbf{F}(\mathbf{I} - \mathbf{\Lambda}^2 + \mathbf{\Lambda}^2)\mathbf{F}^T = \mathbf{X}\mathbf{F}(\mathbf{I} - \mathbf{\Lambda}^2 + \mathbf{\Lambda}^2)\mathbf{F}^T \\
&= \mathbf{X}\mathbf{F}(\mathbf{I} - \mathbf{\Lambda})^2\mathbf{F}^T + \mathbf{X}\mathbf{F}(\mathbf{\Lambda})^2\mathbf{F}^T = \|\mathbf{X} - \mathbf{X}\mathbf{C}\|_F^2 + \|\mathbf{X}\mathbf{C}\|_F^2.
\end{aligned} \tag{4.13}$$

We notice that $\mathbf{X}\mathbf{F}\mathbf{\Lambda}\mathbf{F}^T$ has a physical interpretation. $\mathbf{X}\mathbf{F}$ implies application of a discrete fourier transform to each time series (row vector) in $\mathbf{X}$. $\mathbf{X}\mathbf{F}\mathbf{\Lambda}$ means applying a rectangular

low pass filter of length L with a cutoff frequency at $\frac{1}{K}f_s$ where f_s is the sampling frequency. The low-passed version then is transformed to the time domain through the inverse fourier transform by multiplying by $\mathbf{F}^T$. Accordingly, $\|\mathbf{XC}\|_F^2$ represents the energy of the BCG in the low frequency range whose cutoff depends on $\mathbf{\Lambda}$, and the energy in the high frequency range is $\|\mathbf{X}-\mathbf{XC}\|_F^2$. After observing the ground-truth BCG spectrum, as shown in the main body Figure 8, it is reasonable to argue that the percentage of the high frequency energy over the energy of all frequencies $r = \dfrac{\|\mathbf{X}-\mathbf{XC}\|_F^2}{\|\mathbf{X}\|_F^2}$ is a small quantity

The normalized percentage difference of reconstructed signals between the ideal inference matrix and the recalculated one is:

$$
\begin{aligned}
\frac{\left\|\bar{\mathbf{W}}\mathbf{X}_0 - \widetilde{\mathbf{W}}\mathbf{X}_0\right\|_F^2}{\|\mathbf{X}\|_F^2} &= \frac{\left\|\bar{\mathbf{W}}\mathbf{X}_0 - \mathbf{X} + \mathbf{X} - \widetilde{\mathbf{W}}\mathbf{X}_0\right\|_F^2}{\|\mathbf{X}\|_F^2} \\
&\leq \frac{\left\|\bar{\mathbf{W}}\mathbf{X}_0 - \mathbf{X}\right\|_F^2}{\|\mathbf{X}\|_F^2} + \frac{\left\|\mathbf{X} - \widetilde{\mathbf{W}}\mathbf{X}_0\right\|_F^2}{\|\mathbf{X}\|_F^2} \\
&= \frac{\left\|\bar{\mathbf{W}}\mathbf{X}_0 - \mathbf{X}\right\|_F^2}{\|\mathbf{X}\|_F^2} + \frac{\left\|\mathbf{X} - \mathbf{XC} + \mathbf{XC} - \widetilde{\mathbf{W}}\mathbf{X}_0\right\|_F^2}{\|\mathbf{X}\|_F^2} \\
&\leq \frac{\left\|\bar{\mathbf{W}}\mathbf{X}_0 - \mathbf{X}\right\|_F^2}{\|\mathbf{X}\|_F^2} + \frac{\|\mathbf{X} - \mathbf{XC}\|_F^2}{\|\mathbf{X}\|_F^2} + \frac{\left\|\mathbf{XC} - \widetilde{\mathbf{W}}\mathbf{X}_0\right\|_F^2}{\|\mathbf{X}\|_F^2} \\
&\leq \frac{\left\|\bar{\mathbf{W}}\mathbf{X}_0 - \mathbf{X}\right\|_F^2}{\|\mathbf{X}\|_F^2} + \frac{\|\mathbf{X} - \mathbf{XC}\|_F^2}{\|\mathbf{X}\|_F^2} + \frac{\left\|\mathbf{XC} - \widetilde{\mathbf{W}}\mathbf{X}_0\right\|_F^2}{\|\mathbf{XC}\|_F^2} \\
&= \epsilon_1 + r + \epsilon_2.
\end{aligned}
\tag{4.14}
$$

In sum, since the percentage difference is bounded by the sum of three small quantities, the recalculated inference matrix is indeed a satisfying replacement.

4.8.2 Supplementary Figures

4.8.2.1 Figures for Experimental Setup

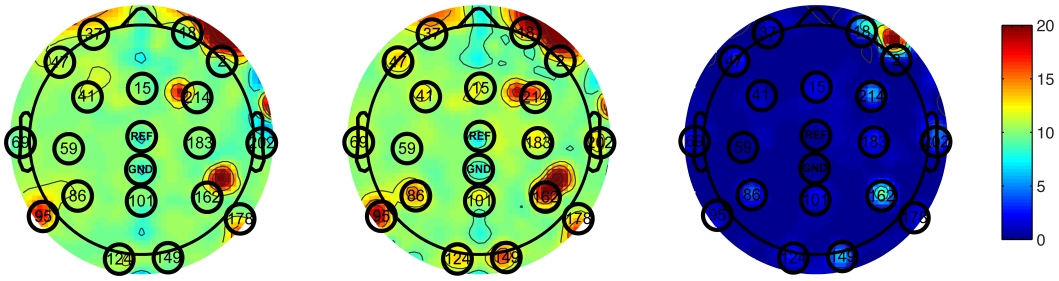

Figure 4.12: The numbers shown on the topographic maps are channel numbers. The conventional channels along with the reference and ground channels are highlighted with black circles. The color indicates the measured impedance number in kΩ. (A) Measured Impedance when all channels are blocked. (B) Measured impedance when reference and ground channels along with conventional 20 channels are unblocked. (C) The difference of impedance between (A) and (B). The average of the difference is approximately 100Ω

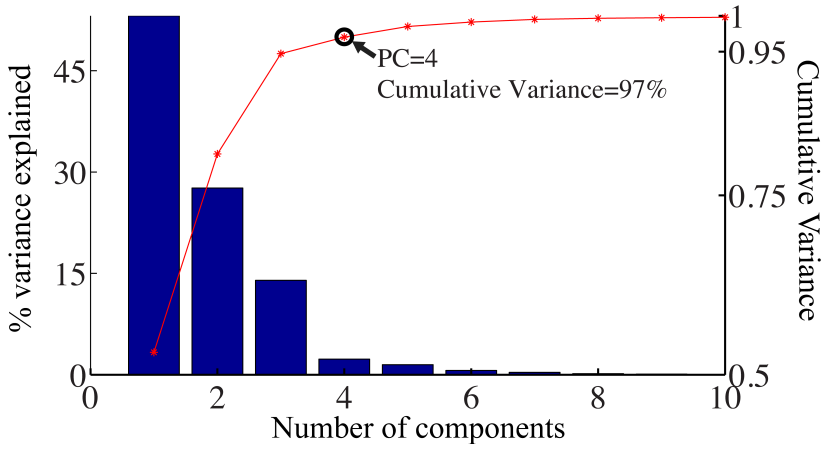

Figure 4.13: The amount of full-scalp BCG variance explained by principal components. Bar plot with ordinate labeling on the left side: the percentage of variance explained by each principal component. Red curve with the ordinate labeling on the right side: The cumulative proportion of the variance explained. The circled value indicates the number of principal components necessary to explain 97% of the total variance.

4.8.2.2 Figures for Results from Real Contaminated eyes open/close Data

No significant change in alpha power was detected in the contaminated signal, while the OMP-based and OBS methods display the expected decreases from EC to EO conditions. The left panel of the following figures depicts the reconstructed EEG spectrograms. The right panel displays the Wilcoxon rank test results of alpha band power comparisons between the EO and EC states; standard errors are indicated.

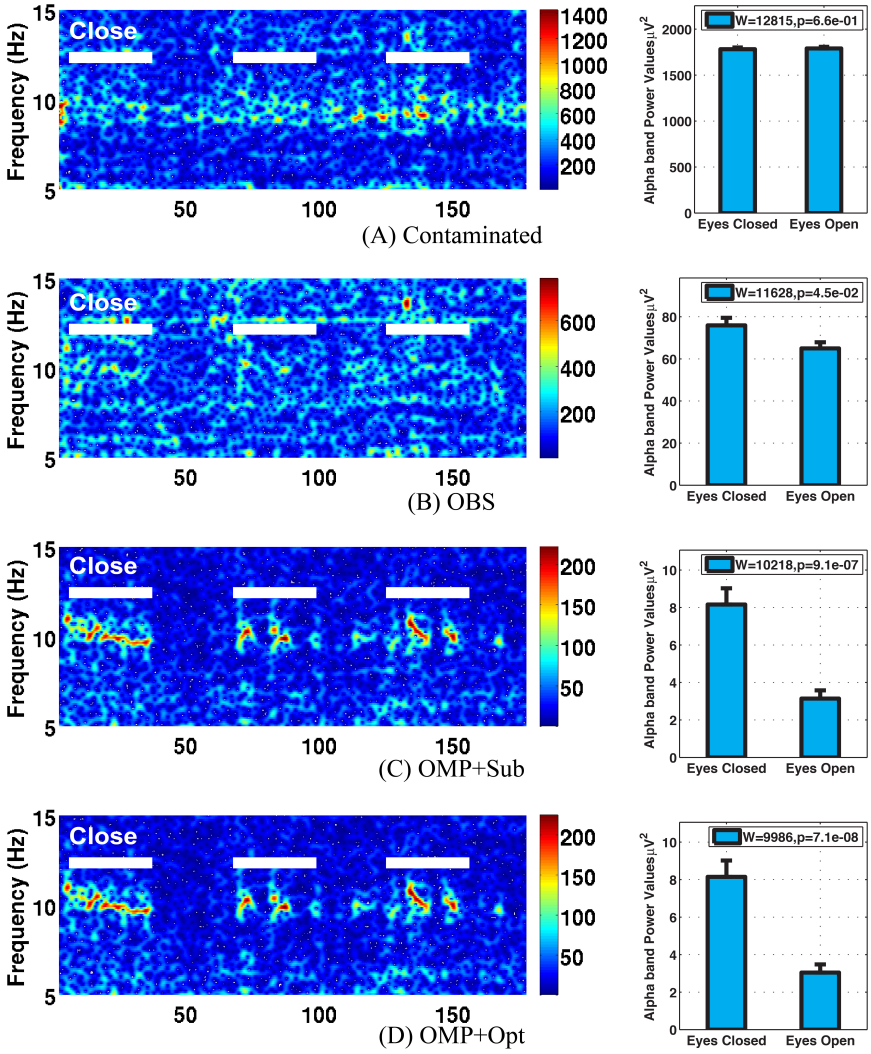

Figure 4.14: Comparison of performance in differentiating the eyes open (EC) and eyes closed (EO) states from Subject 1: (A) based directly on contaminated EEG recording, (B) recovered EEG signals with the OBS method, and (C) the OMP with direct subtraction and (D) the OMP with optimization-based method.

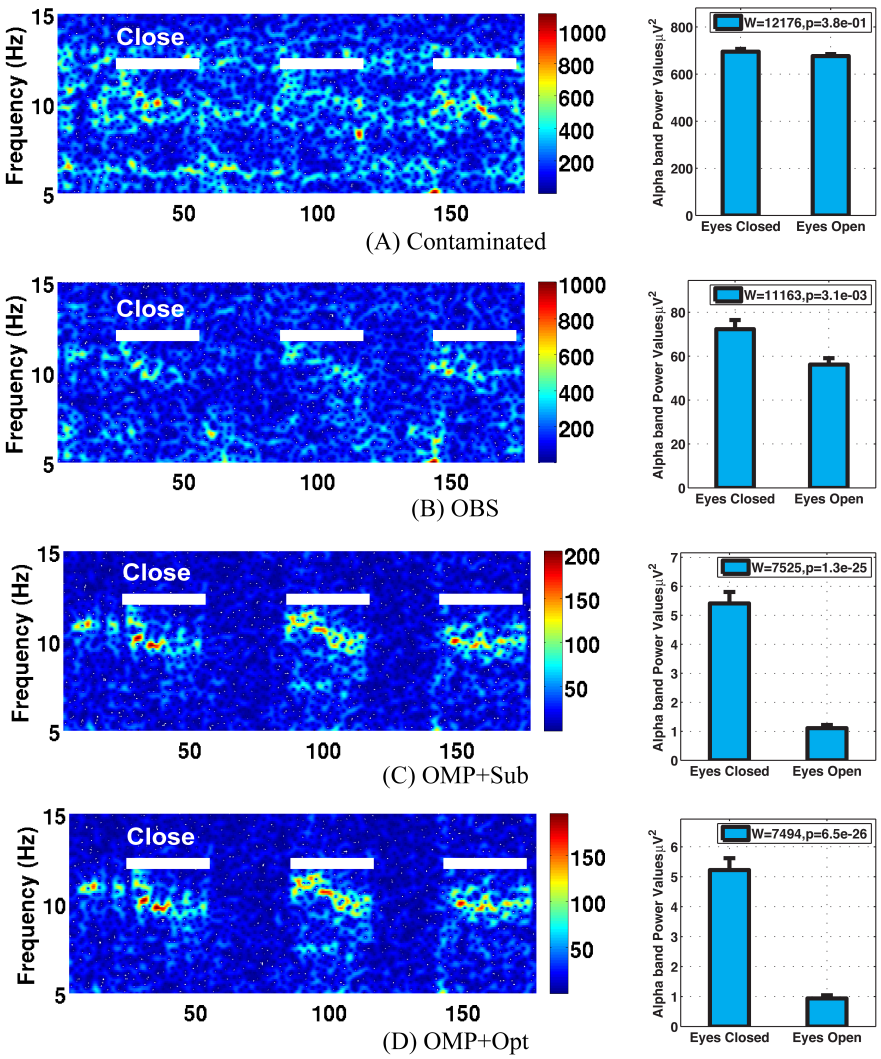

Figure 4.15: Comparison of performance in differentiating the eyes open and closed states from Subject 2, a different subject than Supplementary Figure 4.14. (C) and (D) are results from OMP with direct subtraction and optimization-based method, showing more statistically significant difference between the alpha power changes of EC and EO states than (A) and (B) which are from the contaminated data and the reconstructed EEG data from the OBS method.

4.8.2.3 ERP results from two subjects

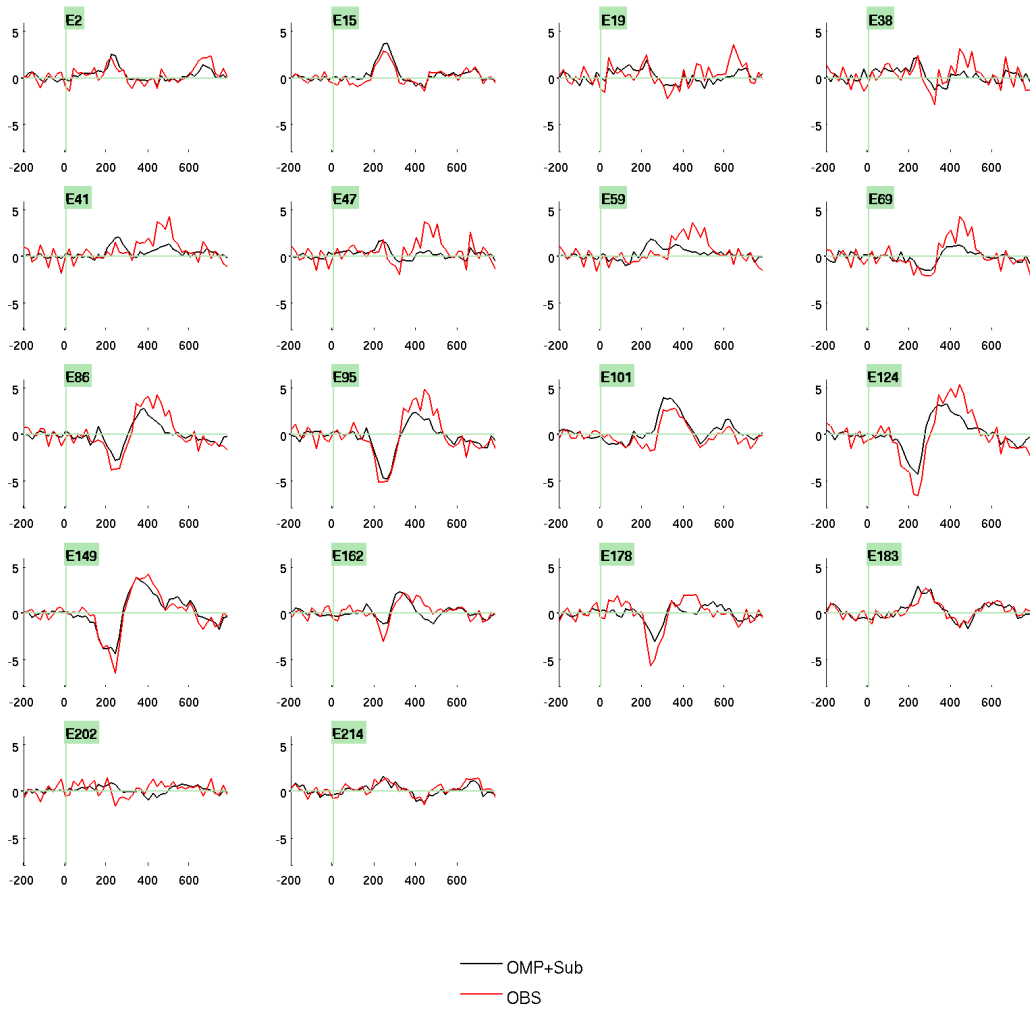

Figure 4.16: Comparison of performance in visual event-related potentials averaged from 150 epochs from Subject 1: Black lines represent reconstructed ERPs using the OMP inference method with Direct Subtraction; Red lines represent ERPs when the OBS method is used.

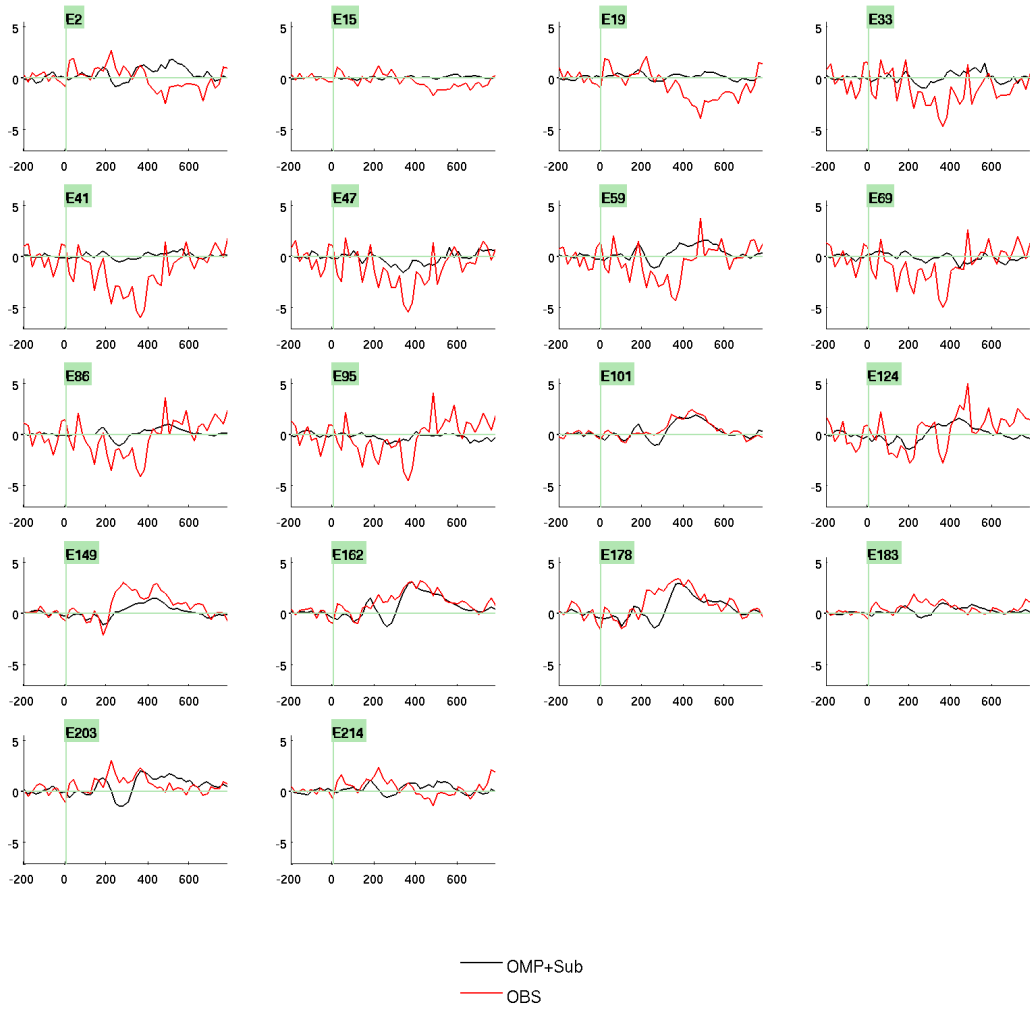

Figure 4.17: Comparison of performance in visual event-related potentials averaged from 150 epochs from Subject 2. Results from the OMP method with a direct subtraction (black lines) appear to be less noisy than the ERP shapes from the OBS method (red lines)

4.8.2.4 Figures for Consistency Tests

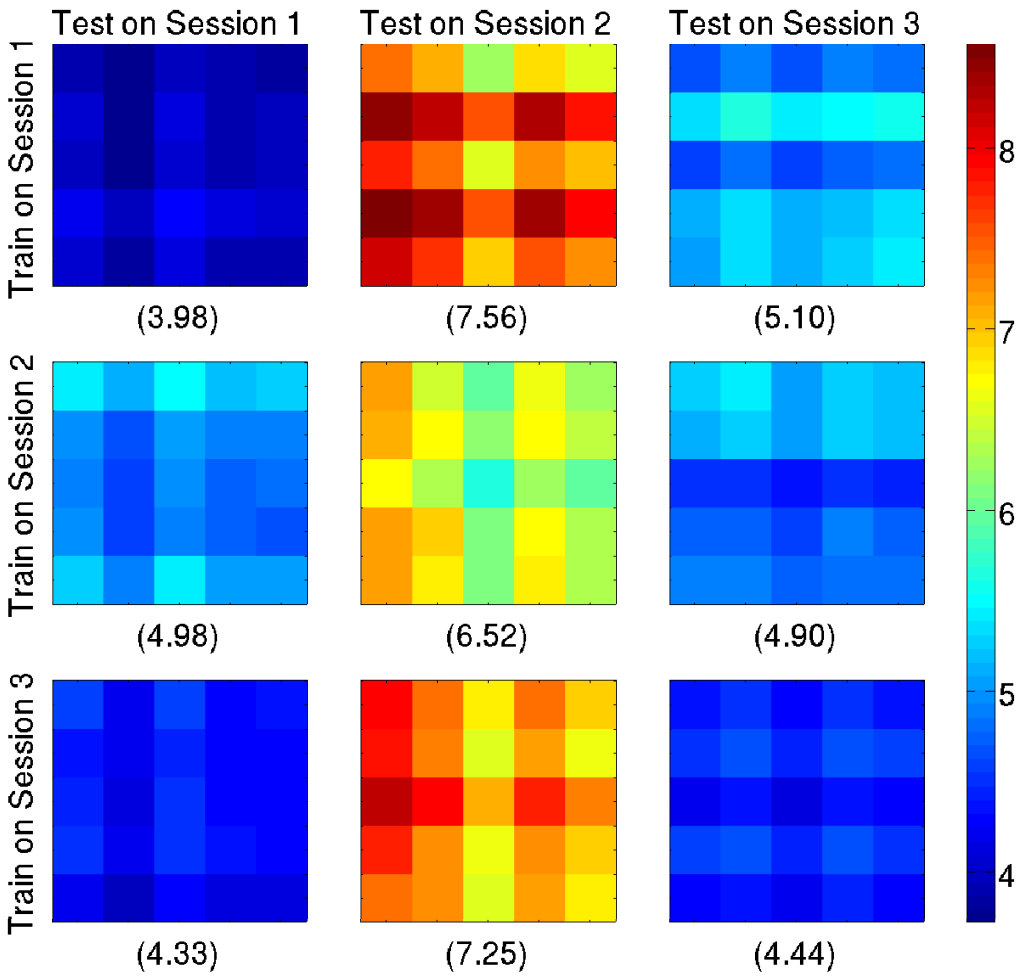

Figure 4.18: BCG estimation errors (*ave nRMSE*) in percentage (%) for models whose subset of channels were learned from one training segment and applied to another testing segment of the same subject when the corresponding inference matrix was updated from the testing segment. Mean of each error matrix is shown in the bracket underneath.

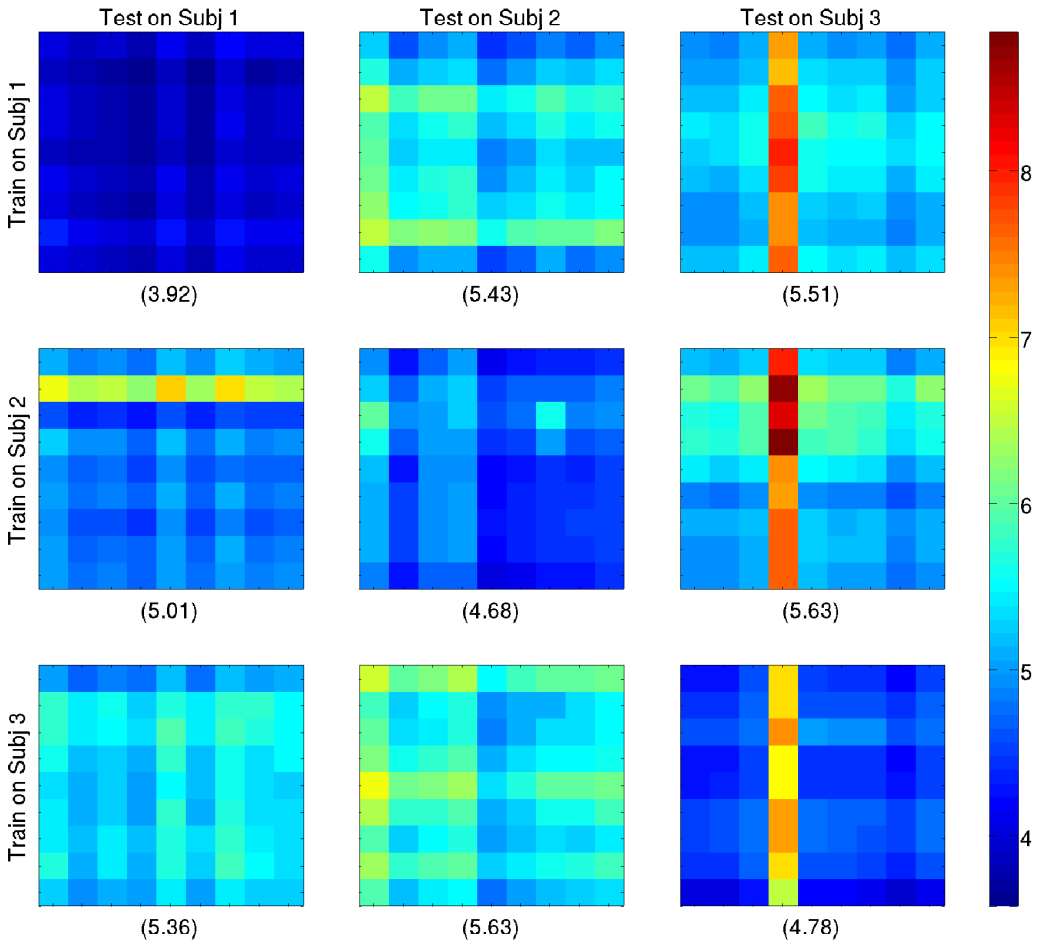

Figure 4.19: BCG estimation errors (*ave nRMSE*) in percentage (%) for models whose subset of channels were learned from a training segment and applied to another testing segment when the corresponding inference matrix was updated from the testing segment but the training and testing segments are from three different subjects.

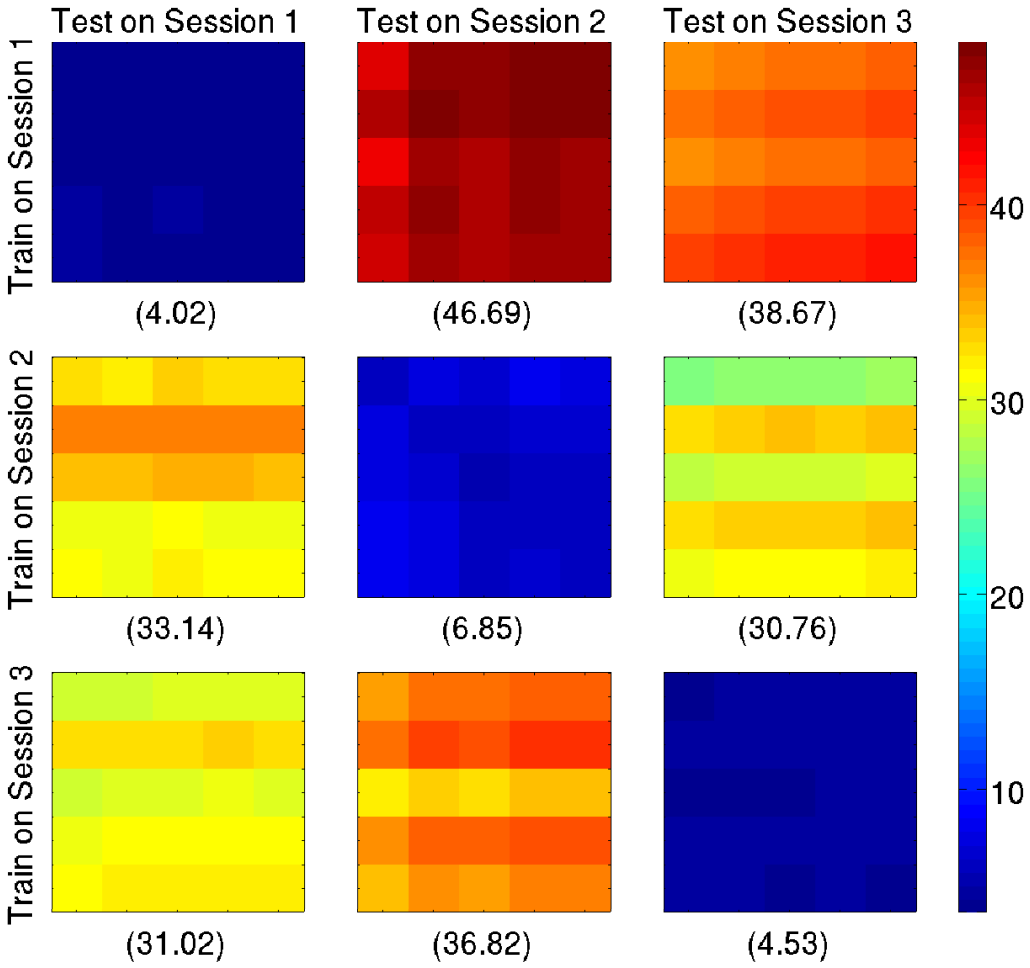

Figure 4.20: BCG estimation errors (*ave nRMSE*) in percentage (%) for models whose subset of channels were learned from one training segment and applied to another testing segment of the same subject when inference matrix was also from the training segment.

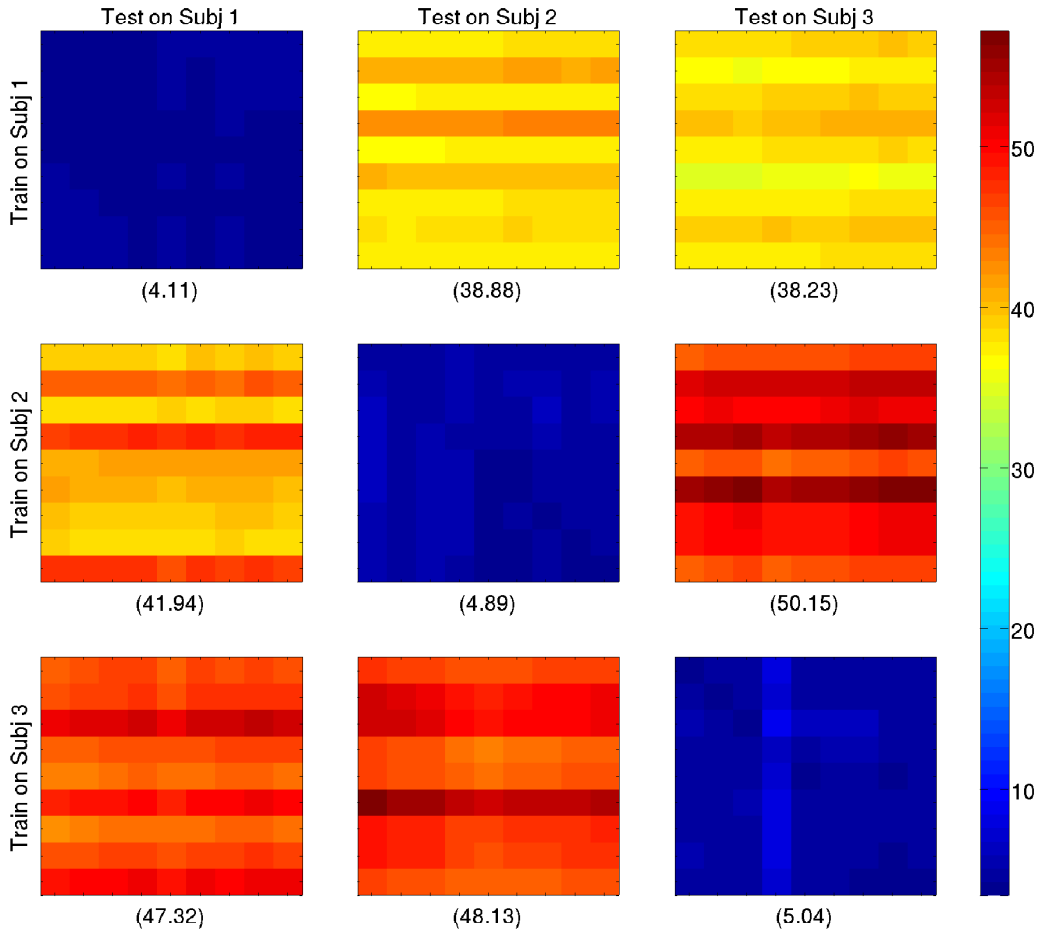

Figure 4.21: BCG estimation errors ($ave\ nRMSE$) in percentage (%) for models whose subset of channels were learned from one training segment and applied to another testing segment when inference matrix was also from the training segment but the training and testing segments are from four different subjects.

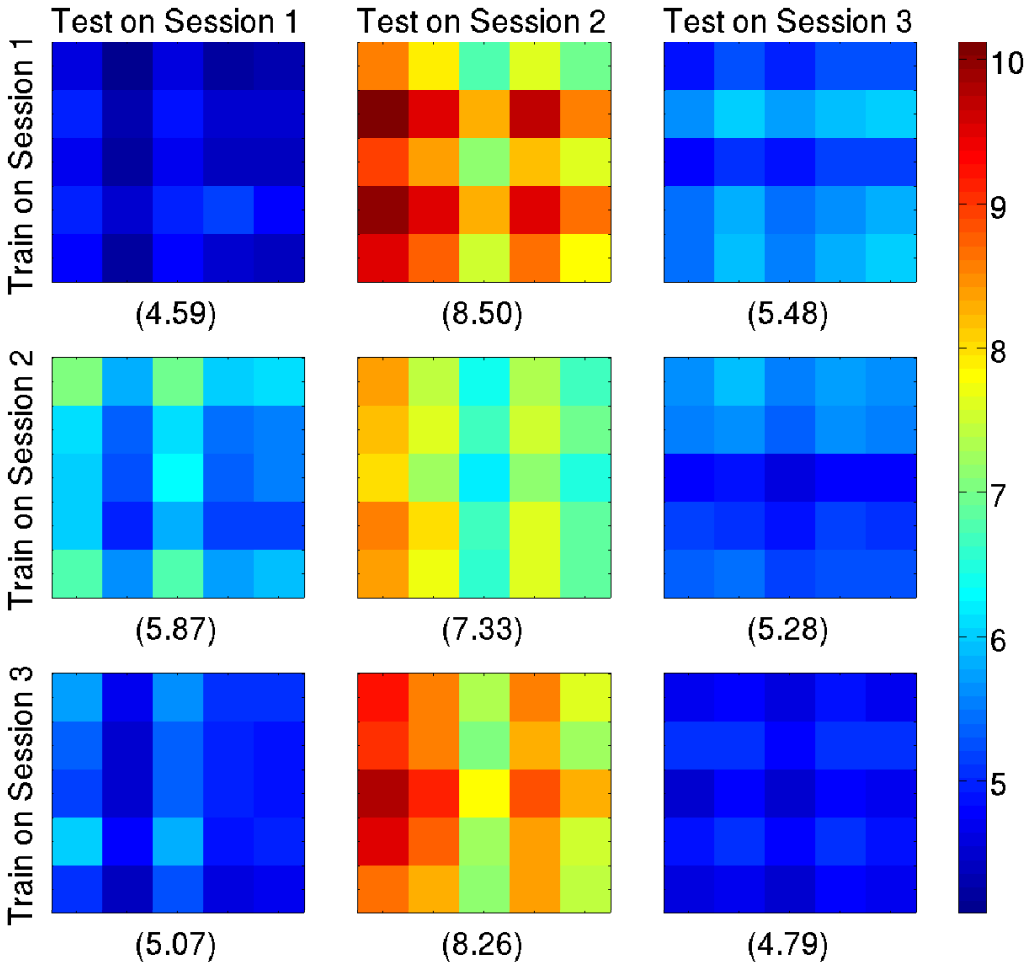

Figure 4.22: BCG estimation errors (*ave nRMSE*) in percentage (%) for models whose subset of channels were learned from one training segment and applied to another testing segment of the same subject when corresponding inference matrix was updated with our inference matrix recalculation method.

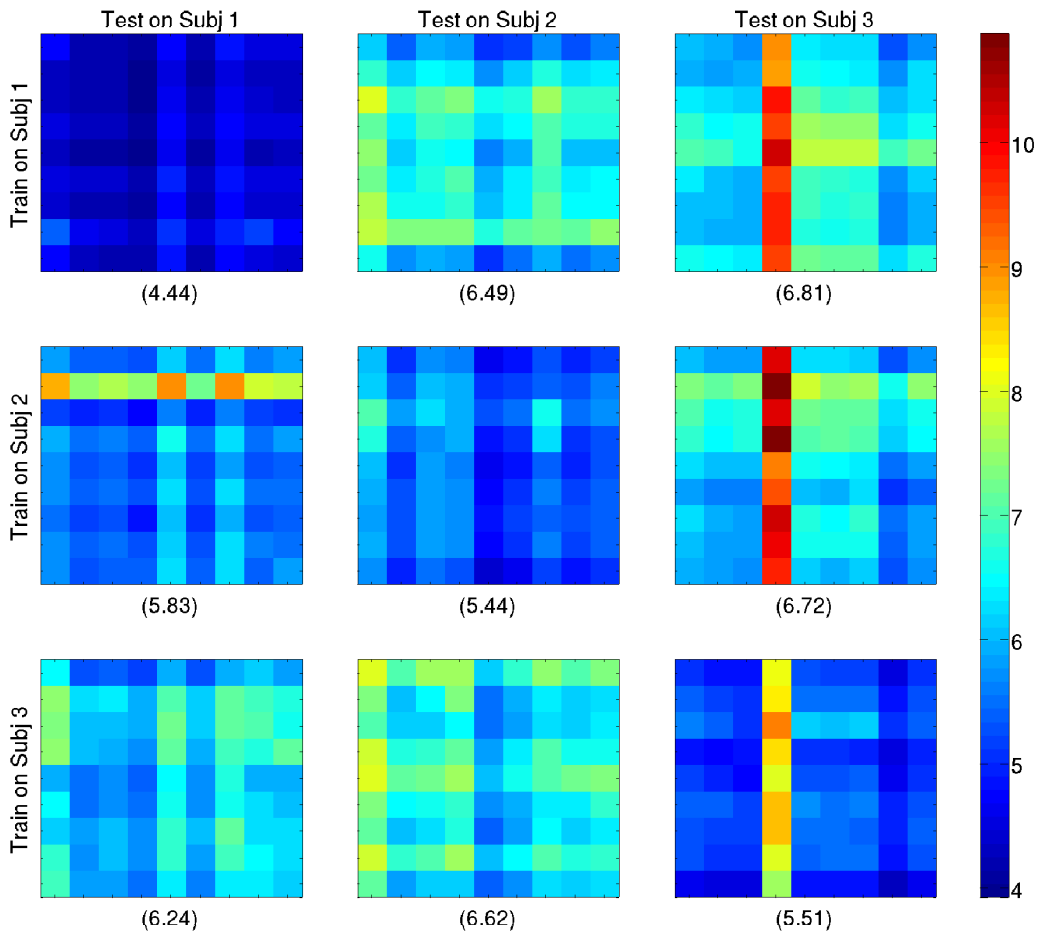

Figure 4.23: BCG estimation errors ($ave\ nRMSE$) in percentage (%) for models whose subset of channels were learned from one training segment and applied to another testing segment of the same subject when corresponding inference matrix was updated with our inference matrix recalculation method and the training and testing segments are from four different subjects.

CHAPTER 5

Conclusions and Future Work

5.1 Conclusions

We have invented three algorithms to improve the quality of reconstructed EEG acquired in simultaneous EEG-fMRI experiments. Firstly, We have developed a new Direct Recording Prior Encoding (DRPE) method [XRC14b] to extract and separate the BCG and EEG from contaminated signals, and have demonstrated its performance by comparing it quantitatively to the popular Optimal Basis Set (OBS) method. Our modified recording configuration allows us to obtain representative bases of the BCG- and EEG-only signals. We have developed an optimization-based reconstruction approach to maximally incorporate prior knowledge of the BCG/EEG subspaces, and of the signal characteristics within them. Both OBS and DRPE methods have been tested with experimental data, and compared quantitatively using cross-validation. In the challenging continuous EEG studies, DRPE outperforms the OBS method by nearly 7 fold in separating the continuous BCG and EEG signals. Secondly, without assuming orthogonality or independence of the BCG and EEG subspaces, as in conventional methods, we propose a Direct Recording Joint Incoherent Basis (DRJIB) [XRC13b] to learn the bases faithfully from BCG-only and EEG-only signals. Specifically, to promote subspace separability, a paired set of low-dimensional and semi-orthogonal (BCG, EEG) basis representations is obtained by minimizing a cost function consisting of group sparsity penalties for automatic dimension selection and an energy term for encouraging incoherence. Reconstruction is subsequently obtained by fitting the contaminated data to a generative model using the learned bases subject to regularization. In the non-event-related continuous EEG studies, our DRJIB method outperforms the OBS method by nearly 7.5

fold in separating and preserving the continuous BCG and EEG signals. Finally, we propose an integrated learning and inference approach, which takes advantage of currently available high-density EEG cap, to estimate the BCG contribution in noisy recordings from inside the MR scanner [XRC13a, XRC14a]. To reliably estimate the full-scalp BCG artifacts, a near-optimal small subset (20 out of 256) of channels is first identified and a corresponding weight is learned through our modified experimental setup. In subsequent recordings inside the MR scanner, BCG-only signal from this subset of channels and the previously learned weight are used to generate continuous estimate of the full-scalp BCG artifacts via inference, from which the intended EEG signal is recovered. The reconstruction of the EEG is performed with a direct subtraction and an optimization scheme. We evaluate the performance on both synthetic, and real contaminated recordings, and compare it to the benchmark Optimal Basis Set (OBS) method. In the non-event-related EEG studies, our reconstruction can yield more than fourteen-fold improvement in reducing the normalized RMS error of EEG signals, compared to OBS.

5.2 Future Work and Applications

5.2.1 Extending BCG removal methods

Although the results presented in this thesis have demonstrated the effectiveness of the BCG removal algorithms, there are a few practical issues to address for the clinical applications. The computational demand is high compared to the OBS method and the optimization procedure uses the alternating direction method of multipliers (ADMM) that usually takes 1-2 sec to evaluate each set of parameters. To be applicable to real-time EEG-fMRI studies, the proposed methods need to be modified to allow on-line artifact removal. For practical applications, we need to improve the workflow and reduce the complexity of the experimental setup to minimize the impact of additional time needed to acquire clean EEG and selecting subset of channels when high quality of reconstructed EEG is required and subject-specific channels are more desired. In addition, we can incorporate the proposed methods with other systems that provide BCG-reference signals, such as the KappaMetrics fEEG^{TM} system and

others [BPJ02, MAF07, CMG14], and providing guidance for placements of motion sensors, wire loops and fewer number of channels for the reference layer. Moreover, we can apply the proposed methods to different ERP studies and exploring the possibilities of different priors for each type of ERP studies. Because our method in principle extends to ERP studies, the artifact suppression effects may not significantly outperform the OBS method, due to the fact that averaging around known triggering events will reduce BCG residual signals when event timing is not correlated to the heartbeats.

5.2.2 Extending Simultaneous EEG-fMRI combining methods

Eventually, the artifact removal methods serve to better analyze the simultaneously acquired EEG and fMRI signals. [BPM11] has presented a comprehensive review about the directions and methods for combining EEG and fMRI. It is mentioned in [BPM11] that canonical correlation analysis (CCA) and its variants optimize the mutual information between two modalities with gaussian distribution and linearity assumptions. Although kernel tricks in CCA is helpful to explain certain non-linearity, it is more appropriate to directly apply manifold learning and nonlinear dimensionality reduction methods to explore the non-linear dependencies between two aligned datasets. To extend Maximum Covariance Unfolding (MCU) [MWP11] that computes a common low dimensional representations of two jointly acquired signals, we suggest replacing the distance measurements for the EEG datasets by a weighted temporal distance, adding a linear weighting function to incorporate temporal history information. This revision should take into account noninstantaneous couplings of two modalities, temporally compensating for modality specific differences and quantifying the contributions of single features to the coupling between two modalities.

References

[AJT00] P. J. Allen, O. Josephs, and R. Turner. "A method for removing imaging artifact from continuous EEG recorded during functional MRI." *NeuroImage*, **12**(2):230–9, 2000.

[APK98] Philip J. Allen, Giovanni Polizzi, Karsten Krakow, David R. Fish, and Louis Lemieux. "Identification of EEG Events in the MR Scanner: The Problem of Pulse Artifact and a Method for Its Subtraction." *NeuroImage*, **8**(3):229–239, 1998.

[ASY02] Kimitaka Anami, Osamu Saitoh, Masato Yumoto, Fumiko Tanaka, Yusuke Kawagoe, Takashi Ohnishi, and Hiroshi Matsuda. "Reduction of ballistocardiogram with a vacuum head-fixating system during simultaneous fMRI and multi-channel monopolar EEG recording." In *International Congress Series*, volume 1232, pp. 427–431. Elsevier, 2002.

[BAW03] Christian-G. Bénar, Yahya Aghakhani, Yunhua Wang, Aaron Izenberg, Abdullah Al-Asmi, François Dubeau, and Jean Gotman. "Quality of EEG in simultaneous EEG-fMRI for epilepsy." *Clinical Neurophysiology*, **114**(3):569–580, 2003.

[Ber29] Hans Berger. "Über das Elektrenkephalogramm des Menschen." *European Archives of Psychiatry and Clinical Neuroscience*, **87**(1):527–570, 1929.

[BGB06] E. Briselli, G. Garreffa, L. Bianchi, M. Bianciardi, E. Macaluso, M. Abbafati, M. Grazia Marciani, and B. Maraviglia. "An independent component analysis-based approach on ballistocardiogram artifact removing." *Magn Reson Imaging*, **24**(4):393–400, 2006.

[BMS08] Matthew J. Brookes, Karen J. Mullinger, Claire M. Stevenson, Peter G. Morris, and Richard Bowtell. "Simultaneous EEG source localisation and artifact rejection during concurrent fMRI by means of spatial filtering." *NeuroImage*, **40**(3):1090–1104, 2008.

[BPJ02] Giorgio Bonmassar, Patrick L. Purdon, Iiro P. Jaaskelainen, Keith Chiappa, Victor Solo, Emery N. Brown, and John W. Belliveau. "Motion and ballistocardiogram artifact removal for interleaved recording of EEG and EPs during MRI." *NeuroImage*, **16**(4):1127–1141, 2002.

[BPM11] F. Biessmann, S. Plis, F. C. Meinecke, T. Eichele, and K. R. Muller. "Analysis of Multimodal Neuroimaging Data." *Biomedical Engineering, IEEE Reviews in*, **4**:26–58, 2011.

[BSG07] C. G. Benar, D. Schon, S. Grimault, B. Nazarian, B. Burle, M. Roth, J. M. Badier, P. Marquis, C. Liegeois-Chauvel, and J. L. Anton. "Single-trial analysis of oddball event-related potentials in simultaneous EEG-fMRI." *Human Brain Mapping*, **28**(7):602–13, 2007.

[Cat75] Richard Caton. "Electrical currents of the brain." *The Journal of Nervous and Mental Disease*, **2**(4):610, 1875.

[CFZ08] A. C. Chen, W. Feng, H. Zhao, Y. Yin, and P. Wang. "EEG default mode network in the human brain: spectral regional field powers." *NeuroImage*, **41**(2):561–74, 2008.

[CGS01] M. S. Cohen, R. I. Goldman, J. Stern, and J. Engel. "Simultaneous EEG and fMRI made easy." *NeuroImage*, **13**(6):6, 2001.

[CMG14] Muhammad E.H. Chowdhury, Karen J. Mullinger, Paul Glover, and Richard Bowtell. "Reference layer artefact subtraction (RLAS): A novel method of minimizing {EEG} artefacts during simultaneous fMRI." *NeuroImage*, **84**(0):307 – 319, 2014.

[Coh02] M. S. Cohen. *Method and apparatus for reducing contamination of an electrical signal*. WO Patent 2,002,013,68902,013,689, 2002.

[COS09] J. F. Cai, S. Osher, and Z. Shen. "Split Bregman methods and frame based image restoration." *Multiscale modeling and simulation*, **8**(2):337–369, 2009.

[CT05] E. J. Candes and T. Tao. "Decoding by linear programming." *Information Theory, IEEE Transactions on*, **51**(12):4203–4215, 2005.

[DGS09] M. Dyrholm, R. Goldman, P. Sajda, and T. R. Brown. "Removal of BCG Artifacts Using a Non-Kirchhoffian Overcomplete Representation." *Ieee Transactions on Biomedical Engineering*, **56**(2):200–204, 2009.

[DMN08] Stefan Debener, Karen J. Mullinger, Rami K. Niazy, and Richard W. Bowtell. "Properties of the ballistocardiogram artefact as revealed by EEG recordings at 1.5, 3 and 7 T static magnetic field strength." *International Journal of Psychophysiology*, **67**(3):189–199, 2008.

[DSS07] Stefan Debener, Alexander Strobel, Bettina Sorger, Judith Peters, Cornelia Kranczioch, Andreas K Engel, and Rainer Goebel. "Improved quality of auditory event-related potentials recorded simultaneously with 3-T fMRI: removal of the ballistocardiogram artefact." *Neuroimage*, **34**(2):587–597, 2007.

[DUS05] S. Debener, M. Ullsperger, M. Siegel, K. Fiehler, D. Y. Von Cramon, and A. K. Engel. "Trial-by-trial coupling of concurrent electroencephalogram and functional magnetic resonance imaging identifies the dynamics of performance monitoring." *The Journal of Neuroscience*, **25**(50):11730–11737, 2005.

[DUS06] S. Debener, M. Ullsperger, M. Siegel, and A. K. Engel. "Single-trial EEG-fMRI reveals the dynamics of cognitive function." *Trends in Cognitive Sciences*, **10**(12):558–563, 2006.

[DWS12] Ana Diukova, Jennifer Ware, Jessica E Smith, C John Evans, Kevin Murphy, Peter J Rogers, and Richard G Wise. "Separating neural and vascular effects of caffeine using simultaneous EEG–FMRI: Differential effects of caffeine on cognitive and sensorimotor brain responses." *Neuroimage*, **62**(1):239–249, 2012.

[DYZ11] W. Deng, W. Yin, and Y. Zhang. "Group sparse optimization by alternating direction method." *TR11-06, Department of Computational and Applied Mathematics, Rice University*, 2011.

[ECM08] T. Eichele, V. D. Calhoun, M. Moosmann, K. Specht, M. L. A. Jongsma, R. Q. Quiroga, H. Nordby, and K. Hugdahl. "Unmixing concurrent EEG-fMRI with parallel independent component analysis." *International Journal of Psychophysiology*, **67**(3):222–34, 2008.

[ELS04] M. L. Ellingson, E. Liebenthal, M. V. Spanaki, T. E. Prieto, J. R. Binder, and K. M. Ropella. "Ballistocardiogram artifact reduction in the simultaneous acquisition of auditory ERPS and fMRI." *NeuroImage*, **22**(4):1534–1542, 2004.

[ESM05] T. Eichele, K. Specht, M. Moosmann, M. L. Jongsma, R. Q. Quiroga, H. Nordby, and K. Hugdahl. "Assessing the spatiotemporal evolution of neuronal activation with single-trial event-related potentials and functional MRI." *Proc Natl Acad Sci U S A*, **102**(49):17798–803, 2005.

[FF05] Kevin Forbes and Eugene Fiume. "An efficient search algorithm for motion data using weighted PCA." In *Proceedings of the 2005 ACM SIGGRAPH/Eurographics symposium on Computer animation*, pp. 67–76. ACM, 2005.

[FHT01] J. Friedman, T. Hastie, and R. Tibshirani. *The elements of statistical learning*, volume 1. Springer Series in Statistics, 2001.

[GLF86] Amiram Grinvald, Edmund Lieke, Ron D Frostig, Charles D Gilbert, and Torsten N Wiesel. "Functional architecture of cortex revealed by optical imaging of intrinsic signals." 1986.

[GNM10] F. Ghaderi, K. Nazarpour, J. G. McWhirter, and S. Sanei. "Removal of Ballistocardiogram Artifacts Using the Cyclostationary Source Extraction Method." *Biomedical Engineering, IEEE Transactions on*, **57**(11):2667–2676, 2010.

[GO09] T. Goldstein and S. Osher. "The Split Bregman Method for L1-Regularized Problems." *SIAM Journal on Imaging Sciences*, **2**(2):323–343, 2009.

[GSE00] Robin I. Goldman, John M. Stern, Jerome Engel Jr, and Mark S. Cohen. "Acquiring simultaneous EEG and functional MRI." *Clinical Neurophysiology*, **111**(11):1974–1980, 2000.

[GSE02] R. I. Goldman, J. M. Stern, Jr. Engel, J., and M. S. Cohen. "Simultaneous EEG and fMRI of the alpha rhythm." *Neuroreport*, **13**(18):2487–92, 2002.

[GVK07] Frédéric Grouiller, Laurent Vercueil, Alexandre Krainik, Christoph Segebarth, Philippe Kahane, and Olivier David. "A comparative study of different artefact removal algorithms for EEG signals acquired during functional MRI." *NeuroImage*, **38**(1):124–137, 2007.

[HBM95] Frank R. Huang-Hellinger, Hans C. Breiter, Glen McCormack, Mark S. Cohen, Ken K. Kwong, Jeffrey P. Sutton, Robert L. Savoy, Robert M. Weisskoff, Timothly L. Davis, John R. Baker, John W. Belliveau, and Bruce R. Rosen. "Simultaneous functional magnetic resonance imaging and electrophysiological recording." *Human Brain Mapping*, **3**(1):13–23, 1995.

[HSM04] Scott A Huettel, Allen W Song, and Gregory McCarthy. *Functional magnetic resonance imaging*, volume 1. Sinauer Associates Sunderland, MA, 2004.

[ILP06] Myung H In, Soo Y Lee, Tae S Park, Tae-S Kim, Min H Cho, and Young B Ahn. "Ballistocardiogram artifact removal from EEG signals using adaptive filtering of EOG signals." *Physiological measurement*, **27**(11):1227, 2006.

[Job77] Frans F Jobsis. "Noninvasive, infrared monitoring of cerebral and myocardial oxygen sufficiency and circulatory parameters." *Science*, **198**(4323):1264–1267, 1977.

[KML01] K. Krakow, D. Messina, L. Lemieux, J. S. Duncan, and D. R. Fish. "Functional MRI Activation of Individual Interictal Epileptiform Spikes." *NeuroImage*, **13**(3):502–505, 2001.

[KRU97] Seong-Gi Kim, Wolfgang Richter, and Kmil Uurbil. "Limitations of temporal resolution in functional MRI." *Magnetic Resonance in Medicine*, **37**(4):631–636, 1997.

[LKS03] H. Laufs, K. Krakow, P. Sterzer, E. Eger, A. Beyerle, A. Salek-Haddadi, and A. Kleinschmidt. "Electroencephalographic signatures of attentional and cognitive default modes in spontaneous brain activity fluctuations at rest." *Proceedings of the National Academy of Sciences*, **100**(19):11053–11058, 2003.

[LSJ01] Louis Lemieux, Afraim Salek-Haddadi, Oliver Josephs, Philip Allen, Nathan Toms, Catherine Scott, Karsten Krakow, Robert Turner, and David R. Fish. "Event-Related fMRI with Simultaneous and Continuous EEG: Description of the Method and Initial Case Report." *NeuroImage*, **14**(3):780–787, 2001.

[LZG12] Z. Liu, J. A. de Zwart, P. van Gelderen, L. W. Kuo, and J. H. Duyn. "Statistical feature extraction for artifact removal from concurrent fMRI-EEG recordings." *NeuroImage*, **59**(3):2073–87, 2012.

[MAF07] Richard A. J. Masterton, David F. Abbott, Steven W. Fleming, and Graeme D. Jackson. "Measurement and reduction of motion and ballistocardiogram artefacts from simultaneous EEG and fMRI recordings." *NeuroImage*, **37**(1):202–211, 2007.

[MEN08] M. Moosmann, T. Eichele, H. Nordby, K. Hugdahl, and V. D. Calhoun. "Joint independent component analysis for simultaneous EEG–fMRI: principle and simulation." *International Journal of Psychophysiology*, **67**(3):212–221, 2008.

[MHB13] K. J. Mullinger, J. Havenhand, and R. Bowtell. "Identifying the sources of the pulse artefact in EEG recordings made inside an MR scanner." *NeuroImage*, **71C**:75–83, 2013.

[MJS04] C. Mulert, L. Jager, R. Schmitt, P. Bussfeld, O. Pogarell, H. J. Moller, G. Juckel, and U. Hegerl. "Integration of fMRI and simultaneous EEG: towards a comprehensive understanding of localization and time-course of brain activity in target detection." *NeuroImage*, **22**(1):83–94, 2004.

[ML09] Christoph Mulert and Louis Lemieux. *EEG-fMRI: physiological basis, technique, and applications*. Springer, 2009.

[Mou57] Vernon B Mountcastle. "Modality and topographic properties of single neurons of cats somatic sensory cortex." *J. neurophysiol*, **20**(4):408–434, 1957.

[MPC07] D. Mantini, M. G. Perrucci, S. Cugini, A. Ferretti, G. L. Romani, and C. Del Gratta. "Complete artifact removal for EEG recorded during continuous fMRI using independent component analysis." *NeuroImage*, **34**(2):598–607, 2007.

[MWP11] Vijay Mahadevan, Chi W Wong, Jose C Pereira, Tom Liu, Nuno Vasconcelos, and Lawrence K Saul. "Maximum covariance unfolding: Manifold learning for bimodal data." In *Advances in Neural Information Processing Systems*, pp. 918–926, 2011.

[NAM06] Wakako Nakamura, Kimitaka Anami, Takeyuki Mori, Osamu Saitoh, Andrzej Cichocki, and S-I Amari. "Removal of ballistocardiogram artifacts from simultaneously recorded EEG and fMRI data using independent component analysis." *Biomedical Engineering, IEEE Transactions on*, **53**(7):1294–1308, 2006.

[NBI05] R. K. Niazy, C. F. Beckmann, G. D. Iannetti, J. M. Brady, and S. M. Smith. "Removal of FMRI environment artifacts from EEG data using optimal basis sets." *NeuroImage*, **28**(3):720–737, 2005.

[NS05] Ernst Niedermeyer and FH Lopes da Silva. *Electroencephalography: basic principles, clinical applications, and related fields*. Lippincott Williams & Wilkins, 2005.

[Nun81] PL Nunez. "Electric fields of the brain, 1981.", 1981.

[RS10] Jorge Riera and Pedro Valdes Sosa. "Mesoscale in neuroimaging: creating bridges between the microscopic and system levels." *Journal of integrative neuroscience*, **9**(4):v–vii, 2010.

[RSS10] I. Ramirez, P. Sprechmann, and G. Sapiro. "Classification and clustering via dictionary learning with structured incoherence and shared features.", 13-18 June 2010 2010.

[SBG05] G. Sammer, C. Blecker, H. Gebhardt, P. Kirsch, R. Stark, and D. Vaitl. "Acquisition of typical EEG waveforms during fMRI: SSVEP, LRP, and frontal theta." *NeuroImage*, **24**(4):1012–1024, 2005.

[SCL05] G. Srivastava, S. Crottaz-Herbette, K. M. Lau, G. H. Glover, and V. Menon. "ICA-based procedures for removing ballistocardiogram artifacts from EEG data acquired in the MRI scanner." *NeuroImage*, **24**(1):50–60, 2005.

[SGA11] Boaz Sadeh, Tamar Goldberg, Chen Avni, Michel Pelleg, and Galit Yovel. "The role of face-selective and object-general mechanisms in the face inversion effect: A simultaneous EEG-fMRI study." *Journal of Vision*, **11**(11):638–638, 2011.

[TG07] J. A. Tropp and A. C. Gilbert. "Signal Recovery From Random Measurements Via Orthogonal Matching Pursuit." *Information Theory, IEEE Transactions on*, **53**(12):4655–4666, 2007.

[TGM83] TS Tenforde, CT Gaffey, BR Moyer, and TF Budlnger. "Cardiovascular alterations in Macaca monkeys exposed to stationary magnetic fields: experimental observations and theoretical analysis." *Bioelectromagnetics*, **4**(1):1–9, 1983.

[UD10] M. Ullsperger and S. Debener. *Simultaneous EEG and fMRI: recording, analysis, and application*. Oxford Univ Pr, 2010.

[VDR10] Katrien Vanderperren, Maarten De Vos, Jennifer R. Ramautar, Nikolay Novitskiy, Maarten Mennes, Sara Assecondi, Bart Vanrumste, Peter Stiers, Bea R. H. Van den Bergh, Johan Wagemans, Lieven Lagae, Stefan Sunaert, and Sabine Van Huffel. "Removal of BCG artifacts from EEG recordings inside the MR scanner: A comparison of methodological and validation-related aspects." *NeuroImage*, **50**(3):920–934, 2010.

[XRC13a] Hongjing Xia, Dan Ruan, and Mark S Cohen. "BCG Artifact Removal for Reconstructing Full-scalp EEG inside the MR Scanner." In *Pattern Recognition in Neuroimaging (PRNI), 2013 International Workshop on*, pp. 178–181. IEEE, 2013.

[XRC13b] Hongjing Xia, Dan Ruan, and M.S. Cohen. "Coupled basis learning and regularized reconstruction for BCG artifact removal in simultaneous EEG-FMRI studies." In *Biomedical Imaging (ISBI), 2013 IEEE 10th International Symposium on*, pp. 986–989, 2013.

[XRC14a] Hongjing Xia, Dan Ruan, and Mark S Cohen. "Removing ballistocardiogram (BCG) artifact from full-scalp EEG acquired inside the MR scanner with Orthogonal Matching Pursuit (OMP)." *Frontiers in neuroscience*, **8**, 2014.

[XRC14b] Hongjing Xia, Dan Ruan, and Mark Steven Cohen. "Separation and Reconstruction of BCG and EEG Signals during Continuous EEG and fMRI Recordings." *Brain Imaging Methods*, **8**:163, 2014.

[YMG10] Winston X. Yan, Karen J. Mullinger, Gerda B. Geirsdottir, and Richard Bowtell. "Physical modeling of pulse artefact sources in simultaneous EEG/fMRI." *Human Brain Mapping*, **31**(4):604–620, 2010.

[ZHT06] Hui Zou, Trevor Hastie, and Robert Tibshirani. "Sparse principal component analysis." *Journal of computational and graphical statistics*, **15**(2):265–286, 2006.